# Interface Engineering for Highly Efficient Perovskite Solar Cells

Saeid Rafizadeh

Tesi per il conseguimento del titolo

Università degli Studi di Pavia
Dipartimento di Fisica

DOTTORATO DI RICERCA IN FISICA – XXX CICLO

Interface Engineering for Highly Efficient Perovskite Solar Cells

Saeid Rafizadeh

Submitted to the Graduate School of Physics in partial

fulfillment of the requirements for the degree of

DOTTORE DI RICERCA IN FISICA

DOCTOR OF PHILOSOPHY IN PHYSICS

at the

University of Pavia

Supervisor: Prof. Lucio Claudio Andreani

Abstract

After decades of research, crystalline silicon technology dominates the global photovoltaic market by 92%.[1] To gain market share from crystal silicon solar cells, emerging photovoltaic technologies have to demonstrate a combination of high power conversion efficiency (PCE), easy and cost-effective manufacturing processes and long-term stability. Recent researches suggest that organic-inorganic halide perovskites have the potential to meet these conditions and become competitive in the marketplace.[2-7]

The work presented here is comprised of an experimental study on the fabrication of perovskite solar cells using a two-step hybrid evaporation-spincoating method. Solution processing enables easy fabrication processes[2-8] with possibility of band-gap tuning[9] for tandem application[9-14] while vacuum basted methods[15-20] offer the advantages of deposition on non-planar surfaces like light trapping pyramidal textured structures, interesting for tandem configuration on high efficiency silicon solar cells.[21-22] The hybrid two-step evaporation-spincoating deposition method, gains benefit from both solution processing and vacuum based deposition advantages while not suffering from the drawback of hazardous solvents consumption in solution processing.[18-20]

With maturing of the fabrication methods, a deepened understanding of which factors determine PCE, becomes more and more important for further improvements. Especially understanding of the crystallization and the layer

ripening is crucial as those determine the occurring of defect centers that could limit performance. Accordingly, the role of excess PbI_2 in perovskite structures and its impact on crystallization quality, optoelectronic properties and photovoltaic performance of different perovskite solar cells is studied in this thesis. It is found that a higher concentration of remnant and unconverted PbI_2 correlates with smaller and stronger interconnected grains, as well as with an improved optoelectronic performance of the solar cells with higher efficiencies and the mitigation of hysteresis.

Moreover, the issue of "Interface Engineering" at the perovskite top and bottom interfaces is addressed. Optimization of the charge carrier transport layers improved the optoelectronic and photovoltaic parameters. The impact of different transparent conductive oxides is also investigated in this thesis. The optical and electrical parameters of the perovskite absorber deposited on FTO and ITO transparent conductive oxides are compared. This is interesting especially for the tandem applications where the interface engineering is crucial for decreasing the parasitic losses.

Tandem perovskite on silicon architecture is presented as an outlook for this thesis. Implementation of perovskite absorber fabricated by hybrid method atop highly efficient silicon bottom cell would lead to the efficiencies beyond theoretical efficiency limit of single junction solar cells.

Preface

This thesis work has been initiated at the Department of Physics, University of Pavia where I have started my PhD in 2015 under supervision of Prof. Lucio Claudio Andreani.

The initial investigation on the perovskite solar cells fabrication and characterization was done under supervision of Dr. Annamaria Petrozza at the Center for Nano Science and Technology (CNST) in Milan/Italy, which is a research center within the Italian Institute of Technology (IIT). I spent the second year of my PhD in this prestigious center and got familiar with the basics of perovskite materials and realization of perovskite solar cells.

The main experimental goals of this thesis has been followed in the Fraunhofer Institute for Solar Energy Systems ISE in Freiburg/Germany, where I joined as a visiting PhD student and could use the opportunity of working in high-tech labs with advanced facilities for fabrication and characterization of high efficiency perovskite solar cells utilizing the novel two-step hybrid evaporation-spincoating method.

Working in the field of perovskite solar cells was extremely challenging for me because I had to gain a lot of knowledge from the Material and Chemistry sciences and combine them with my Physics and thin film technology background within a short time period to fulfill an innovative and productive research work.

The necessity to gain these knowledges made me get to know many talented and interesting people from whom I learned a lot during my PhD. I hope the results achieved in this study would be useful for the researchers of photovoltaics, especially those who have been focused on perovskite solar cells fabrication and characterization.

Acknowledgements

My 3 years PhD journey has passed but left me a lot of memorable moments. I would like to use this opportunity and express my sincere gratefulness to the marvelous people who helped me to successfully reach the final destination of this journey. I wish to express my warmest regards to my supervisor Prof. Andreani whose unlimited support from beginning to end was the major reason for this accomplishment. I would also thank Prof. Guglielmo Lanzani and Dr. Annamaria Petrozza for hosting me in the Center for Nanoscience and Technology (CNST) where I learned the basics of perovskite solar cells. My very special thanks to Prof. Stefan Glunz and Dr. Jan Christoph Goldschmidt to host me in prestigious Fraunhofer Institute for Solar Energy Research ISE and University of Freiburg where I fulfilled the major part of my research work to finalize this thesis work. I should also thank all my colleagues in the department of physics at University of Pavia, CNST IIT, Fraunhofer ISE and University of Freiburg with whom I had productive long hours of scientific discussions which enabled me to improve day to day.

Finally I wish to express my endless love to the most important people of my life, my mother Soheila, father Aliakbar, brother Sahand and wife Maral. I believe without their outstanding support I wouldn't be able to move in this challenging path and successfully reach to the final point.

Contents

List of abbreviations

XRD   **X**-**R**ay **D**iffraction

SEM   **S**canning **E**lectron **M**icroscopy

AFM   **A**tomic **F**orce **M**icroscopy

KPFM   **K**elvin **P**robe **F**orce **M**icroscopy

TRPL   **Tr**ansient **Ph**otoluminescence

Jsc   **S**hort **C**ircuit **C**urrent

Voc   **O**pen **C**ircuit **V**oltage

FF   **F**ill **F**actor

PCE   **P**ower **C**onversion **E**fficiency

EQE   **E**xternal **Q**uantum **E**fficiency

PSCs   **P**erovskite **S**olar **C**ell**s**

MA   **M**ethylammonium

FA   **F**ormamidinium

Cs   **C**esium

Rb   **R**ubidium

Pb   **L**ead

Sn   **T**in

I   **I**odine

Cl   **C**hlorine

Br   **B**romine

DMF   **Dim**ethyl**f**ormamide

DMSO   **Dim**ethyl**s**ulfoxide

Spiro-MeOTAD   N2,N2,N2',N2',N7,N7,N7',N7'-octakis(4-methoxyphenyl)-

9,9'-spirobi[9H-fluorene]-2,2',7,7'-tetramine

PCBM   [6,6]-**P**henyl **C**61 **b**utyric acid **m**ethyl ester

PEDOT-PSS   **P**oly(3,4-**e**thylene**d**ioxy**t**hiophene)-**p**oly(**s**tyrene**s**ulfonate)

PTAA   **P**oly[bis(4-phenyl)(2,4,6-**t**rimethylphenyl)**a**mine]

BCP   **B**atho**cup**roine

Jsc   **S**hort **C**ircuit **C**urrent

Voc   **O**pen **C**ircuit **V**oltage

FF   **F**ill **F**actor

PCE   **P**ower **C**onversion **E**fficiency

TCSPC   **T**ime-**C**orrelated **S**ingle **P**hoton **C**ounting

List of publications

Conference Presentations:

1- **Saeid Rafizadeh**, et al. Perovskite Solar Cells, International Summer School and Workshop on Photovoltaic Science and Technology, June 2016, Ankara, Turkey.

2- **Saeid Rafizadeh**, et al. 18.3% Stabilized Efficiency in Hybrid Evaporation-Spincoating Low-Temperature Processed Planar Perovskite Solar Cell, PSCO 2017, 18-20 September 2017, Oxford, U.K.

3- **Saeid Rafizadeh**, et al. Record Stabilized Efficiencies Exceeding 18% for Hybrid Evaporation-Spincoating Planar Perovskite Solar Cells, HOPV 2018, 28-31 May 2018 Benidorm, Spain. (Best Poster Award)

4- **Saeid Rafizadeh**, et al. Evaporation-Based Perovskite Solar Cells: Promising Methods with Reproducible High Efficiencies for Tandem Applications, PVCON2018, 4-6 July 2018, Ankara, Turkey.

5- **Saeid Rafizadeh**, et al. Stoichiometry Engineering for Efficiency Enhancement and Hysteresis Mitigation in Hybrid Evaporation-Spincoated Perovskite Solar Cells, PSCO 2018, 30-2 October 2018, Lausanne, Switzerland.

Journal Publications:

1- **Rafizadeh, S.**; Wienands, K.; Schulze, P. S. C.; Bett, A. J.; Andreani, L. C.; Hermle, M.; Glunz, S. W.; Goldschmidt, J. C., Efficiency Enhancement and Hysteresis Mitigation by Manipulation of Grain Growth Conditions in Hybrid Evaporated−Spin-coated Perovskite Solar Cells. *ACS Appl. Mater. Interfaces* **2019**, *11*, 722-729.

2- **Rafizadeh, S.**; Wienands, K.; Mundt, L. E.; Bett, A. J.; Schulze, P. S. C.; Andreani, L. C.; Hermle, M.; Glunz, S. W.; Goldschmidt, J. C. The Role of Surface Passivation Layer Prepration in Crystallization and Optoelectronic Performance of Hybrid Evaporated-Spincoated Perovskite Solar Cells. *IEEE JOURNAL OF PHOTOVOLTAICS* **2019**, *9*, 1428-1435.

3- Cojocaru, L.; Wienands, K.; Kim, T. W.; Uchida, S.; Bett, A. J.; **Rafizadeh, S.**; Goldschmidt, J. C.; Glunz, S. W. Detailed Investigation of Evaporated Perovskite Absorbers with High Crystal Quality on Different Substrates. *ACS Appl. Mater. Interfaces* **2018**, *10*, 26293-26302.

4- Patricia S.C. Schulze, Karl Wienands, Alexander J. Bett, **Saeid Rafizadeh**, Laura E. Mundt, Ludmila Cojocaru, Martin Hermle, Stefan Glunz and Jan Christoph Goldschmidt, *High band gap perovskite deposition via a hybrid evaporation/ spin coating method for application in fully textured monolithic silicon-based tandem stacks*, Manuscript Submitted.

Chapter 1: Introduction

1.1 Perovskite solar cell materials and interfaces

Perovskite is calcium titanium oxide with the chemical formula $CaTiO_3$. The mineral was found in the Ural Mountains by Gustav Rose in 1839 and was named after Russian mineralogist Count Lev Perovski (1792-1856). All materials with the same crystal structure as $CaTiO_3$, namely ABX_3 are termed perovskites. However, $CaTiO_3$ is an insulator and not suitable for photovoltaic applications.

The useful materials from perovskite family for solar cells fabrication are lead halide perovskites with an ABX_3 structure where A is an organic cation like methylammonium (MA) or formamidinium (FA) or inorganic cation like cesium (Cs) or rubidium (Rb), B is a metal like lead (Pb) or tin (Sn) and X is a halide like iodine (I), chlorine (Cl) or bromine (Br).

(a) CaTiO$_3$ **(b) ABX$_3$ Perovskite Crystal Structure**
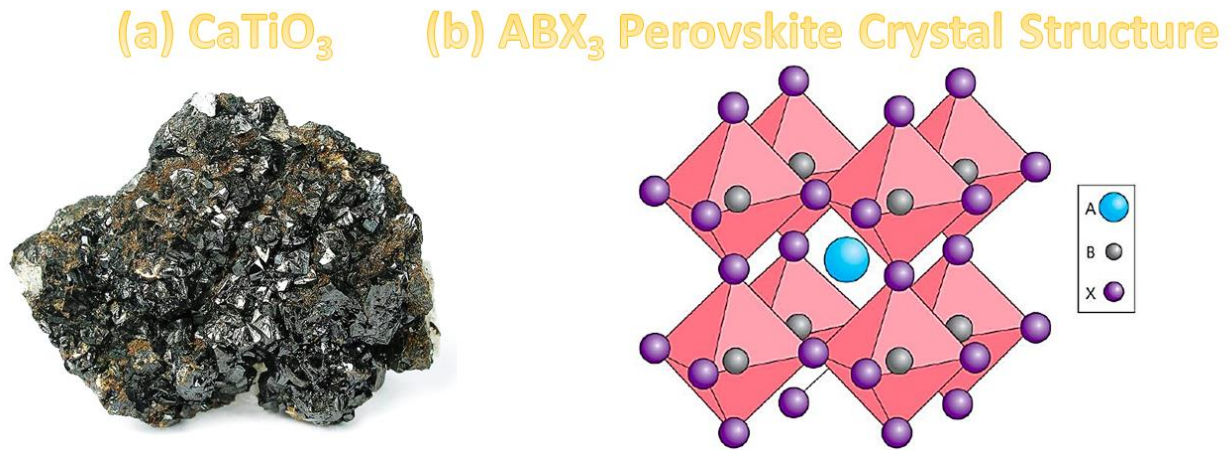
Figure 1. The CaTiO$_3$ mineral (a) and the ABX$_3$ perovskite crystal structure (b).[25]

The first successful implementation of perovskite materials in solar cells was realized in 2009 by using the MAPbI$_3$ and MAPbBr$_3$ as the semiconductor sensitizer in liquid electrolyte dye-sensitized solar cells.[23-25] In recent years the perovskite solar cells (PSCs) have soared by power conversion efficiencies (PCEs) reaching more than 25 % in 2019.[26] This class of perovskite materials have a tunable band gap from 1.15 eV (MASn$_{0.8}$Pb$_{0.2}$I$_3$) to 3.06 eV (CsPbCl$_3$) by interchanging the cations, metals and/or halides.[27]
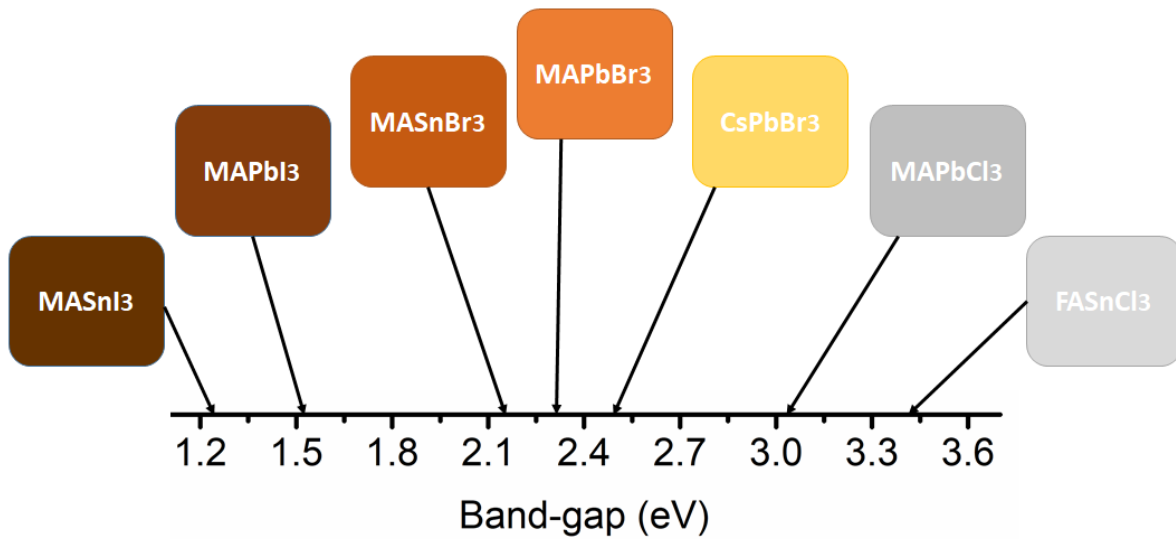
Figure 2. Band-gap tuning in perovskite solar cells.

The variety of ions that can occupy the A, B and X-sites enables variation of optoelectronic properties in perovskite solar cells. The possible combinations of A and B sites are determined by Goldschmidt tolerance factor, which is derived from a close-packing of spherical hard ions. The best performing recently reported perovskite solar cells are employed complex stoichiometry based on cesium (Cs), formamidinium (FA) and methylammonium (MA) cations on A-site and iodine and bromine on the X-site. This complexity affects performance and stability of the solar cells due to variation of trap states in the material bulk and interfaces as well as energy alignment and chemical reactions.

A combination of unique characteristics of hybrid perovskites such as high absorption coefficient, long carrier diffusion length and shallow trap energy

levels puts them within a potential application space beyond photovoltaic application.

1.2 Perovskite deposition methods

The unprecedented progress in perovskite solar cells performance is strongly correlated to the improvements in deposition methods. The formation of a pin hole-free, compact and uniform layer is a prerequisite for high efficiency. This is especially more pronounced in planar structure where the pin holes may become shunt paths.

Different fabrication methods have been employed so far.[27-30] Spin-coating,[2-8] either one-step or two-step, has been the most common perovskite deposition method. In one-step method, a precursor from a solution containing a metal-halide like PbI_2 and organo-halide like MAI in a solvent such as dimethylformamide (DMF) and/or dimethylsulfoxide (DMSO) was prepared and spin-coated. While spin-coating, an anti-solvent like toluene was dropped on top, this induces rapid dissolution of perovskite salt within the solution and causes a good quality film formation after annealing at 120 °C for 30 min under nitrogen atmosphere. In two-step solution processing method, two separate solutions of metal-halides and organo-halides in DMF and IPA were prepared, respectively. In first step, PbI_2 in DMF was spin-coated followed by annealing at 100 °C for 10 min. To convert the PbI_2 into perovskite, deposited layer was immersed in MAI solution in the second step. The MAI solution could also be spin-coated for

perovskite layer formation. Both methods were followed by annealing at 120 °C for 30 min in nitrogen atmosphere. In general, spin-coating enables easy fabrication processes with control over crystallization by solution modification using additives,[7-8] or band-gap tuning,[27] for tandem applications[9].

Vacuum-based deposition methods,[15-20] demonstrated high throughput and reliability due to well stablished fabrication methods in electronic industry. In this case both metal-halide and organo-halide components could be co-evaporated resulting in a fully evaporated perovskite layer formation or evaporation of metallic part and spin-coating of organic part to form a perovskite layer with a hybrid deposition route. Additionally, vacuum basted methods would offer the advantages of deposition on non-planar surfaces like light trapping pyramidal textured structures, interesting for tandem configurations on high efficiency silicon solar cells with light trapping structures. It also worth to mention that in vacuum deposition methods, there is no need to use toxic and flammable solvents such as DMF and DMSO, which is indeed a drawback for solution processing method. The hybrid two-step evaporation-spincoating deposition method,[17-20] gains benefit from both spin-coating and vacuum based deposition advantages while not suffering from the drawback of aggressive solvents consumption in solution processing. Non-hazardous solvents consumption offers the possibility of deposition on variety of substrates which are sensitive to aggressive solvents.

Blade coating[28], Slot die coating[29] and inkjet printing[30] are other deposition methods especially important for large area deposition. In blade coating a sharp blade moves over a solution droplet perpendicular to the substrate. In slot die coating precursor solution pumps over a moving substrate at a fixed substrate-to-nozzle height. Variation of substrate moving speed and ink flow rate enable the layer thickness control. Inkjet printing provides a controlled layer formation through rapid and digital deposition.

All the above mentioned processing methods are potentially scalable for large production lines.[27-30] In the end, this is the target application, which determines the best deposition method. For instance, realization of tandem configuration requires a precise and more controlled deposition method like full evaporation or hybrid method while for the consumable electronics solution-based techniques are cost-effective.
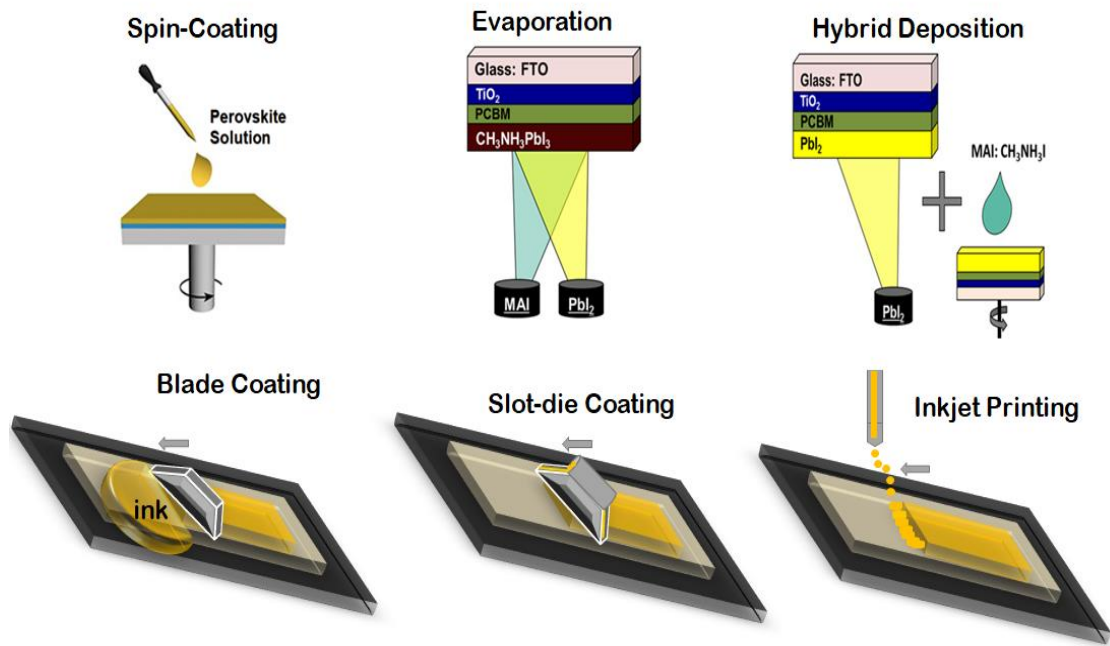
Figure 3. Different deposition methods of perovskite solar cells.

1.3 Perovskite solar cell architectures

At first halide perovskite was used as a dye in dye-sensitized solar cells (DSSC) and then in more stable solid-state DSSC.[24] In both cases the TCO coated glass substrates were covered with a mesoporous titanium oxide as an electron transport layer. The perovskite was then deposited on mesoporous electron transport layer. Later the mesoporous was substituted by insulating Al_2O_3 or removed to form a planar heterojunction. Finally the device was completed by deposition of a p-type hole transport layer and subsequent metal contact. Later other oxides such as SnO_2[45]and ZnO[34] were tested as electron transport layers.

This architecture of perovskite solar cells is called standard or n-i-p. Over time different perovskite solar cell architectures have been developed. In general, perovskite solar cells have been realized in two architectures, standard n-i-p and inverted p-i-n.[32-33] In p-i-n, the perovskite layer was deposited on a p-type hole transport layer such as inorganic NiOx[35] or polymers like PEDOT:PSS[33] and PTTA[33]. Then the device would be completed by deposition of an organic electron transport layer such as fullerene derivatives (C_{60}, PCBM) or bathocuproine (BCP) followed by a metal contact.

To realize highly efficient working devices utilizing the unique optoelectronic properties of perovskite bulk materials, the interfaces between perovskite and adjacent materials plays a crucial role. This bolds the importance of choosing the proper ELT and HTL layers. Compact or pinhole-free layers prevent shunt paths between top and bottom electrodes while transparent layers avoid parasitic absorption. Electrically conductive with aligned energy levels facilitates charge carrier transport with minimum energy losses.
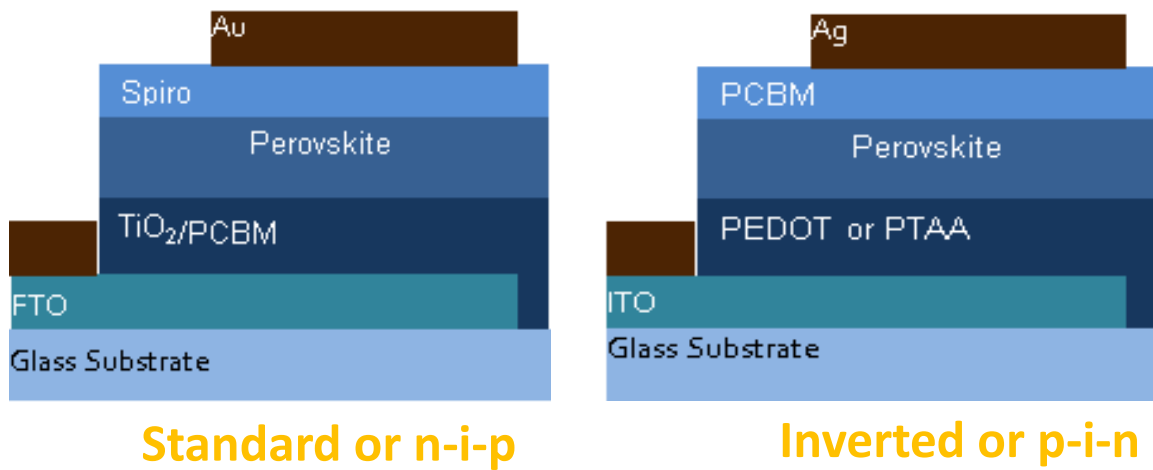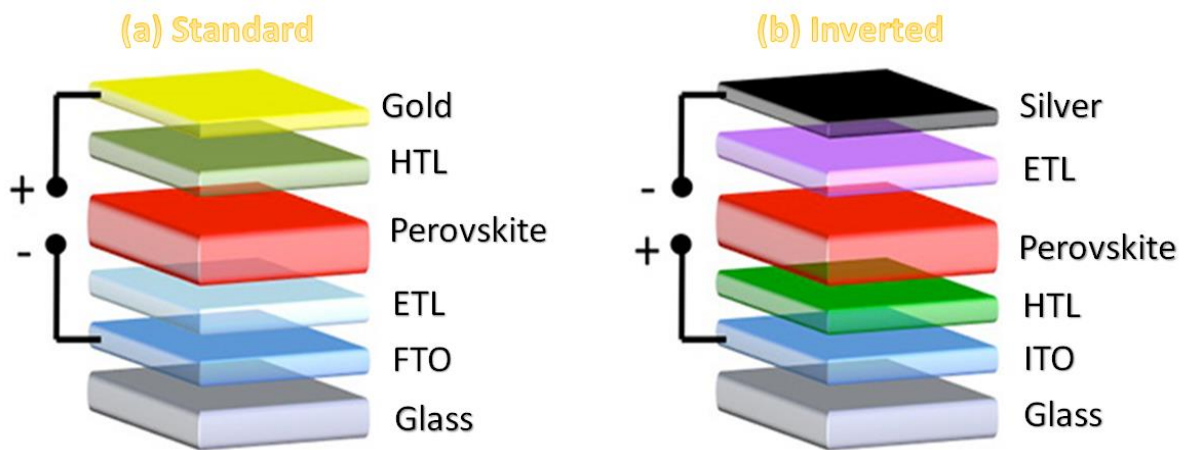
Figure 4. Different perovskite solar cells architectures.

1.4 Challenges for high efficiencies

The challenges for high efficiencies in perovskite solar cells can be categorized in four levels, perovskite atoms, grains, layers and charge carrier extraction interfaces.

In atomic level, perovskite crystals are made of ions which can move within the perovskite lattice.[36] These ionic motions play an important role in outstanding photovoltaic behavior of perovskite solar cells.[37-40] However under cell working conditions (voltage and light bias) these ions accumulate at the interfaces and turn to the trap states and limit the charge carrier extractions and thereupon decrease the cell performance.[41] The hysteresis which is known as an intrinsic drawback in perovskite solar cells, where the forward and backward current-voltage curves differ, is correlated to halide migration in perovskite lattice.[34-41] To deal with the drawback of ions migration, the passivation of defect traps at the perovskite/charge carrier interfaces and also within the perovskite bulk is extremely crucial.[42-47] The perovskite grains are formed by interconnection of perovskite crystal atoms. The role of grain boundaries on the device performance is widely investigated, although there is no definite answer to the question of whether the grain boundaries are detrimental or beneficial for the solar cell performance.[48-54] Further investigations addressing this challenge should be done to clarify the optimum grains formation and interconnection situation. Indeed the well-impinged grains form a uniform and compact (pinhole-free) bulk layer, exactly where the charge carrier generation takes place. Furthermore, a good passivation of bulk and interface trap states, enhances the photo carrier generation and paves the charge injection ways into the charge transport layers.

The fourth challenge on the way of a high efficiency perovskite solar cell fabrication is the selection of proper charge carrier transport layers with aligned energy bands to collect the carriers before being recombined.[55-67]

1.5 Perovskite solar cells record efficiencies

The perovskite solar cells efficiencies have increased with an unprecedented pace from 3.8% in 2009 to certified 24%> in 2019.[23,26] This outstanding increase in PCE have been achieved by tailoring the perovskite compositions like mixing the cations and/or halides which resulted in an improvement in optoelectronic and photovoltaic performance of the perovskite solar cells. More recently the NREL chart is updated with a perovskite new record of 25.2%.[26] These mentioned results are all from solution processed solar cells. As mentioned before, consumption of hazardous solvents, reproducibility and scalability are drawbacks of the solution processing methods. Thereby, vacuum based fabrication methods gained a huge attention very recently. The highest value reported so far for the fully vacuum deposited perovskite solar cells is 20.3% from a planar $MAPbI_3$ cell[15] and 15.9% from a mixed halide perovskite solar cells[17] suitable for tandem applications.
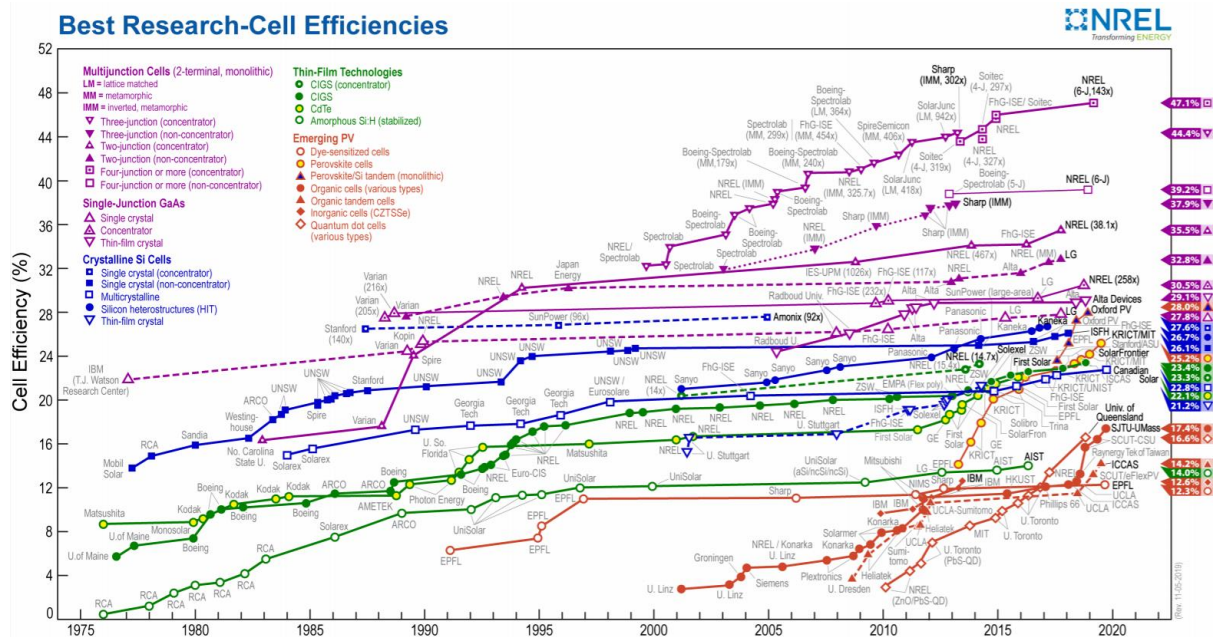
Figure 5. NREL chart for the best solar cell efficiencies.[16]

1.6 Other optoelectronic applications of perovskites

The band-gap tunability characteristic of peroskites made them good candidates for a variety of applications out of photovoltaics. Light emitting diodes,[68-69] lasers,[70] sensors[71] and photodetectors[72-73] as well as X-ray[74] and particle detection[75] are examples of widespread applications of perovskites.

1.7 Challenges for industrialization of perovskites

Perovskites need to address some challenges on the way of industrialization. Stability for instance is the main issue in perovskite devices fabrication. Perovskites are humidity,[76-77] light and temperature sensitive,[78] therefore they are prone to severe degradation while being exposed to ambient situation. Moreover, highly efficient perovskites are lead-based materials and lead is a toxic element

with high solubility in water. All these issues bold the importance of good encapsulation to mitigate the chance of degradation and environmental pollution in a long term use. Nevertheless, widespread investigations have been done recently upon stability enhancement by perovskite composition engineering as well as improvements in encapsulation materials and methods.[79-81] However, still these challenges are not fully answered and more investigations are required.

Besides stability and toxicity, scalability is another important matter to accelerate the perovskites commercialization. So far all the reported record efficiencies have been achieved with the solar cells having small active areas <1 cm^2, which is sufficient for proof-of-concept. Regarding industrial applications it is crucial to realize the perovskite devices on large areas with high throughputs.[82-83] Over past few years, significant progress have been done for instance in roll-to-roll,[84-85] spray coating,[86] doctor blading,[87] ink-jet printing[88] and evaporation deposition methods[15-21] but still the efficiencies are far behind the reported efficiencies on lab scale devices. This requires intensive investigations to realize higher efficiencies on larger areas making them cost-effective for commercial applications.

1.8 Motivation and goals of this thesis

The efficiencies of perovskite solar cells are mainly limited by their Voc values due to nonradiative recombination.[101-102] In recent years many investigations have been done on the recombination in perovskite solar cells suggesting that the

defects at perovskite bulk (grain boundaries) and interfaces between perovskite absorber and charge transport layers are the possible reasons for nonradiative recombination.[40-45] To tackle this important loss mechanism and to boot the efficiency of the perovskite solar cells a detailed understanding of the underlying physical process is necessary. Therefore, the main scopes of this thesis are (1) investigation on how to modify the grain growth and layer formation, and (2) interface engineering by optimization of charge transport layers targeting the bulk and interface defects passivation. Hybrid two-step evaporation-spincoating method is chosen for fabrication of perovskite solar cells in this thesis. Development of this fabrication method is important, which enables deposition of perovskite layer on textured surfaces, this is important for deposition of perovskite on highly efficient silicon bottom cells with textured front surfaces in a tandem configuration. So far only few papers are published reporting perovskite solar cells fabrication with this method. Tao et al[18] presented a PCBM-based electron transport layer with efficient charge extraction leading to 17.6% stabilized efficiency. This was the highest efficiency reported for the single junction perovskite solar cells fabricated with hybrid method at the time of starting this thesis work. Sahli et al[22] recently deposited a high band-gap CsFA-based mixed cation perovskite layer on top of a textured heterojunction silicon bottom cell yielding efficiencies beyond 25%. Improving the efficiency of perovskite/silicon tandem solar cells to surpass the single junction efficiency limits is an outlook for this thesis.

Chapter 2 : Experimental techniques

2.1 Perovskite solar cells fabrication

To fabricate the perovskite solar cells, FTO (fluorinated tin oxide) coated glass substrates were cleaned through sequential cleaning steps using an ultrasonic bath. The substrates were sonicated first in a 1% Hellmanex solution followed with two times sonication in deionized water. Then cleaning procedure continued with sonication in isopropanol, acetone and again isopropanol respectively. Each step was done for 10 minutes. Immediately after cleaning, the substrates were heated at 400 °C for 20 minutes.

A compact 30 nm TiO_2 hole blocking layer was deposited by electron beam evaporation. To create an electron transport bilayer, a 10 mg PCBM in 1 ml anhydrous chlorobenzene solution was prepared and deposited atop TiO_2 by spinning at spin speeds ranging from 1000 rpm to 4000 rpm for 30 s followed by

a 10 min annealing at 80 °C. The PCBM deposition and annealing was done under nitrogen atmosphere in a glove box.

The perovskite layer was deposited via a two-step hybrid evaporation-spincoating method. Accordingly, a 185 nm PbI_2 layer was thermally evaporated at ~10^{-6} torr vacuum pressure and a constant deposition rate of 0.5 Å/s. During deposition, the substrate temperature was kept at 20 °C. MAI solution was prepared by dissolving 40 mg MAI in 1 ml IPA. To convert the PbI_2 porous layer into perovskite, MAI solution was spin-coated at 2000 rpm for 35 s followed by 90 min annealing at 100 °C. Just before spincoating the solution was filtered with a PTFE 0.45 μl filter to remove undissolved MAI particles.

The Spiro-OMeTAD hole transport layer (HTL) solution was prepared by dissolving 72.3 mg Spiro-OMeTAD in 1 ml anhydrous chlorobenzene and doping with 28.8 μl 4-tert-butylpyridine and 17.5 μl from a stoke solution of 520 mg lithium bis(trifluoromethylsulphonyl)imide dissolved in 1 ml acetonitrile. The HTL layer was spun at spin speeds of 2000 rpm for 30 s. Afterwards the samples where left in ambient air over night for HTL oxidation.

Finally, 80 nm gold electrodes were thermally evaporated at ~10^{-6} mbar vacuum pressure.

The materials used for fabrication of the solar cells were as follow:

Spiro-MeOTAD, [6,6]-phenyl-C_{61}-butyric acid methyl ester (PCBM), bis (trifl uoromethane) sulfonimide lithium salt (Li-TFSI,99.95%), 4-tertbutylpyridine (96%), chlorobenzene (≥99.5%), and acetonitrile (anhydrous, 99.8%) were purchased from Sigma Aldrich. Lead (II) Iodide (PbI_2, 99.99%) was purchased from Tokyo Chemical Industry (TCI). Methylammonium iodide (MAI) was purchased from Greatcell Solar, and isopropanol (anhydrous, 99.5+%) was purchase from Alfa Aesar.

The two-step hybrid evaporation-spincoating method was used to fabricate the perovskite solar cells with an n-i-p structure shown in figure 6.
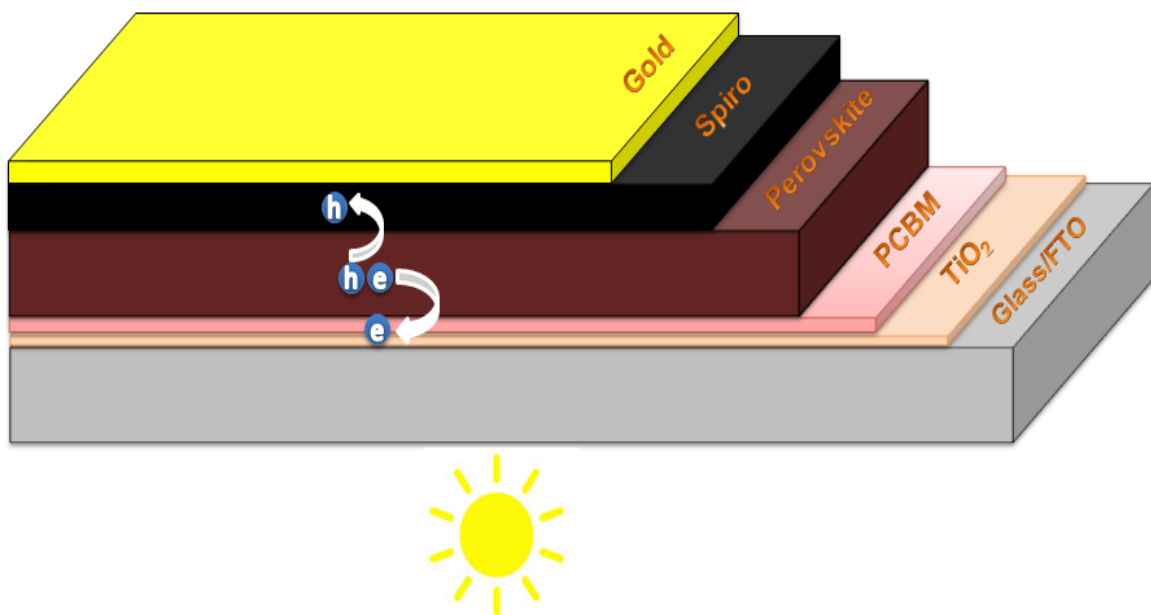

Figure 6. Schematic of the perovskite solar cell fabricated in this thesis.

2.2 Structural investigation

2.2.1 X-ray diffraction

XRD measurements were performed with a PANalytical Empyrean 2 diffractometer with Copper K alpha 1 radiation (lambda = 0.154060 nm). A PIXcel-3D detector was used in "receiving slit mode" with a range of 1.0 mm. 2theta-theta-scans with step size of 0.02 degree and integration time of 1s were recorded.
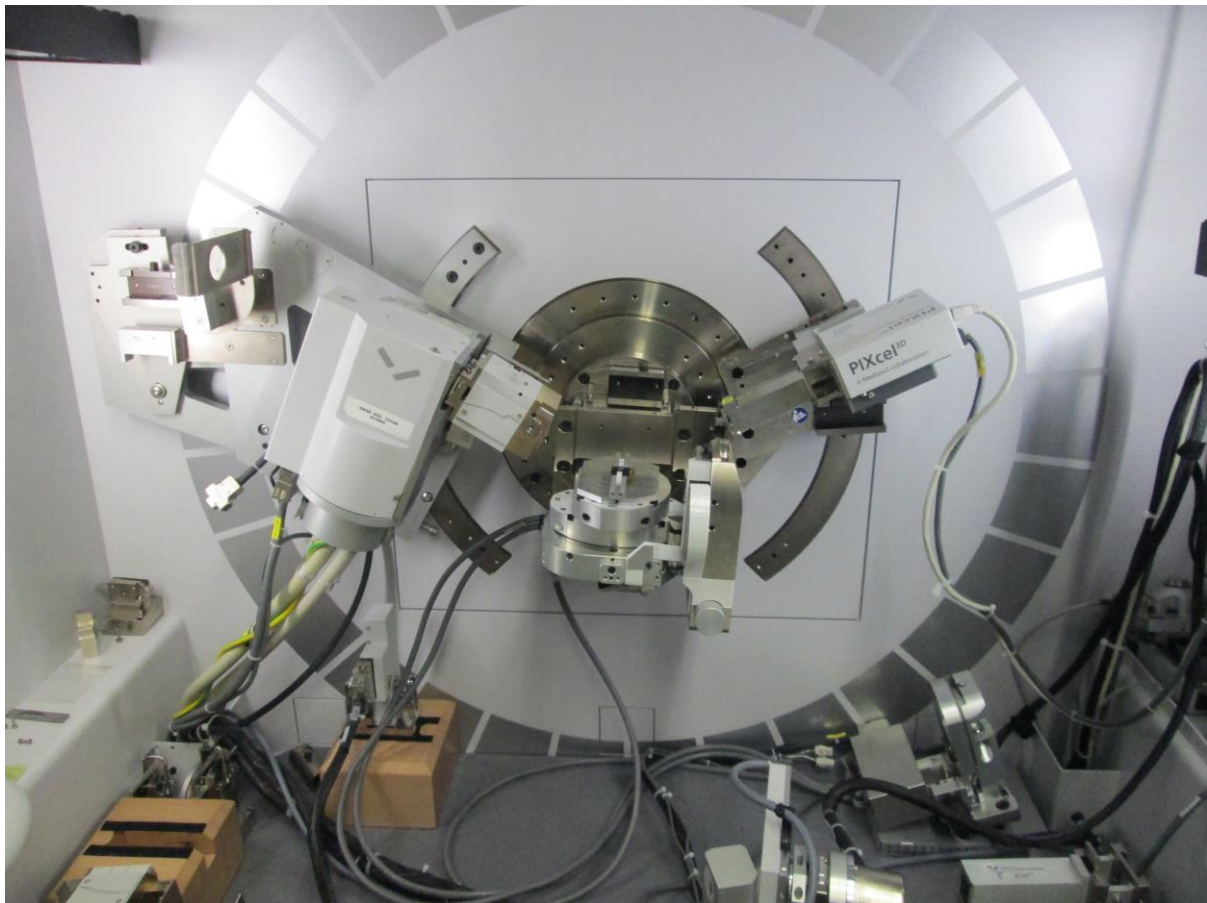

Figure 7. XRD setup used in this thesis. This setup was used in the Fraunhofer IAF.

2.2.2 Scanning electron microscopy

SEM images were taken using a Zeiss Auriga 60 Crossbeam Workstation, field emission SEM with InLens detector at 5 kV acceleration voltage.
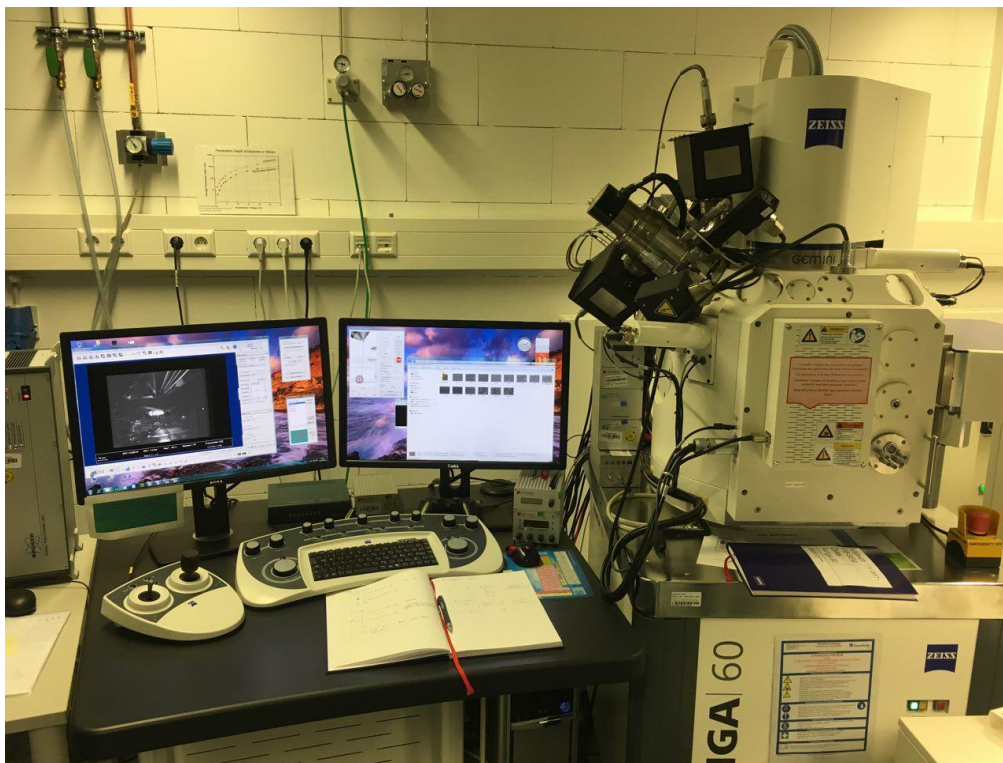

Figure 8. SEM setup used in this thesis. This setup is used in the Fraunhofer ISE.

2.2.3 Atomic force microscopy

The AFM images were taken via a Bruker dimension edge AFM. The measurements have been done in the tapping mode over 10×10 µm surface area of the samples with 512 data points each line.
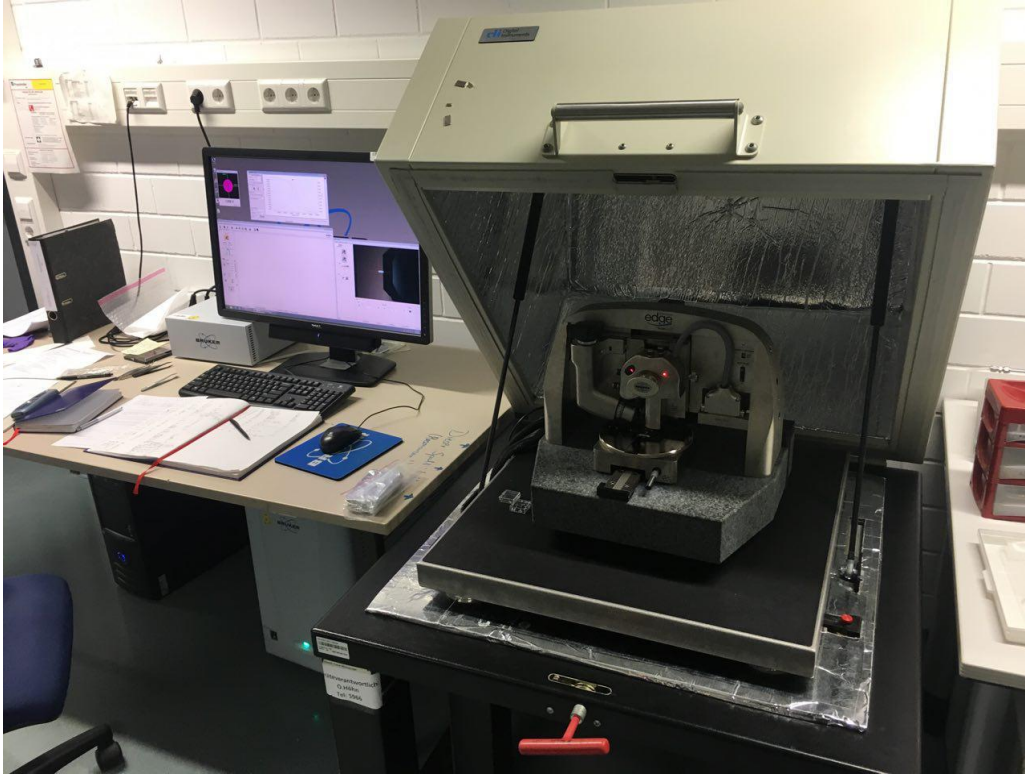
Figure 9. AFM setup used in this thesis. This setup is used in the Fraunhofer ISE.

2.3 Optical measurements

2.3.1 Optical properties

Reflection and transmission optical properties were measured utilizing a Lambda 950 UV/Vis spectrophotometer.

Figure 10. Spectrophotometer setup used in this thesis. This setup is used in the Fraunhofer ISE.[103]

2.3.2 Photoluminescence spectroscopy

Transient photoluminescence decay spectra were measured using a fiber coupled confocal microscope. A pulsed laser diode (635 nm, 0.26 mW, spot diameter 0.2 mm) was used for local excitation. The emitted light was detected using a silicon single photon avalanche diode. The optical components in the light path from laser to detector were: laser band-pass filter 635 nm, cold-light mirror, sample, focusing lens with a numerical aperture of 0.26, cold-light mirror followed by 650 nm long-pass filter for suppressing spurious laser light, Ø 100 µm pinhole.

The spectrally resolved detection can be applied in a fixed position and monitored over time with measurement frequencies up to 100 Hz, thereby allowing to track the spectral evolvement of the signal over milliseconds up to several hours. For this purpose, Time-Correlated Single Photon Counting (TCSPC) is used to

determine the photoluminescence lifetime. In TCSPC, one measures the time between sample excitation by a pulsed laser and the arrival of the emitted photon at the detector.

To do spectrally resolved photoluminescence measurements a movable x-y-z stage was mounted below the lens to map the sample. To get highest spatial resolution, a piezo-stage was used, allowing steps in the sub-micrometer range. Controlling the height of the stage during the mapping is crucial for an efficient collection exclusively from the focal plane.

All measurements were performed in ambient conditions with no significant temperature increase related to the sample illumination.

2.4 Electrical measurements

2.4.1 Current-voltage characteristics

A SINUS–220 PRO solar simulator from WAVELABS with LED lamp was used to measure the photovoltaic performance. The solar spectrum was calibrated to 1sun (100 mW/cm^2) using a reference silicon solar cell. Current-Voltage (J-V) characteristics were measured in reverse and forward scan directions respectively with a slow scan rate of 43 mV/s. Stabilized measurements were done, with the voltage fixed at the maximum power point as determined from the average of J-V scans. A shadow mask was used during the measurements to define a 0.16 cm^2 active are.

Chapter 3: Two-step hybrid evaporation-spincoating fabrication method

To prepare the perovskite films, a two-step hybrid evaporation-spincoating method was utilized. In a first step, the PbI_2 was deposited via thermal evaporation, which is subsequently converted into a perovskite layer by MAI spincoating. To improve the crystallization quality and form a uniform and compact layer, the two-step was followed by an annealing process at 100 ℃. Due to the porosity of PbI_2 layer, intercalation of MAI was effective. The perovskite layer formed with this method was compact and pinhole free. This was achievable with a rather simple process because unlike solution processing methods where a precise stoichiometry is crucial to form a crystallized and compact perovskite, here only isopropanol (IPA) solvent (for dissolution of MAI) was used. Therefore controlling the MAI/PbI_2 ratio was much easier in hybrid method. The MAI/PbI_2 ratio is important because it plays an important role on the quality of crystallization, grain size and surface morphology.

3.1 Optimization of charge transport layers

Besides the importance of a compact and highly crystallized perovskite layer formation, considerable attention had to be paid to the charge transport layers. This is because without implementation of an appropriate charge transport layer, the charge carrier collection and thereupon output efficiency would be negatively affected. Therefore, in this thesis the role of interface engineering at perovskite and charge carrier interfaces is investigated. Moreover, optimization study is performed on the TiO_2/PCBM electron and Spiro-MeOTAD hole transport layers of the perovskite solar cell.
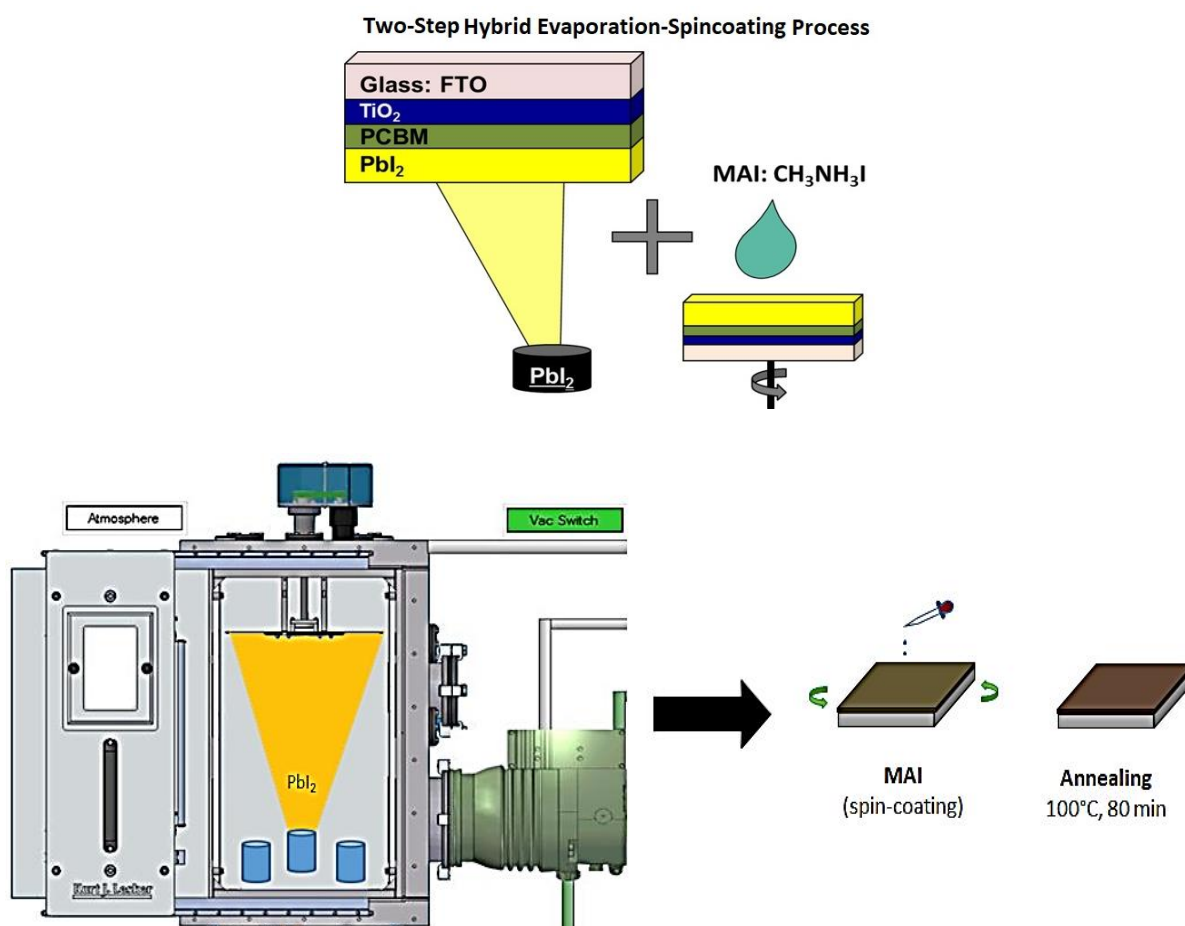

Figure 11. Schematic of hybrid evaporation-spincoating method.

3.1.1 Optimization of TiO$_2$/PCBM Electron Transport Layer

Fullerene derivatives such as PCBM or C60 are known to be passivation layers for TiO$_2$ or SnO$_2$ metal oxides.[45] The combination of fullerene derivatives with metal oxides to form an electron transport bilayer is extremely important for the performance of the solar cell. This is because in general, the dissociated charge carriers and here the electrons need to be injected into ETL very fast before being recombined with holes. Implementation of a bi-layer like TiO$_2$/PCBM paves the electron transport paths while blocking the hole transport paths. This leads to a mitigation of the non-radiative losses and also intrinsic hysteresis defect. In this thesis, the role of TiO$_2$/PCBM as ETL on the photovoltaic performance of MAPbI$_3$ perovskite solar cells has been investigated. Optimization studies were done to understand the optimum thickness ratio of TiO$_2$/PCBM combination. A 30 nm TiO$_2$ thickness was kept constant while to modify the PCBM thicknesses, throughout the optimization studies, deposition spin speeds were varied ranging from 1000 rpm to 4000 rpm.

X-ray diffraction (XRD) patterns of the perovskite layers deposited atop spun PCBM with different spin speeds are depicted in Figure 12.
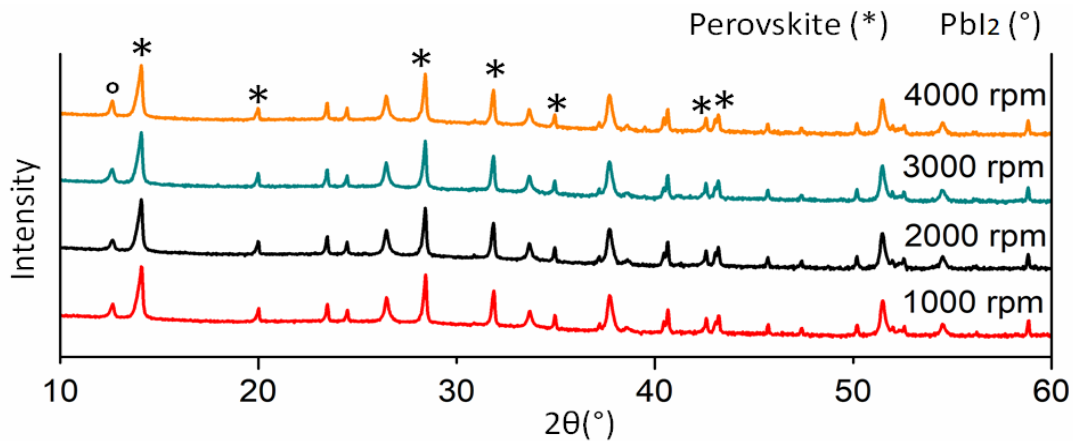
Figure 12. X-ray diffraction patterns of the perovskite layers deposited on spun PCBM with different spin speeds.

As can be seen, the formed layers were well crystallized and the known perovskite peaks (marked with stars) were appeared. Also the PbI_2 peak (marked with a circle) was appeared at around $12.67°$. The presence of PbI_2 peak is reported to be beneficial for the solar cell performance. Although, too intensive or too small peaks towards no peak is detrimental.

The compactness of the formed perovskite layer is one of the advantages of hybrid deposition method. This is illustrated in Figure 13, where the crystal grains are strongly impinged into each other and formed a pinhole-free layer.
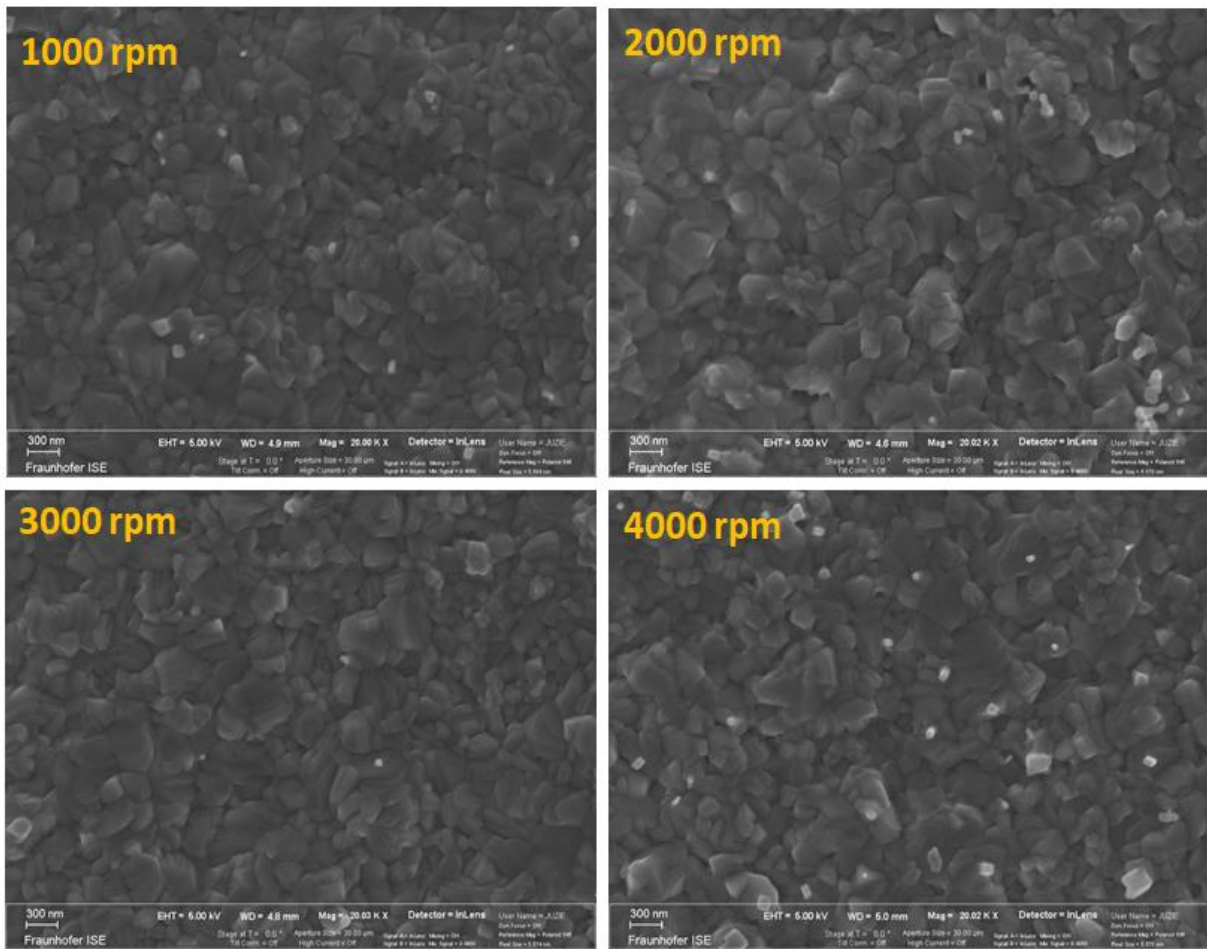
Figure 13. SEM top view images of the perovskite layers deposited on spun PCBM with different spin speeds.

As it can be seen, there was a slight difference in crystal grain sizes of perovskite layers formed on PCBM spun with different spin speeds. The crystal grains were very small in perovskite layer deposited on thick PCBM (1000 rpm). By increasing the spin speeds to 2000 rpm and 3000 rpm, larger and more impinged grains formed during the layer ripening. In the perovskite layer deposited atop thin (4000 rpm) PCBM, a combination of large and small grains formed. This

difference in nucleation and gains growth could be associated to surface strains imposed by different substrate thicknesses. The perovskite layers formed atop spun PCBM with 2000 rpm and 3000 rpm (~ 30-40 nm) spin speeds looked more homogenous than a very thick or a very thin PCBM.

To have an in-depth understanding of perovskite grains growth on different PCBM layer thicknesses, atomic force microscopy (AFM) measurements were performed. Figure 14 presents the AFM images of the perovskite layers formed atop PCBM spun with different spin speeds.
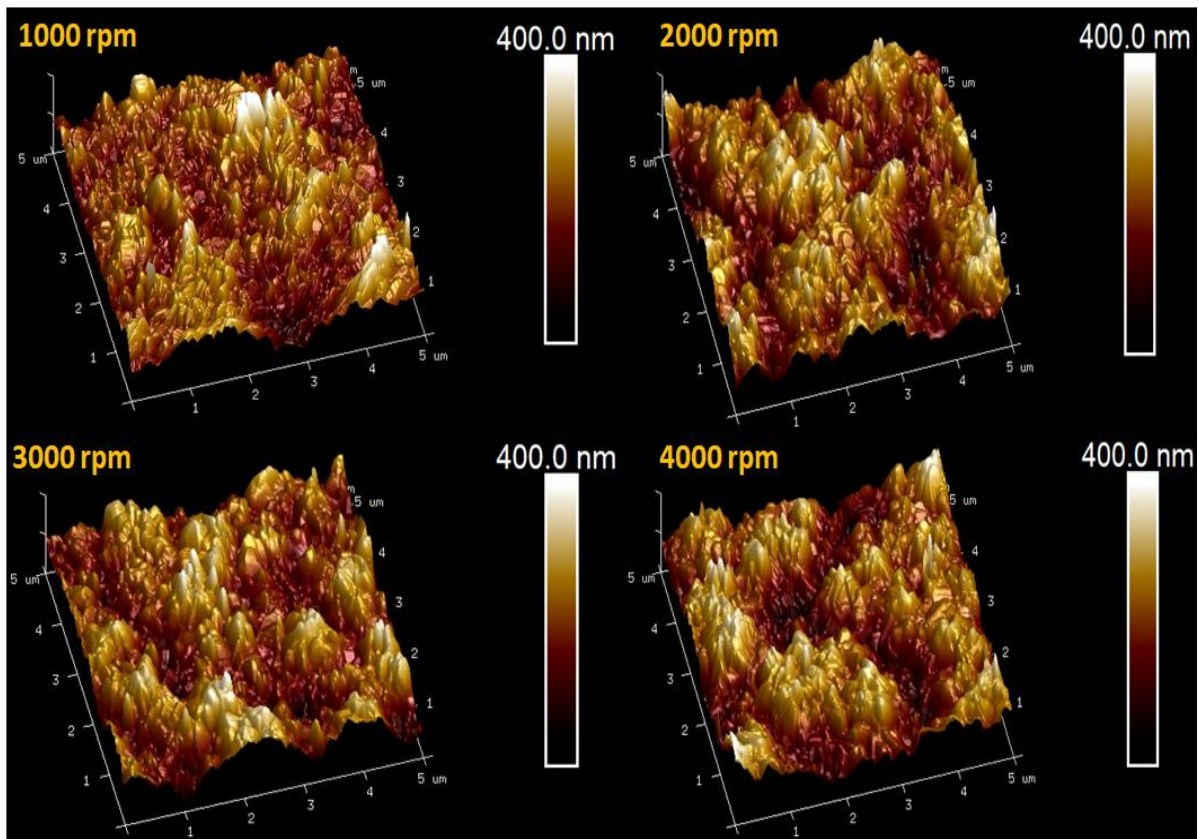

Figure 14. AFM images of the perovskite layers deposited on spun PCBM with different spin speeds.

Looking carefully at the crystal grain growth mechanism, AFM images supplied a close analogy to SEM images. As can be seen in AFM images, more

homogenous layers were formed atop 2000 rpm and 3000 rpm spun PCBM while smaller grains formed in case of 1000 rpm and a combination of small and large grains with huge roughness in case of 4000 rpm.

The TRPL measurements (Figure 15) were performed on perovskite layers deposited atop PCBM spun with different spin speeds. A bi-exponential decay model was used to fit the PL decay data and extract the life time values (Figure 16). The fitting was done over 6-10 TRPL curves of each PCBM spin speed. The fast life time components were in the range of few hundred picoseconds independently from the spin speed. On the other hand, there were significant differences for the slow components (t_2). The highest mean life time of 19±3 ns was determined for the sample with 3000 rpm, which coincides with the highest efficiency. Accordingly, the shortest life time of 12±3 ns was determined for 1000 rpm, where we also found the lowest efficiencies. If short decay times were the result of an increased recombination at the interface or in the perovskite volume, we would expect that short life time values correlate with low Voc. However, no such correlation could be found. On the other hand, if long life times would be a sign of good charge extraction, we would see a positive correlation with the Jsc, as it is indeed present in our data. This is somehow surprising, as a quenched PL signal has been identified in literature previously as a sign of good charge extraction. A possible explanation is that in the case of efficient charge extraction electrons are first extracted from the perovskite via the PCBM/TiO$_2$ interface and then re-injected into the perovskite when the electron concentration has decreased

due to (radiative) recombination in the perovskite. This would result in an apparent longer lifetime. However, in order to test this hypothesis extensive additional characterization would be necessary.
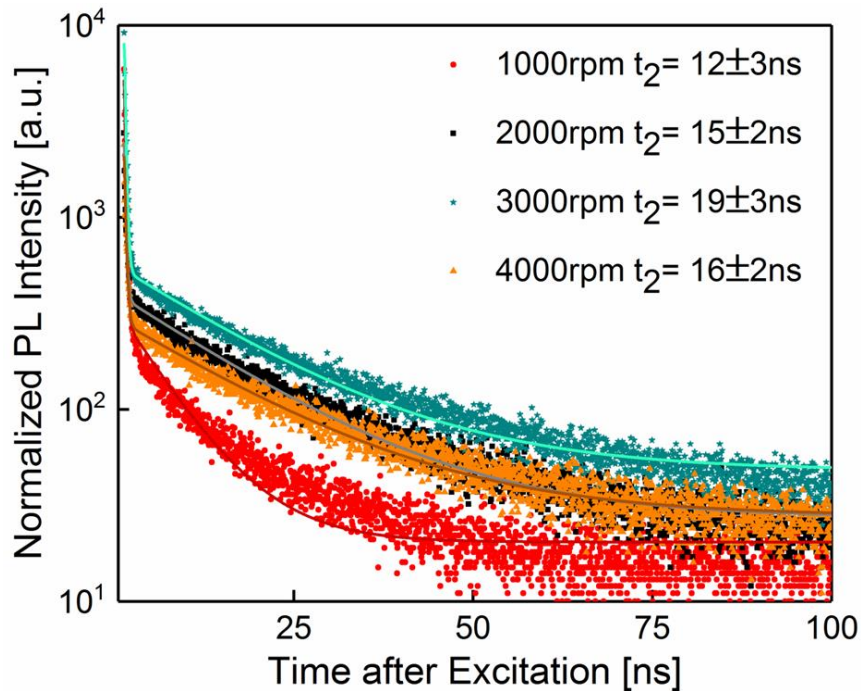

Figure 15. TRPL curves of the perovskite layers deposited on spun PCBM with different spin speeds.

Steady state PL and light beam induced current (LBIC) measurement were performed on completed devices made with 1000 and 3000 rpm spun PCBM layers. From the PL measurements, the PL intensity as well as the spectral position of the peak were determined, which are typically associated with the splitting of the Quasi-Fermi levels and hence the presence of recombination pathways, and the bandgap of the perovskite, respectively. The LBIC imaging gives spatial information about the charge generation and extraction. As can be

seen in Figure 16, a more homogeneous layer is formed in case of PCBM deposition with 3000 rpm spin speed compared with 1000 rpm. A precise interpretation of the spatial information, however, is difficult. Regions can be found where a low LBIC signal coincides with high PL intensity, e.g., for the edges of both devices. This could point to problems with the charge extraction. If compared on the device level, PL intensity is also higher in average for the sample spun with 1000 rpm than with 3000 rpm. This would fit to the observation of higher voltage but lower current and FF for the sample with 1000 rpm compared with 3000 rpm. On the other hand, there are also regions where high LBIC signal coincides with high PL intensity especially for the sample produced with 3000 rpm (labeled with a star). One could argue that in this case charge extraction is sufficiently good, so observed inhomogeneities are being caused by differences in the crystal quality or surface passivation. However, there are also structures clearly visible in both PL intensity and peak position that apparently do not affect charge extraction at all, e.g., the set of lines visible on the 3000 rpm sample. Overall, one can conclude that a balance has to be reached between effective charge extraction, crystal quality, and interface passivation to simultaneously achieve high Voc, FF, and Jsc and thereby the highest PCE.
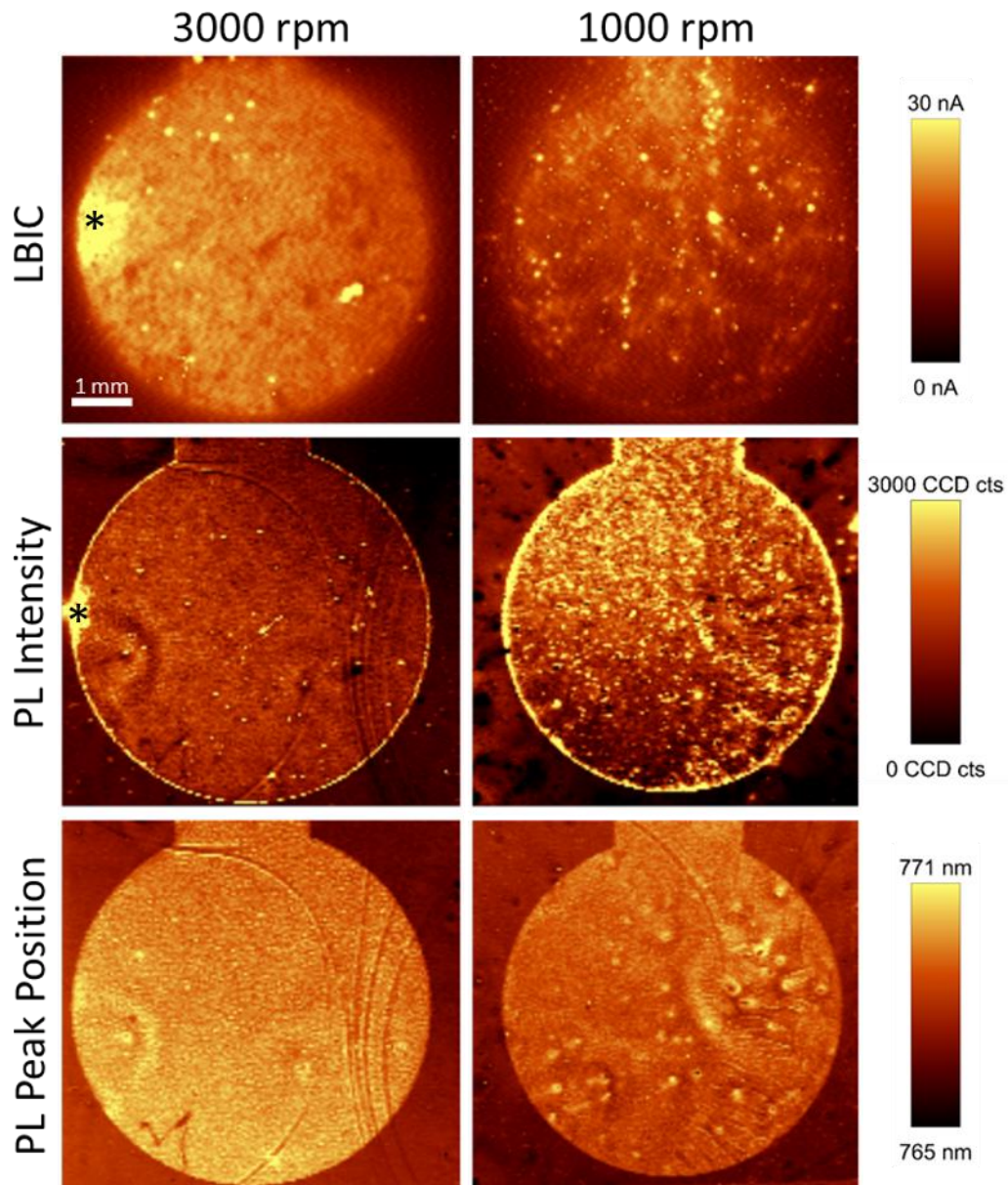
Figure 16. Steady state PL measurements of the perovskite layers deposited on spun PCBM with 1000 and 3000 rpm spin speeds.

As the initial argumentation was that an important clue for high performance lays at the perovskite/charge carrier interfaces, the photovoltaic performance of the

solar cells implementing different thicknesses of PCBM and Spiro-MeOTAD charge transport layers, was analyzed. The main photovoltaic figures of merit are depicted in Figure 17.
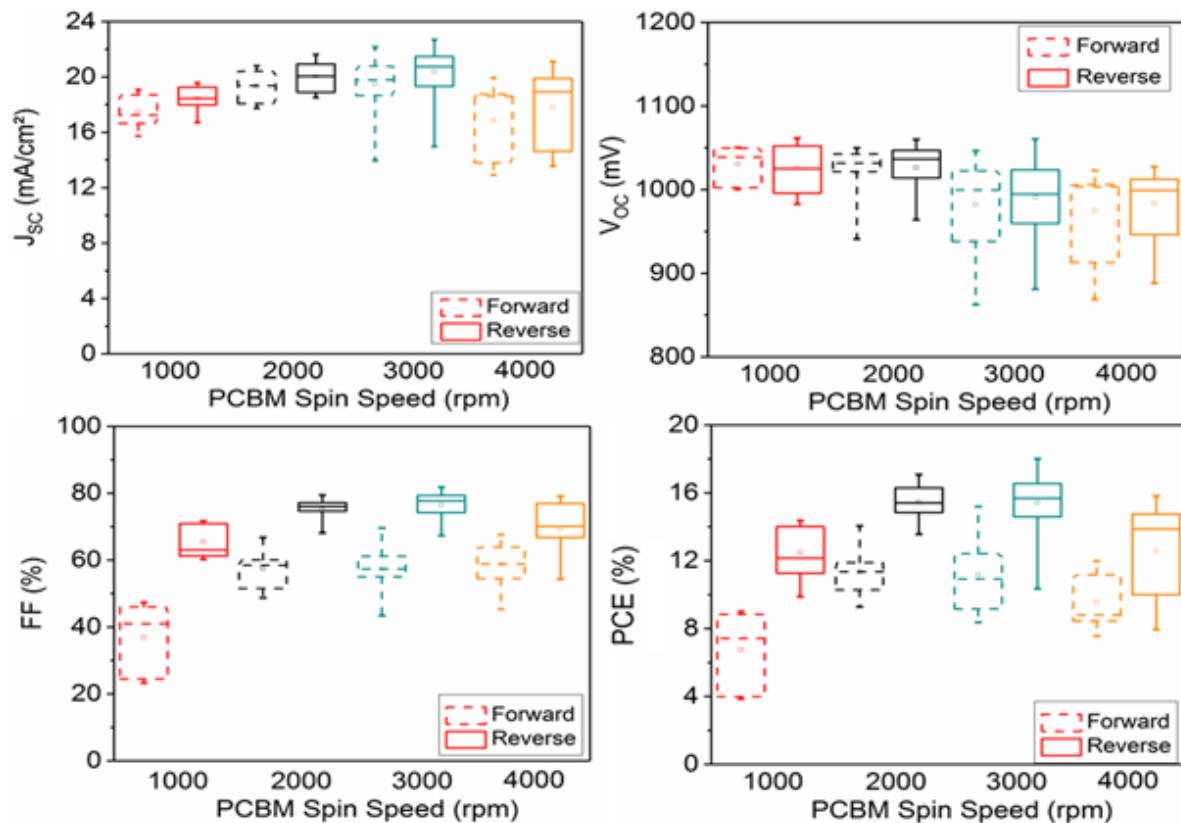

Figure 17. The photovoltaic parameters of the perovskite solar cells fabricated with PCBM layers deposited with different spin speeds.

As it can be seen, for all photovoltaic parameters, the perovskite solar cells made atop PCBM spun with 2000 rpm and 3000 rpm showed higher performances than 1000 rpm and 4000 rpm. Based on the results, the 3000 rpm was convincingly the best recipe for PCBM deposition. Comparing the short circuit current (Jsc)

values, the higher values measured for PCBM deposited with 3000 rpm and 2000 rpm spin speeds, were due to a compact and more homogenous perovskite absorber layer formation. Moreover, the lowest currents measured in case of 1000 rpm could be associated to the small perovskite crystal grains formation. The combination of larger and smaller grains in case of 4000 rpm resulted in slightly better Jsc values while for homogenous and larger grains in case of 2000 rpm and 3000 rpm the results were improved. The Voc values for 4000 rpm was lower than the other spin speeds. Based on AFM measurements, roughness was the significant difference of perovskite layers formed atop 4000 rpm spun PCBM with the other spin speeds. Thereby, in case of 4000 rpm, a perovskite layer with less homogeneity was formed with deep valleys between crystal grains which may act as recombination centers and decrease the Voc. In the same manner as Jsc and Voc, FF values in case of 3000 rpm were the highest. This could be associated to an effective passivation of interface trap states by PCBM layer as well as a good electronic coupling between perovskite absorber and electron transport bilayer, which enabled an efficient electron transport. Finally the champion PCE is achieved from the solar cells fabricated with PCBM spun at 3000 rpm.

3.1.2 Optimization of Spiro-MeOTAD hole transport layer

To optimize Spiro-MeOTAD deposition parameters, different spin speeds ranging from 1000 rpm to 6000 rpm were tested. Utilizing the optimum recipe for ETL, the perovskite solar cells were fabricated with different HTL thicknesses. Cross-section SEM images of these perovskite layers are shown in Figure 18.
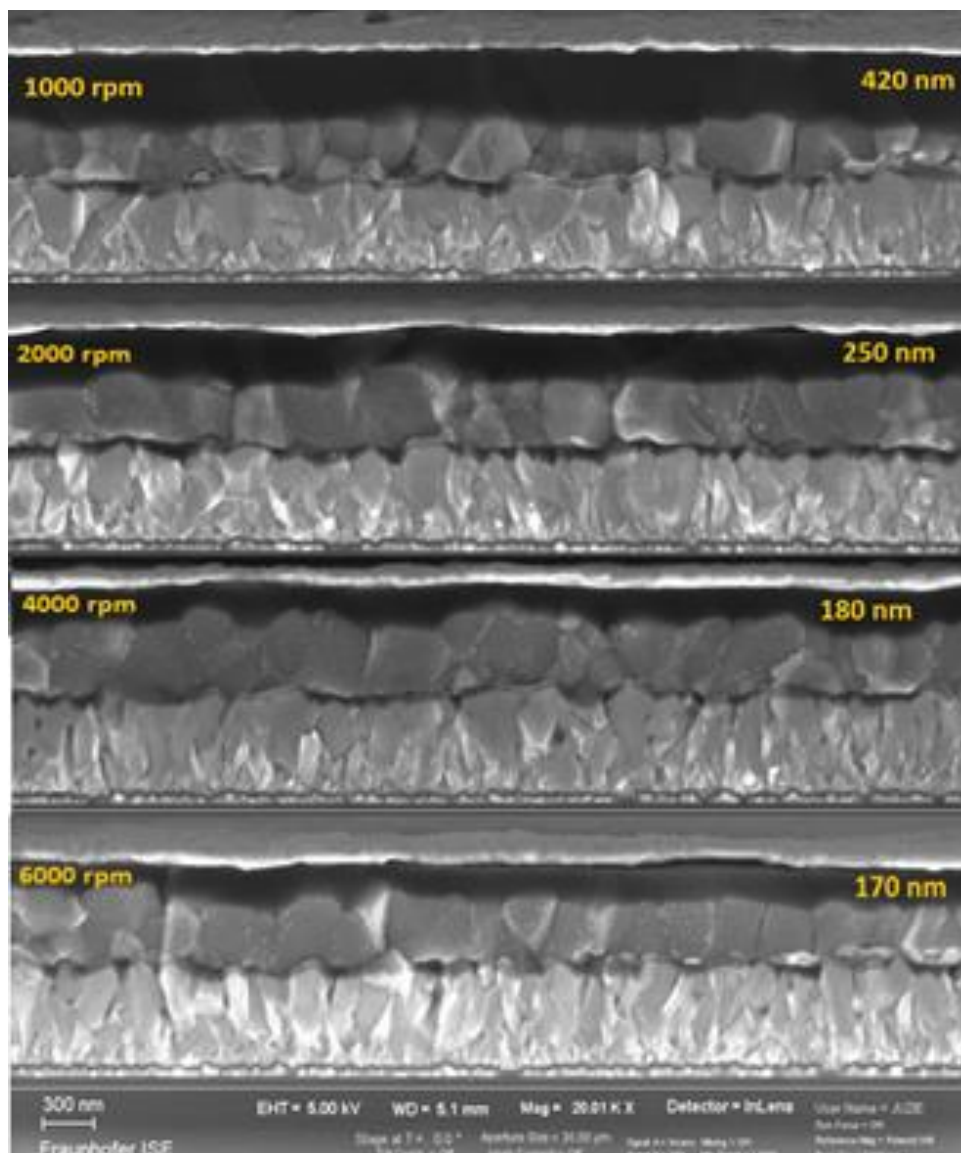

Figure 18. SEM cross-section images of the perovskite solar cells fabricated with different Spiro-MeOTAD spin speeds.

As can be seen in this figure, a very compact and highly crystallized perovskite was formed and very well covered by Spiro-MeOTAD layer.

Again, main photovoltaics figures of merit were measured and analyzed to understand the optimum deposition parameters for Spiro-MeOTAD. Figure 19 presents the photovoltaic parameters versus Spiro-MeOTAD deposition spin speeds. Convincingly, the 2000 rpm spin speed, has shown to be the optimum value. Comparing the results of HTL and ETL optimizations, a significant Voc gain and a slightly increase in Jsc were achieved by HTL optimization.
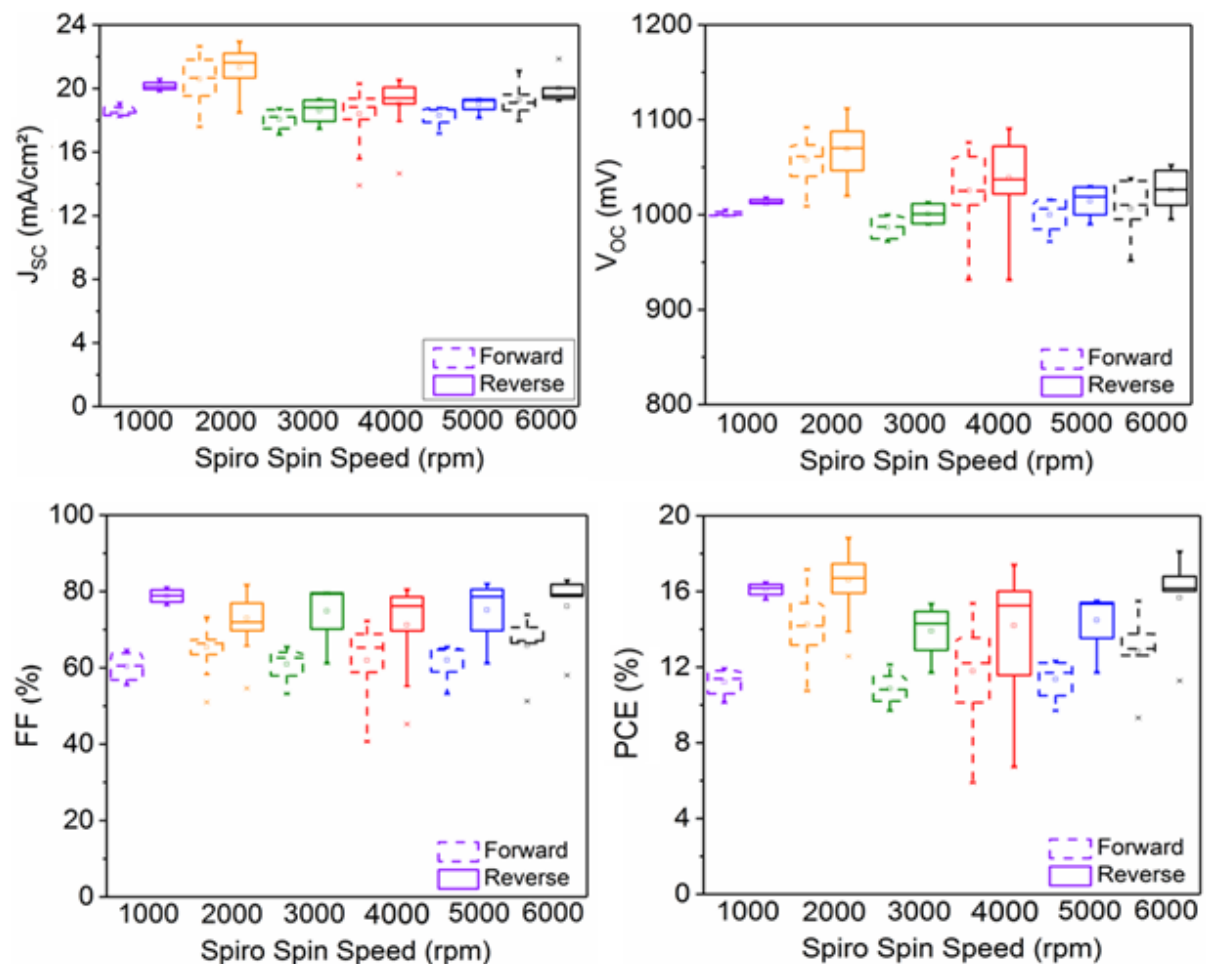

Figure 19. The photovoltaic parameters of the perovskite solar cells fabricated with Spiro layers deposited with different spin speeds.

By implementing the optimum recipes for charge transport layers, using the two-step hybrid fabrication method, perovskite solar cells were fabricated. Figure 20 presents the current-voltage characteristics of the champion cell along with the stabilized power conversion efficiency at the maximum power point. As can be seen, an 18.2% stabilized efficiency has been achieved. This efficiency have been achieved as a result of optimization on perovskite layer and HTL which is discussed in section 3.2 and 3.3.
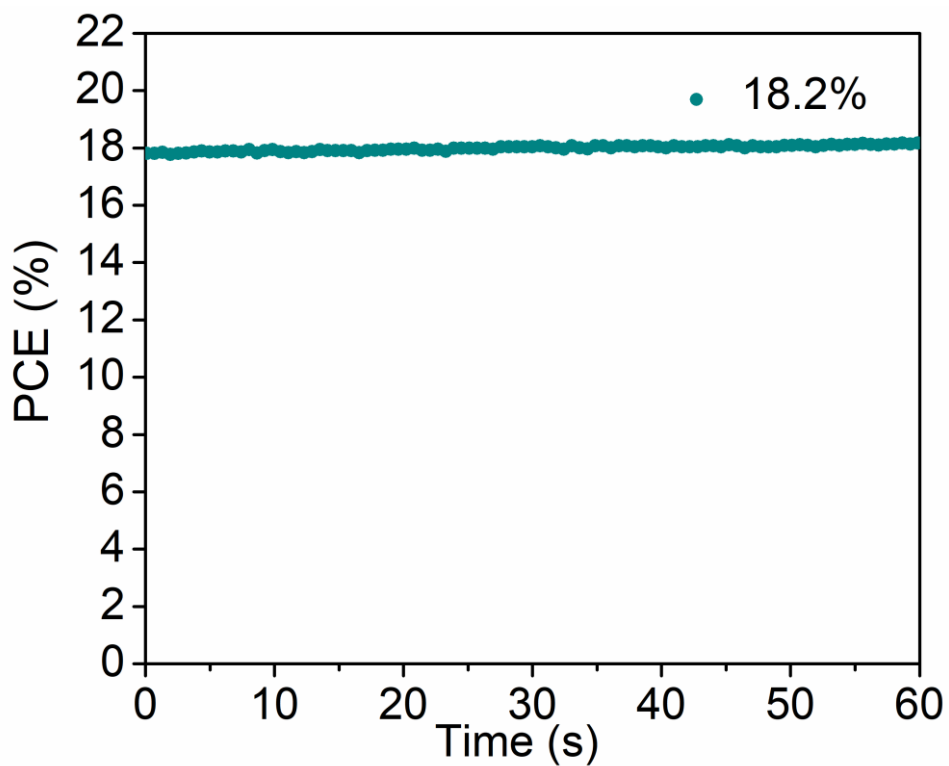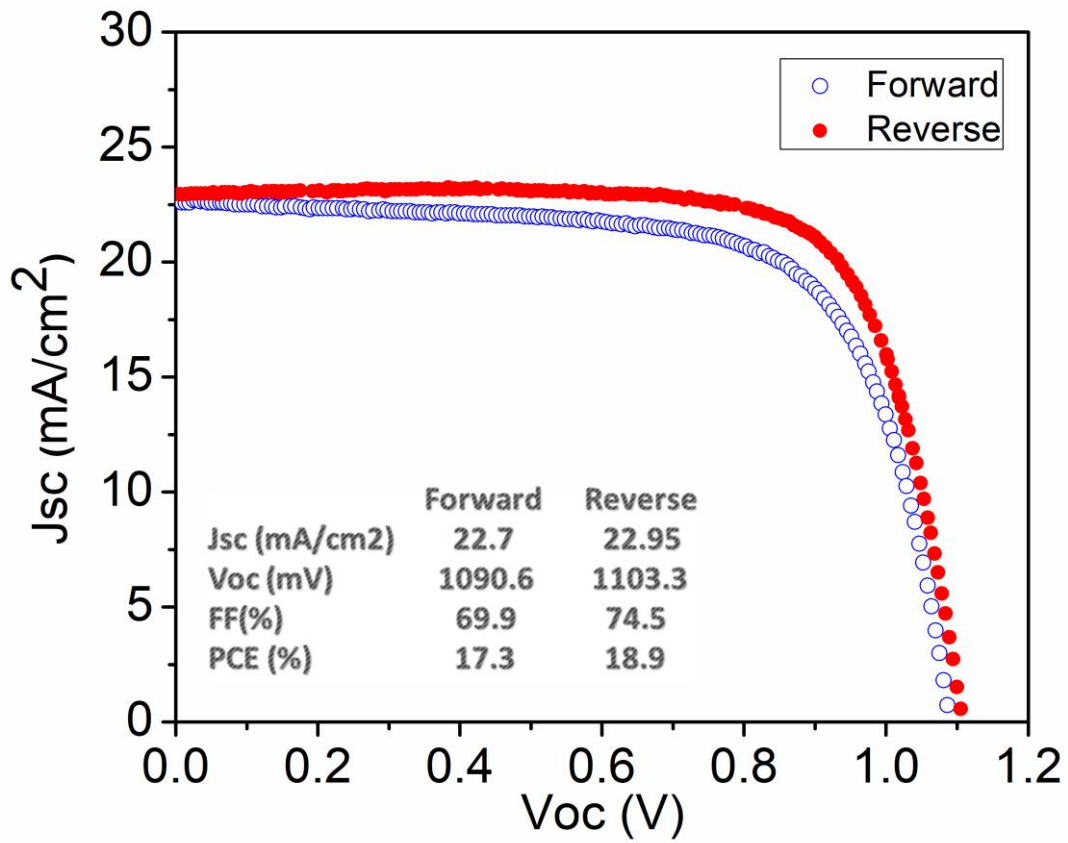
Figure 20. J-V (a) and stabilized PCE (b) curves of the solar cells measured

with scan rate of 43 mV/s.

External quantum efficiency (EQE) spectra of the champion cell was measured with a custom-made spectral response set-up where the samples were irradiated with chopped light and the response was measured with a lock-in amplifier (Figure 21). Both J-V and EQE measurements were carried out in air.
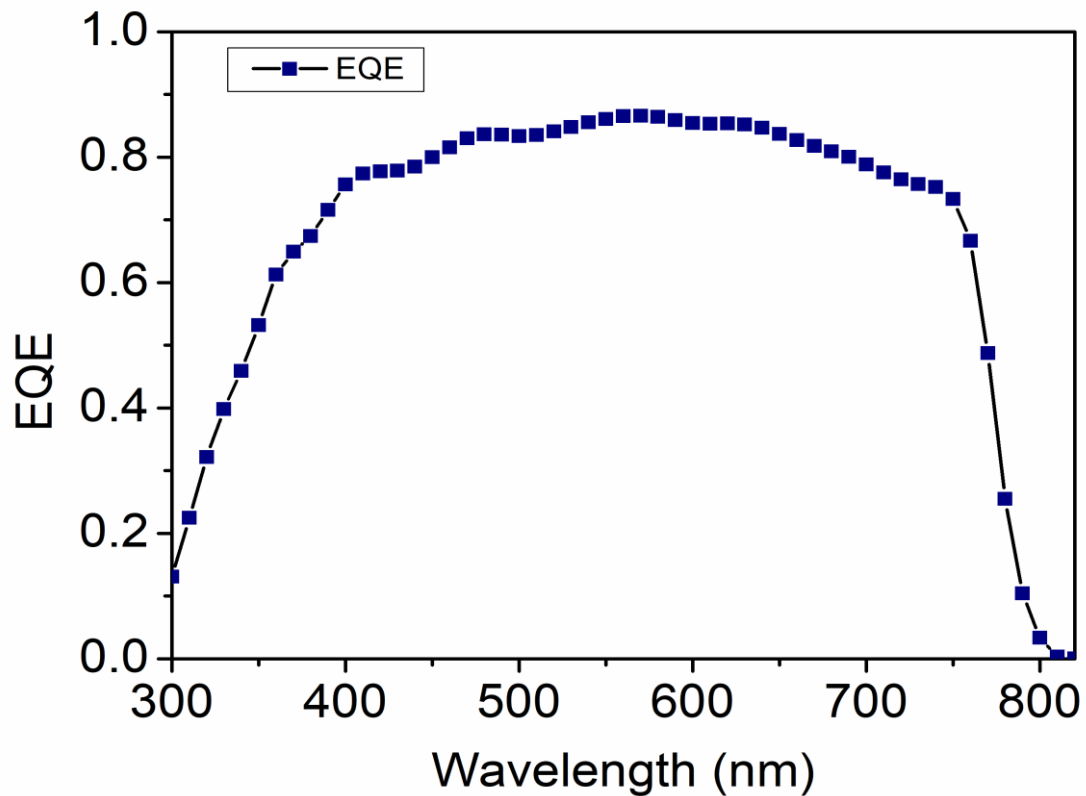

Figure 21. External quantum efficiency (EQE) of the champion solar cell.

3.2 The role of crystal growth conditions for achieving high efficiencies

With maturing of the fabrication methods, a deepened understanding of the factors determining PCE becomes more and more important for further improvements. Especially understanding of crystallization and layer ripening is crucial as those effects determine the occurrence of defect centers that could limit the performance. Accordingly, the role of excess PbI_2 in perovskite structures and its impact on crystallization quality, optoelectronic properties and photovoltaic performance of different perovskite solar cells has been studied recently.[89-93] However, among all these studies, perovskites produced via the highly reproducible and efficient two-step hybrid evaporation-spincoating deposition method have not been investigated.

Therefore, in this thesis the role of excess PbI_2 on the morphological properties and thereupon the photovoltaic behavior of $MAPbI_3$ perovskite solar cells produced via hybrid method has been investigated. X-ray diffraction (XRD) and scanning electron microscopy (SEM) were employed to study the crystallization quality and surface morphology. TRPL measurements were performed to evaluate the charge extraction quality. Finally, photovoltaic parameters of the cells were measured and compared.

FTO (fluorinated tin oxide) coated glass substrates were cleaned through sequential cleaning steps using an ultrasonic bath. The substrates were sonicated

first in a 1% Hellmanex solution followed with two times sonication in deionized water. Then cleaning procedure continued with sonication in isopropanol, acetone and again isopropanol respectively. Each step was done for 10 minutes. Immediately after cleaning, the substrates were heated at 400 °C for 20 minutes.

To implement a standard n-i-p structure (Figure. 22a), a 30 nm compact TiO_2 hole blocking layer was deposited via electron beam evaporation. Subsequently, to create an electron transport bilayer, a 10 mg/ml PCBM (Sigma-Aldrich) solution in anhydrous chlorobenzene (Sigma-Aldrich) was deposited atop TiO_2 by spin-coating at 3000 rpm for 30s followed by a 10 min annealing at 80 °C. The PCBM deposition and annealing was done under nitrogen atmosphere in a glove box. The combination TiO_2/C60 as an electron transport bilayer was also tested. A 30 nm layer of C60 (Solenne) was thermally evaporated atop a 30 nm evaporated TiO_2 layer at ~10^{-6} torr vacuum pressure.

The perovskite layer was deposited using a hybrid evaporation-spincoating two-step method. Accordingly, a 185 nm PbI_2 (Tokyo Chemical Industry) layer was thermally evaporated at ~10^{-6} torr vacuum pressure and a constant deposition rate of 0.5 Å/s. During deposition, the substrate temperature was kept at 20 °C. To convert the PbI_2 porous layer into perovskite, a 45 mg/ml CH_3NH_3I (MAI, Dyesol) solution in isopropanol was spin-coated at 2000 rpm for 35 s followed by 90 min annealing at 100 °C. Just before spin-coating, half of the MAI solution

was filtered by a PTFE 0.45 μm filter to remove undissolved MAI particles. The other half was used as it is.

The Spiro-OMeTAD hole transport layer (HTL) solution was prepared by dissolving 72.3 mg Spiro-OMeTAD (Sigma-Aldrich) in 1 ml anhydrous chlorobenzene and doping with 28.8 μl 4-tert-butylpyridine (Sigma-Aldrich) and 17.5 μl from a stoke solution of 520 mg/ml lithium bis(trifluoromethylsulphonyl)imide (Sigma-Aldrich) in acetonitrile (Sigma-Aldrich). The HTL layer was spin-coated at 2000 rpm for 30s. Afterwards the samples were left in ambient air over night for HTL oxidation.

Finally, 80 nm gold electrodes were thermally evaporated at $\sim 10^{-6}$ mbar vacuum pressure.
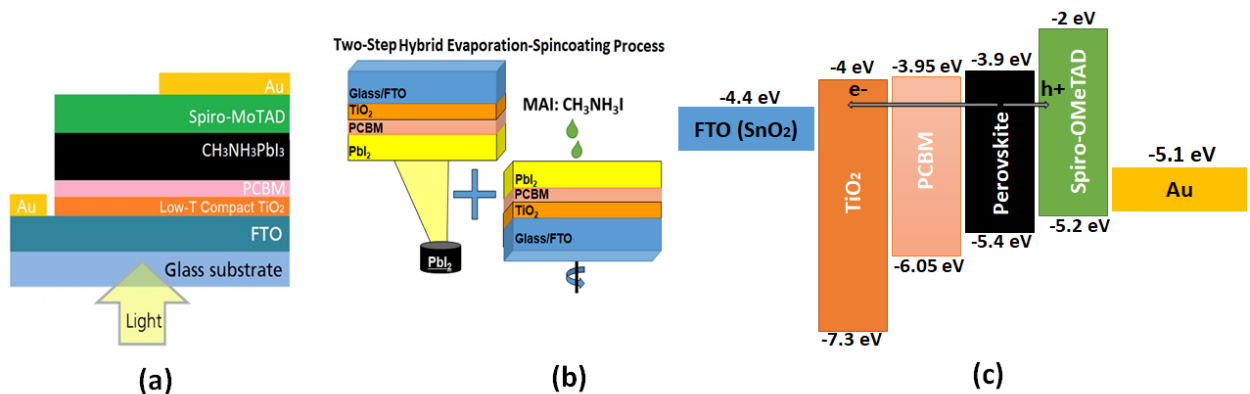

Figure 22. Schematic of the solar cell structure (a), the hybrid evaporation-spin coating two-step process (b) and energy band diagram of the material stack (c).

Figure. 23a presents the XRD pattern of the perovskite layer formed on a TiO_2/PCBM electron transport bilayer using the MAI solution without filtration. In contrast, Figure. 23b, presents the results for the perovskite layer using the filtered MAI solution. In both cases perovskite peaks are clearly visible, which indicates formation of the perovskite phase. Nevertheless, there is also a diffraction peak associated with (001) crystal orientation of PbI_2 at 12.67°. The intensity of the PbI_2 peak is stronger in case of the filtered MAI solution. This means that more PbI_2 is present in the perovskite structure.
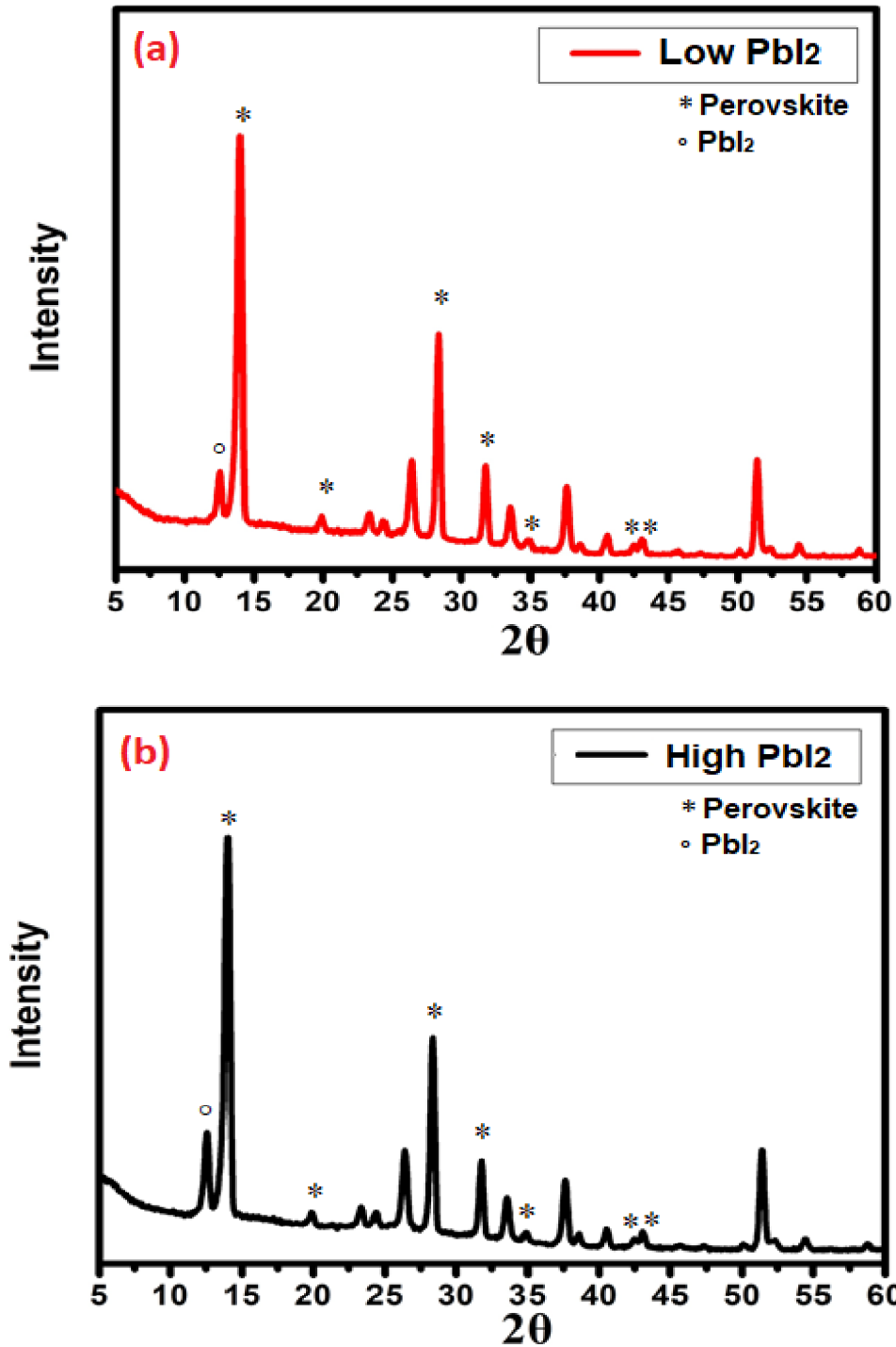
Figure 23. X-ray diffraction patterns of the perovskite layers fabricated with low and high PbI_2 contents.

Differences between the two samples are also visible in the SEM images (Figure. 25). Both top view SEM images show a compact perovskite layer formation, but

with a clear difference in nucleation quality and thereupon crystallites sizes. As it can be seen in Figure 24a, the crystallites sizes of the layer with the lower PbI_2 content are slightly bigger than the one with more PbI_2. But looking carefully at the quality of crystallization in the case of excess PbI_2, the crystallites are strongly impinged into each other. This is also visible in cross section SEM images (Figure. 24c,d). For the sample with more PbI_2, the cross section SEM image (Figure. 24c) shows a more compact and tight crystallization, while for the lower PbI_2 content, gaps between the different crystallites are visible.
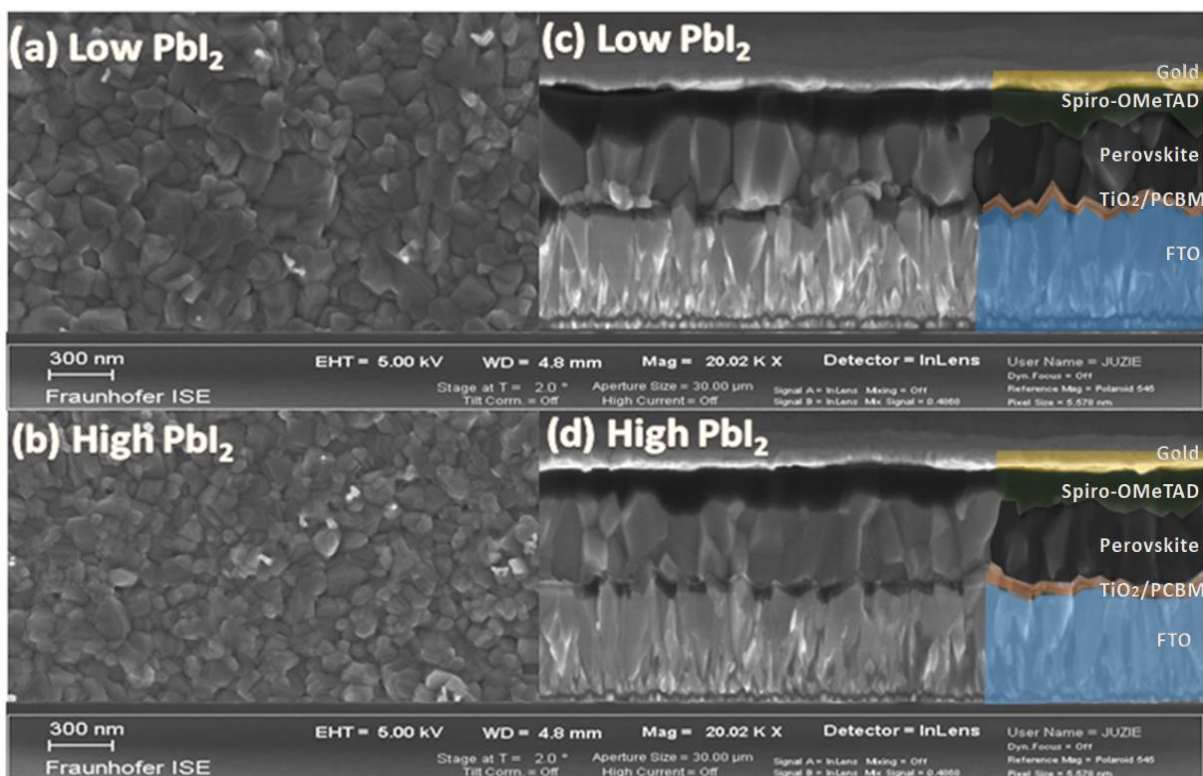

Figure 24. SEM images of the perovskite layers with low PbI_2 content (a) top and (c) cross section views and with high PbI_2 content (b) top and (d) cross section views.

To include a larger variety of PbI_2 concentrations in this study, XRD pattern of perovskite layers formed on a TiO_2 electron transport single layer (Figure. 25a)

and a TiO_2/C60 bilayer (Figure. 25b) was also determined. As it can be seen, the PbI_2 to perovskite peak ratios are different for different substrates. The PbI_2 peak disappeared for the cell with only TiO_2 as electron transport layer. Also for the perovskite made on TiO_2/C60, the PbI_2 peak is very small, in comparison to the TiO_2/PCBM sample. This variation in PbI_2 peak could be due to different perovskite growth on substrates of different roughness.
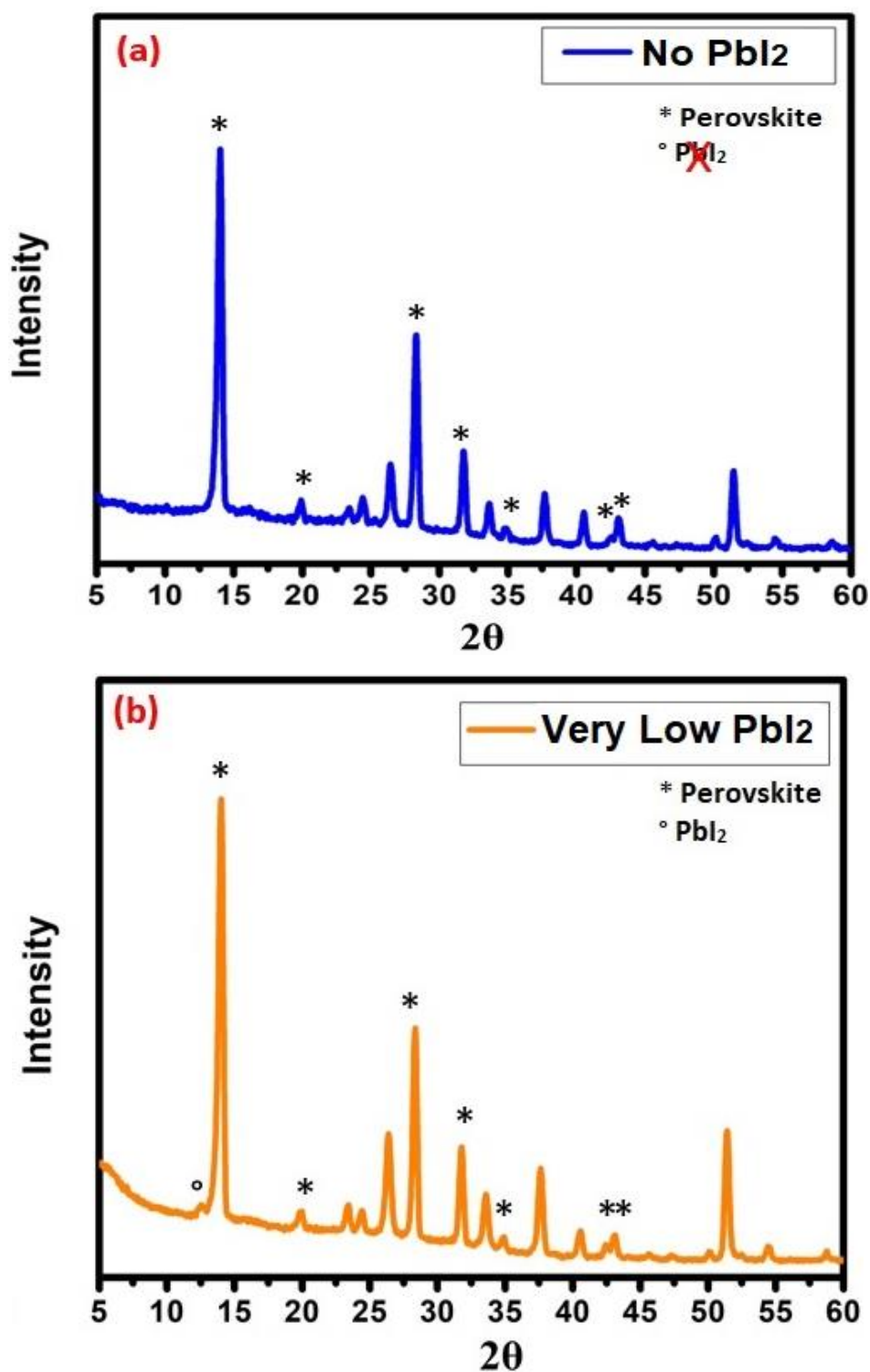
Figure 25. X-ray diffraction patterns of the perovskite layers formed on (a) TiO_2 and (b) $TiO_2/C60$.

TRPL measurements were performed to evaluate the charge extraction quality of the samples with different contents of PbI_2 but a similar $TiO_2/PCBM$ electron

transport bilayer. As can be seen in Figure. 26, the TRPL curve, decays slower in case of higher PbI_2 content. This can be due to the reduction of non-radiative recombination as a result of passivation in the cell with higher PbI_2 content, resulting in the dramatic increase in open-circuit voltage.
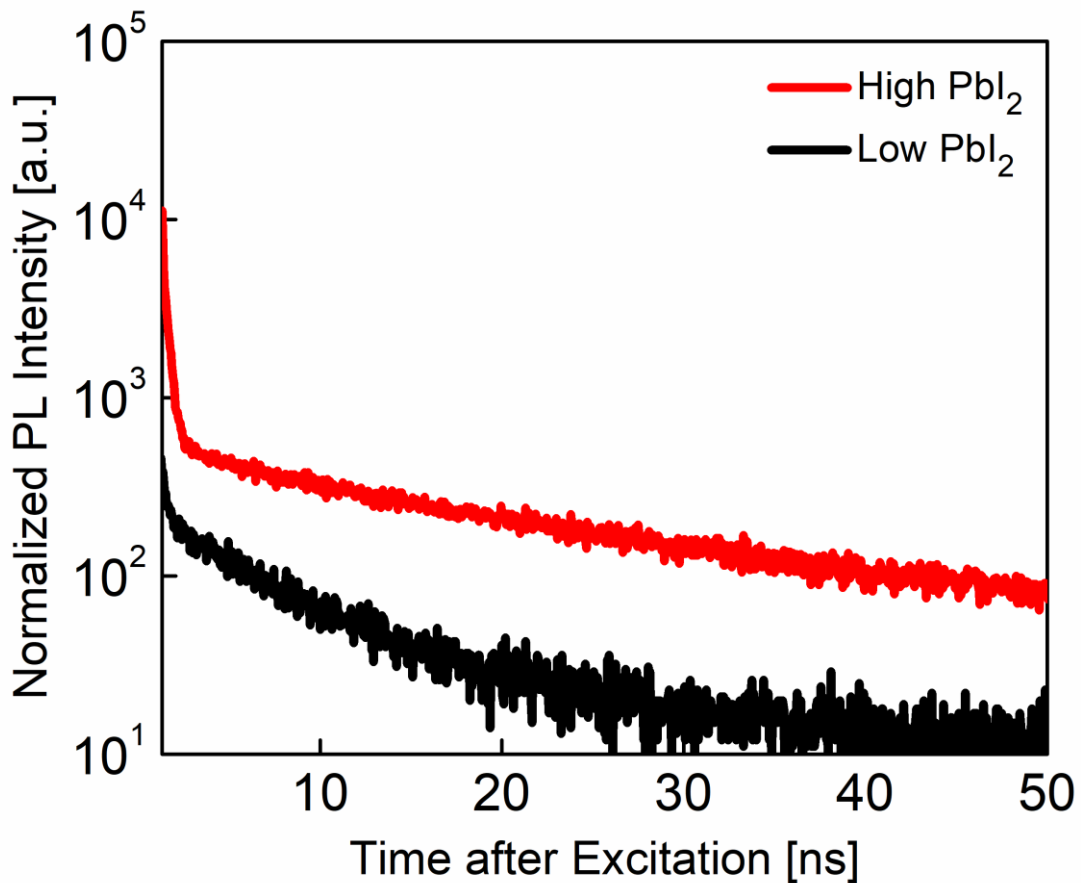

Figure 26. TRPL curves of the perovskite layers prepared on the TiO_2/PCBM electron transport bilayer.

Two sets of solar cells both featuring a TiO_2/PCBM electron transport bilayer but a different PbI_2 content were prepared by decreasing the MAI concentration via

solution filtration. Furthermore, solar cells were prepared using different electron contact configurations, which have shown different PbI_2 concentrations in the XRD spectra. The photovoltaic parameters are listed in Table I. As can be seen, the solar cells with the higher PbI_2 content clearly show a better performance. Comparing the photovoltaic parameters between two sets of cells prepared with the TiO_2/PCBM electron transport bilayer, the difference between Voc and FF is prominent while the Jsc is rather equal with slightly higher values for the solar cell with higher PbI_2. Considering solar cells with different electron contact layers in the comparison, a clear correlation between PbI_2 content and all photovoltaic performance parameters can be seen (Figure 27).

Table I. Photovoltaic performance of the solar cells fabricated with different electron transport layers (ELTs) and PbI_2 contents.

| ETL	TiO_2		TiO_2/C60		TiO_2/PCBM		TiO_2/PCBM	
PbI_2 Content	No PbI_2		Very Low PbI_2		Low PbI_2		High PbI_2	
Scan Direction	Forward	Reverse	Forward	Reverse	Forward	Reverse	Forward	Reverse
Jsc (mA/cm^2)	14.9	16.2	21.8	21.9	22	22.6	22.7	22.95
Voc (mV)	939.4	939.5	1054.5	1054.6	1056.2	1056.4	1090.6	1103.3
FF (%)	46.9	68.3	43.4	54.5	62.9	70.7	69.9	74.5
PCE (%)	6.6	10.4	10	12.6	14.6	16.9	17.3	18.9
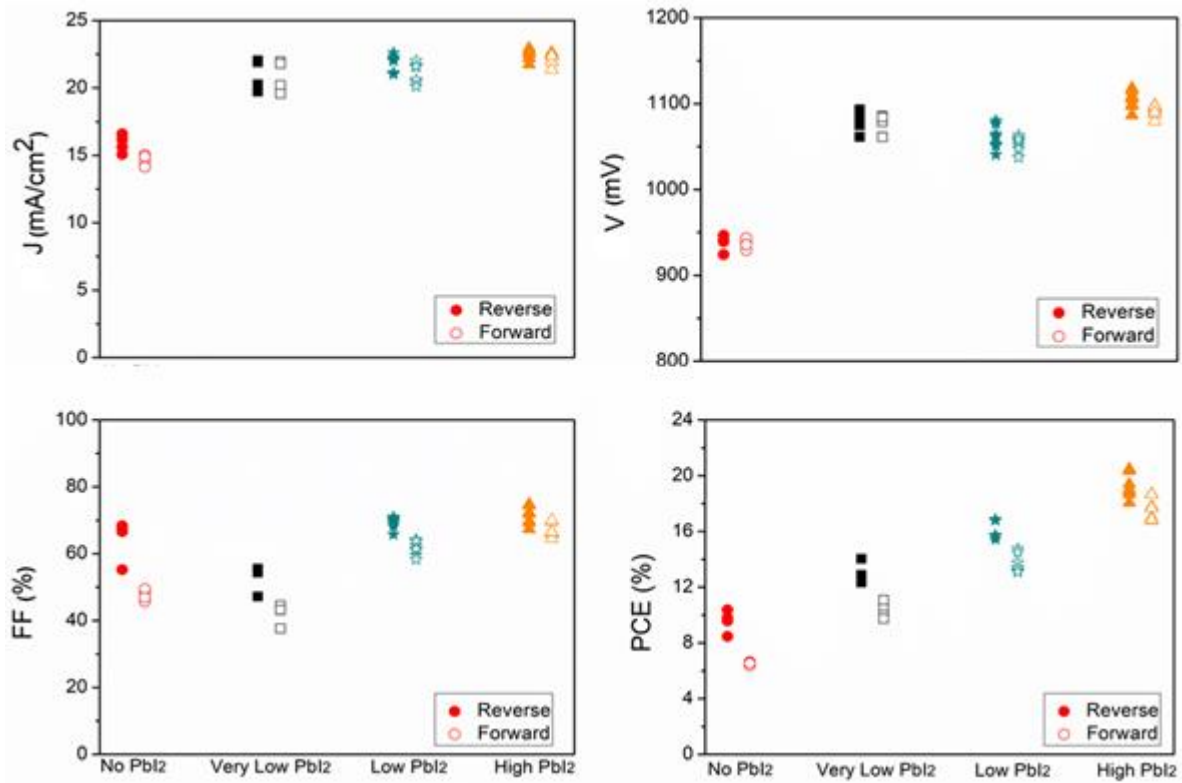
Figure 27. Photovoltaic parameters of the solar cells made with different PbI$_2$ contents.

The J-V characteristics (a,b) and stabilized power conversion efficiencies (c,d) of the champion solar cells featuring a TiO$_2$/PCBM electron transport bilayer are plotted in Figure 28. Additionally to the superior performance of the cell with higher PbI$_2$ content, also the hysteresis mitigated in the solar cell with higher PbI$_2$ content.
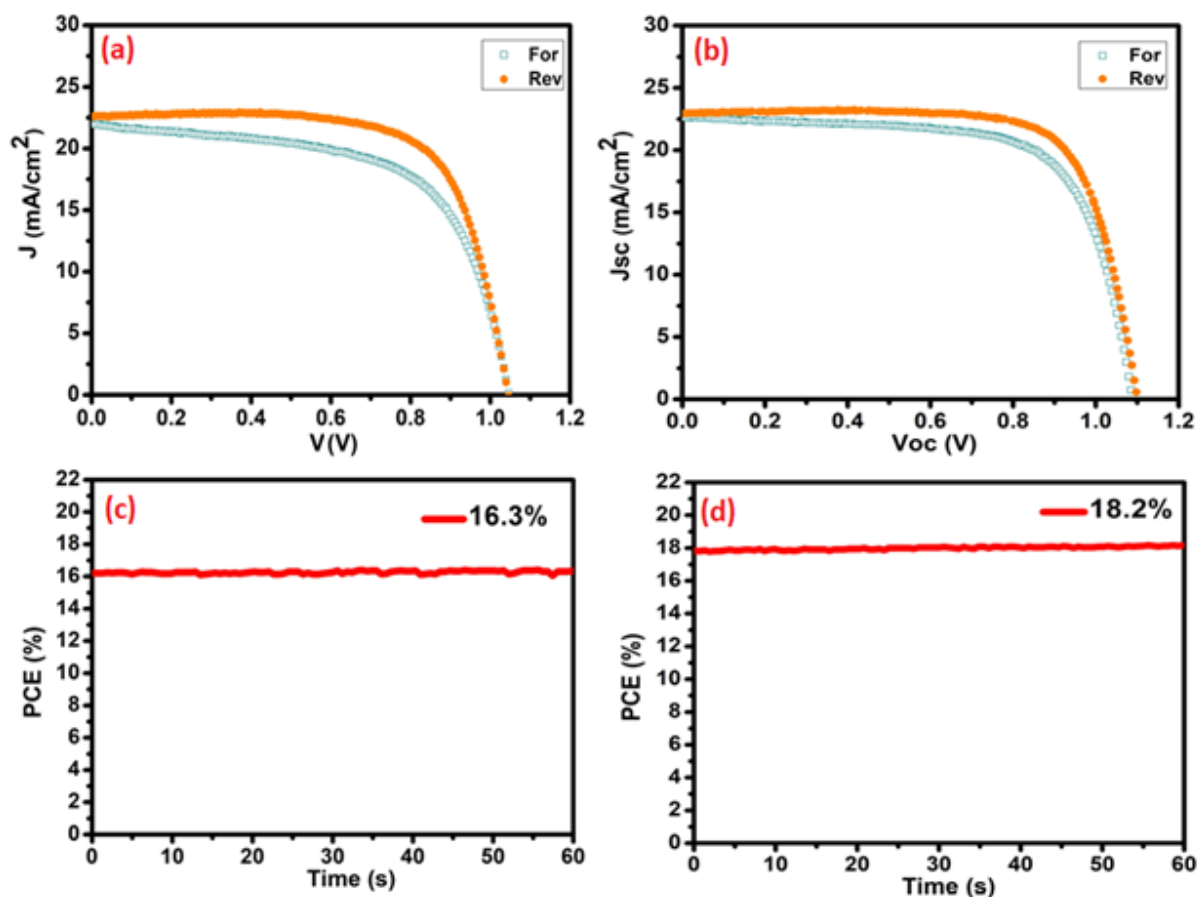
Figure 28. J-V and stabilized PCE curves of the champion solar cells made with low (a,c) and high (b,d) PbI_2 contents.

Better photovoltaic performance is correlated with higher PbI_2 content, smaller but more strongly impinged grains and faster current extraction. All samples have seen differences in processing (filtering/no filtering, different electron contacts), which could cause some of the observed differences. However, the clear trend between PbI_2 content and performance over the whole set of samples suggest that the PbI_2 content is an important parameter for performance. This beneficial role of a slight excess in PbI_2 is also reported for the perovskite solar cells made with solution processing. It is emphasized that a precise stoichiometry is important to

reach the optimum performance. The observations could be convincingly explained by the presence of remnant PbI_2 between the perovskite crystal grains. There, the PbI_2 could act as a surface passivation. Moreover, the unreacted PbI_2 atop ETL, may passivate the ETL/Perovskite interface. Therefore, the higher V_{OC} and the reduced hysteresis would be due to either surface passivation or band edge matching between ETL and perovskite. This band edge matching also facilitates the electron injection which is elucidated by TRPL measurements and is also consistent with the sizeable increase of fill factor shown in Table II. With passivated surfaces, the discontinuity of the crystal at grain boundaries would also be less detrimental. In contrast, it is even possible to profit from improved charge collection close the grain boundaries. Hence, the smaller crystal grains observed for the sample with high PbI_2 content, would even be beneficial.

To achieve even higher efficiencies it is necessary to increase the understanding of crystallization, grains formation and layer ripening. Therefore in this thesis, by a systematic variation of the MAI concentrations, the stoichiometry and thereupon the crystal growth conditions in $MAPbI_3$ perovskite solar cells prepared by a two-step hybrid evaporation-spincoating deposition method, were varied.

The XRD patterns of the perovskite layers formed on a TiO_2/PCBM electron transport bilayer using the MAI solutions with different concentrations are shown in Figure 29. In all samples, perovskite peaks are clearly visible, which are the

indication of perovskite phase formation. Nevertheless, there is also a diffraction peak associated with (001) crystal orientation of PbI_2 at 12.67°. Between the samples, the intensity of the PbI_2 peak is higher in case of 40 mg/ml MAI solution. This means that more PbI_2 is present in the perovskite structure. By increasing the MAI concentrations towards 55 mg/ml, the PbI_2 peak disappeared and the intensity of the perovskite peak increased. This is an indication of more perovskite phase formation and less remnant PbI_2 in the formed perovskite layer.
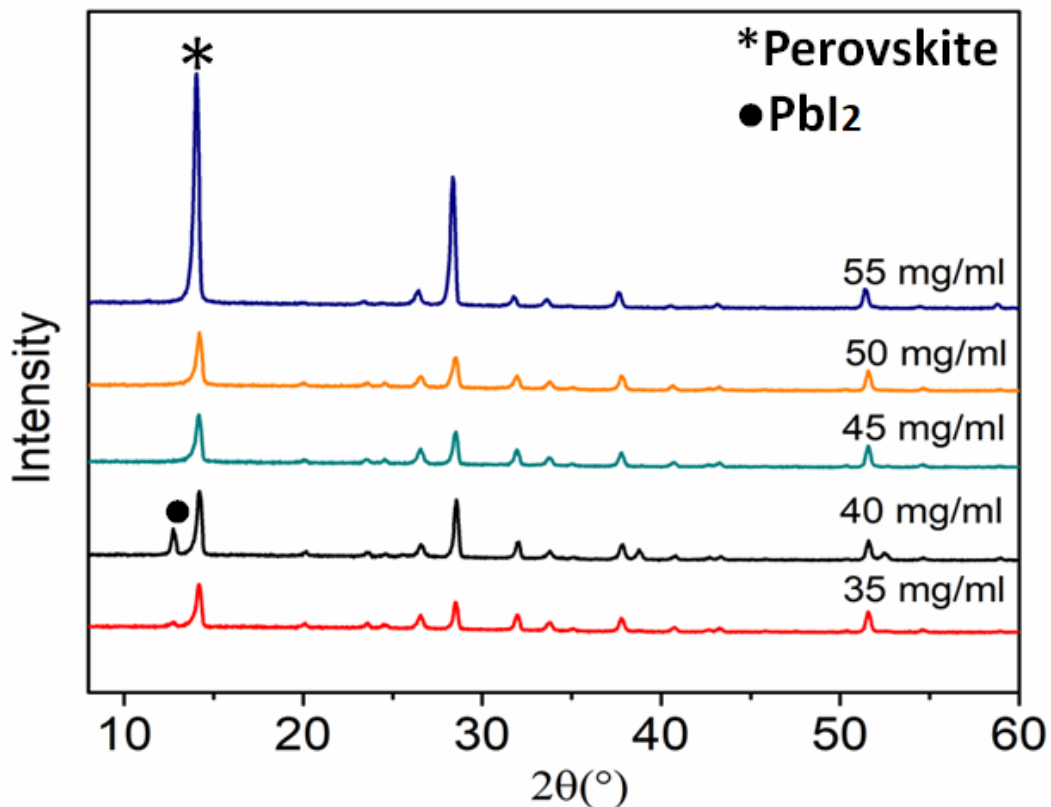

Figure 29. X-ray diffraction patterns of the perovskite layers formed with different MAI concentrations.

The grain sizes of the perovskite layers formed with different MAI concentrations were calculated using the Scherrer equation by taking the full width at half-

maximum (fwhm) of the dominant lattice reflection of 2Θ at 14.02°. The results are shown in Table II. The error bars of estimated perovskite grain sizes are also provided in Figure 30.

Table II. Estimated perovskite grain size using Scherrer equation by taking the full-width-at-half-maximum (FWHM) of the dominant lattice reflection of 2θ at 14.02°.

| MAI Concentration (mg/ml)	Grain Size (nm)
55	236
50	212
45	208
40	206
35	202
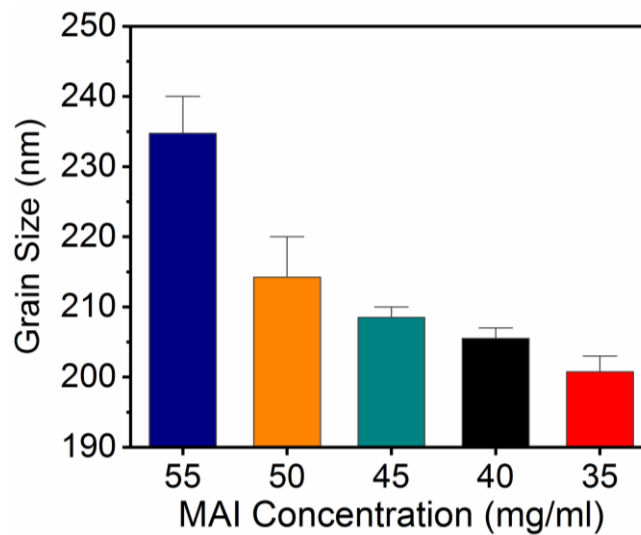
Figure 30. Error bars of estimated perovskite grain size using Scherrer equation by taking the full-width-at-half-maximum (FWHM) of the dominant lattice reflection of 2θ at 14.02°.

Differences between the samples are also visible in the SEM images (Figure 31). The pristine PbI_2 layer is porous, this facilitates the efficient MAI intercalation and perovskite phase formation. In all MAI concentrations highly crystallized perovskite layers were formed, but with clear differences in nucleation quality and crystallites sizes. As can be seen in Figure 31, the crystallites sizes of the layers of the higher (50-55 mg/ml) MAI concentrations are slightly bigger than those with lower (35-45 mg/ml) concentrations. Comparing the quality of crystallization in case of 40 mg/ml MAI concentration, which contain excess PbI_2 with 50-55 mg/ml, the crystal grains are more strongly impinged into each other. In case of 35 mg/ml, the lowest MAI concentration in this study, the compactness of the formed perovskite layer is less than the other concentrations. It seems that 40 mg/ml was a threshold for the MAI concentration, less than that the perovskite phase formation was not complete and a lot of voids appeared in the formed layer.
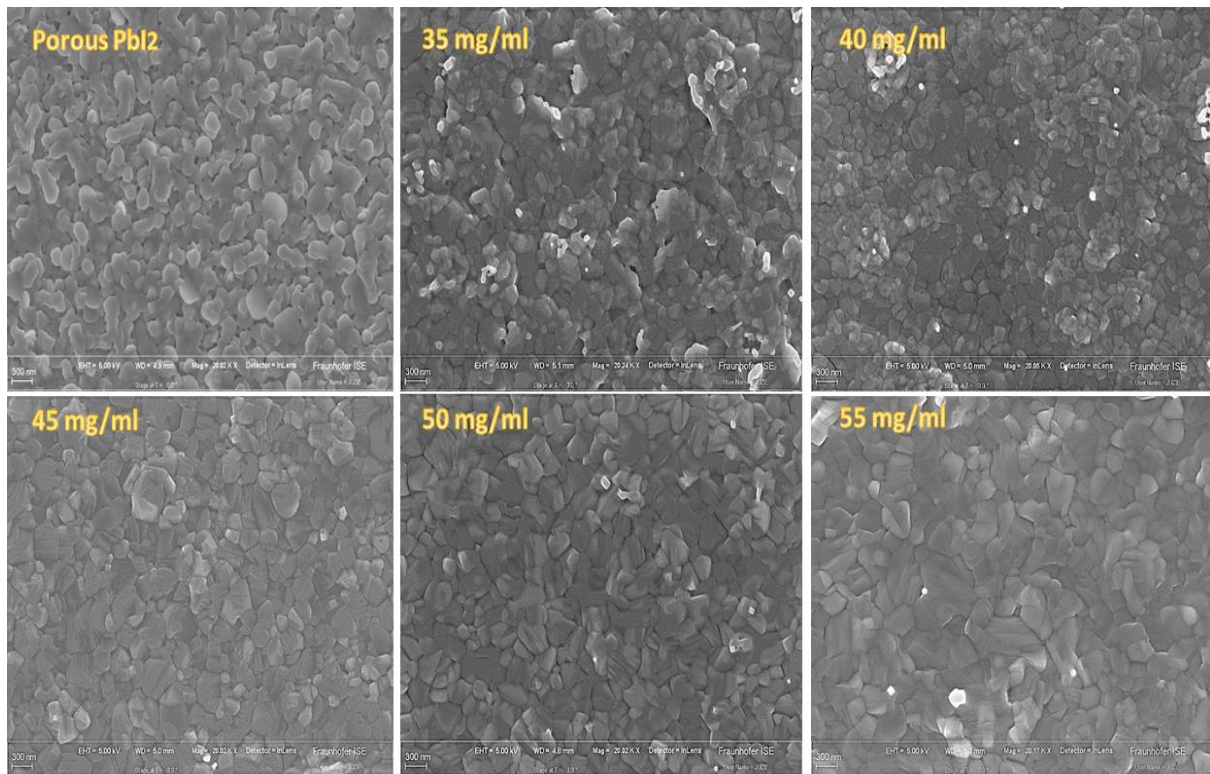
Figure 31. SEM images of the porous PbI$_2$ and the perovskite layers formed with different MAI concentrations.

The variations in grains growth conditions are also shown with AFM images in Figure 32. For the sample of lower MAI concentration (40 mg/ml) with remnant PbI$_2$, smaller and more impinged perovskite grains were formed while in case of the highest MAI concentration (55 mg/ml) with full perovskite phase formation and no remnant PbI$_2$, big grains with deep valleys between them and a highly rough surface were formed. This is in a good agreement with SEM images in Figure 31.
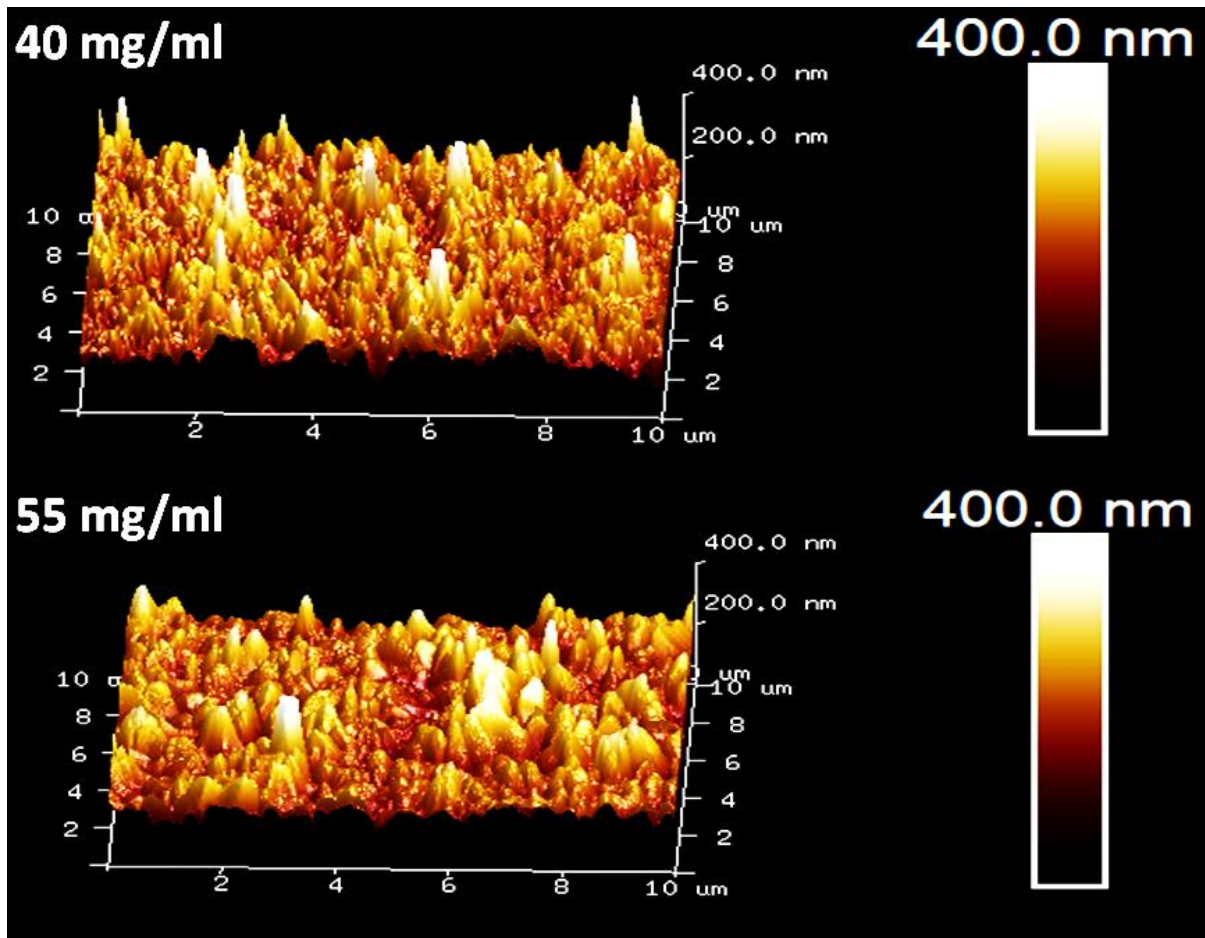
Figure 32. AFM images of the perovskite layers formed with 40 mg/ml and 55 mg/ml MAI concentrations.

Cross-section SEM images are depicted in Figure 33. As can be seen, in case of MAI concentrations of 40-45 mg/ml the formed perovskite layers are highly compact and the grains are strongly impinged but in very low 35 mg/ml or very high 50-55 mg/ml concentrations many gaps appeared between the grains. These gaps could act as the defect centers, which decreases the power conversion efficiency of a solar cell. Different sizes of the crystallites are also visible in cross-section SEM images (Figure 31). The grains formed with higher (50-55 mg/ml) MAI concentrations are bigger but less impinged while in case of 40-45 mg/ml

the crystal grains are smaller and compact. Therefore a very good agreement between all microscopic results in explanation of the grain growth conditions under variable stoichiometries can be seen.
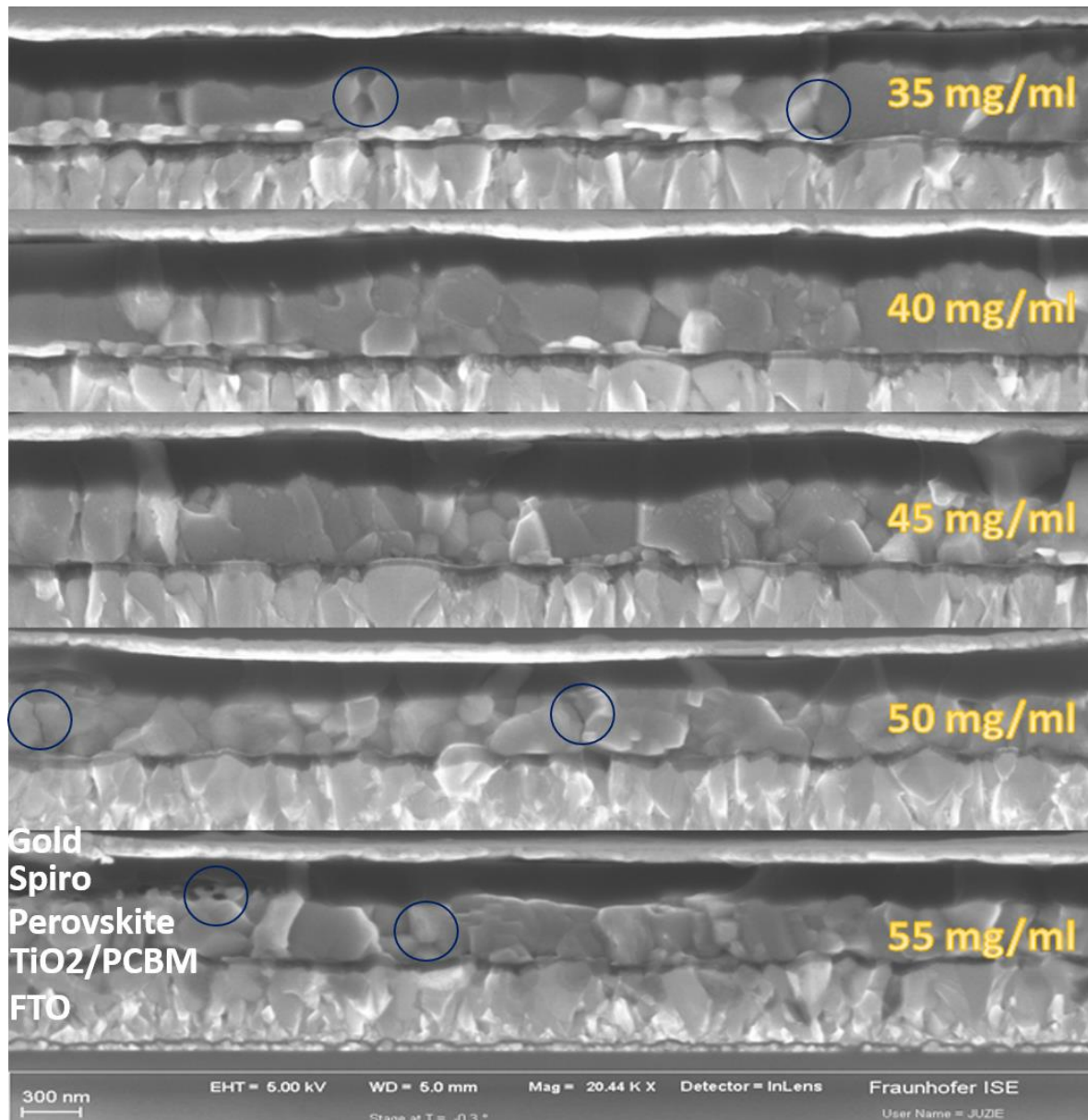

Figure 33. Cross-section SEM images of the perovskite layers formed with different MAI concentrations. Gaps and cracks are shown with circles.

The absorption spectra of the perovskite layers formed with different stoichiometries are shown in Figure 34. As can be seen, the perovskite layers of 40-45 mg/ml MAI concentrations yield higher absoption than the low 35 mg/ml and high 50 mg/ml concentrations. The difference in absorption by stoichiometry variation could be attributed to the variable grains growth conditions explained by microscopic measurements. In case of 40-45 mg/ml, the formed perovskite layers were compact and uniform while in very low or very high MAI concentrations the voids appeared between grains and decreased the compactness and uniformity of the deposited layer. Accordingly the more compact and uniform perovskite layer formed and the higher absorption achieved.
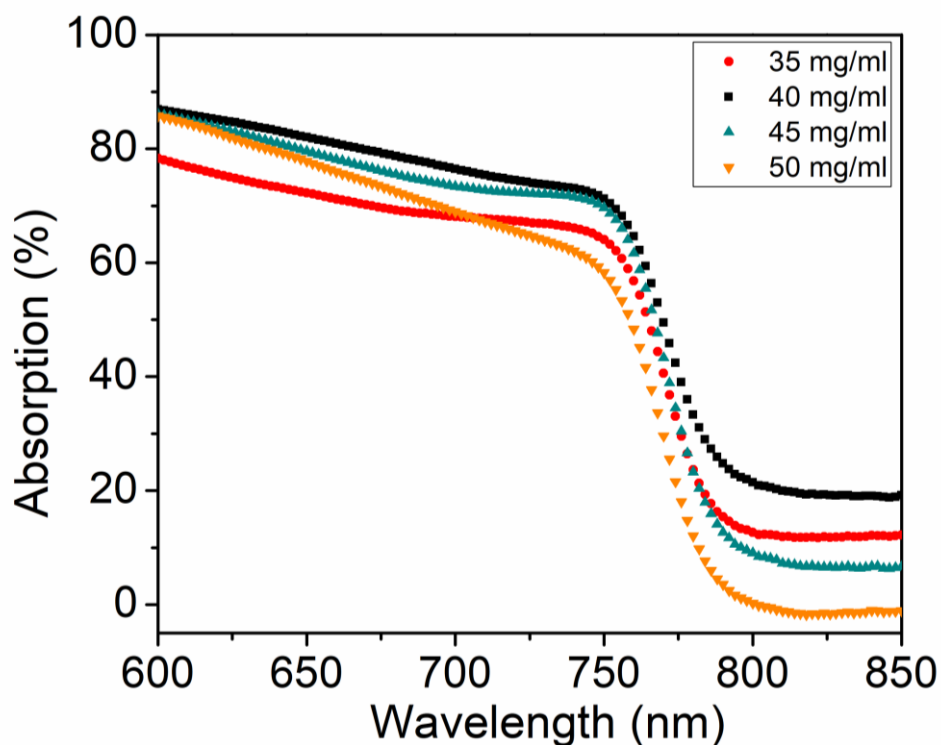

Figure 34. UV-vis absorption spectra of the perovskite layers formed with different MAI concentrations.

The photovoltaic parameters are shown in Figure 35. As can be seen, the Jsc and Voc values are higher for the samples prepared with lower MAI concentrations or higher PbI_2 contents. This could be attributed to passivation role of excess PbI_2 both at perovskite-ETL interface and grain boundaries. In case of 35 mg/ml the intercalation of MAI in PbI_2 was not efficient and the perovskite phase formation was not complete. The FF of the solar cells made with this stoichiometry is lower than 40-45 mg/ml due to the remnant and intact PbI_2 layer at the perovskite-ETL interface. By increasing the MAI concentrations to 50-55 mg/ml the Jsc and Voc values decrease while the FF is still high. Accordingly the 40-45 mg/ml MAI concentrations are found as the optimized stoichiometries where the solar cells gain benefit from the passivation role of excess PbI_2 both at grain boundaries and interfaces and thereupon not suffering from charge transport problems at the interfaces. This indicates that by decreasing the PbI_2 contents or increasing the MAI concentrations, passivation of grains and grain boundaries diminish while the perovskite-ETL interfaces are still transporting well.
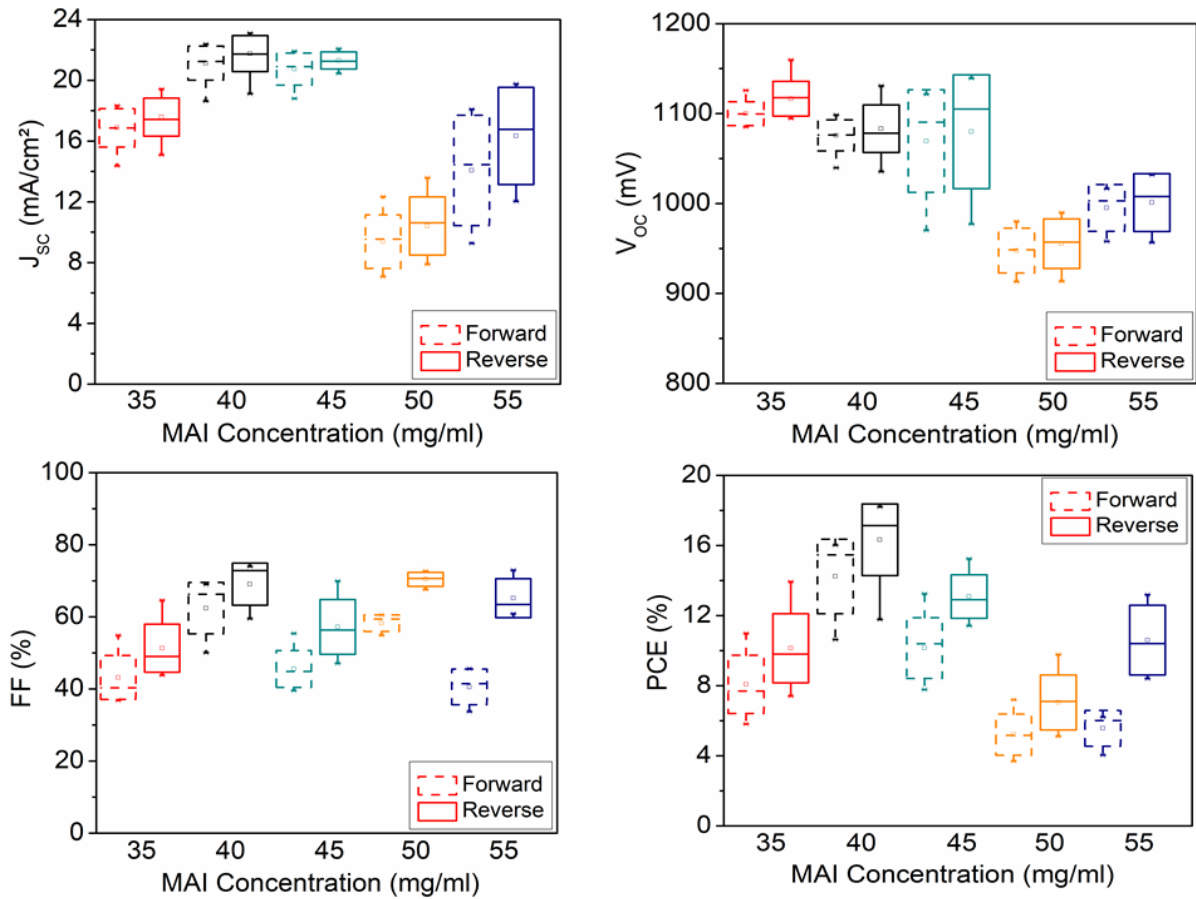
Figure 35. Photovoltaic parameters of the perovskite solar cells made with different MAI concentrations.

The photovoltaic parameters are also listed in Table III. Hysteresis is known as a challenge for perovskite photovoltaics.[36-40] Therefore in this study the role of grain growth conditions by stoichiometry variation and their impact on hysteresis level was investigated. As we already know from the literature, the ionic movements within the perovskite lattice and the interfaces at perovskite-charge transport layers play the most important roles in the origin of hysteresis.[36-40] Here in this study, by variation of stoichiometry the PbI_2 contents in the solar cells were varied, which elucidated direct impact on grain growth conditions, interfaces and

thereupon hysteresis level. As can be seen in table III, the hysteresis level is lower for lower MAI concentrations of 35-45 mg/ml. This is due to the passivation role of remnant PbI_2. However, the sample with 35 mg/ml suffered from interface problems and the positive role of excess PbI_2 tends to be negative. The 40-45 mg/ml yielded the lowest hysteresis levels. This is due to both grain boundaries and interface passivation. Moving towards higher MAI concentrations of 50-55 mg/ml, the Jsc and Voc values dramatically dropped, which is an indication of diminished grain boundaries passivation by excess PbI_2. Accordingly, the origins of hysteresis could be addressed by manipulation of the grain growth conditions and the hysteresis could be mitigated as an important challenge in perovskite photovoltaics.

Table III. Photovoltaic parameters of the perovskite solar cells made with different MAI concentrations. 10-15 solar cells are made and analyzed for each MAI concentration.

MAI (mg/ml)	35		40		45		50		55	
Scan Direction	Forward	Reverse	Forward	Reverse	Forward	Reverse	Forward	Reverse	Forward	Reverse
Jsc (mA/cm²)	18.4	19.5	22.7	22.95	21.9	22	12.4	13.6	14.5	16.5
Voc (mV)	1092.2	1111.4	1090.6	1103.3	1091.5	1100.6	980.1	990	997.4	1000.6
FF (%)	54.9	64.6	69.9	74.5	55.4	62.75	59.6	72.7	41.75	60.9
PCE (%)	11	14	17.3	18.9	13.25	15.2	7.25	9.8	6.1	10
Hysteresis (%)	21.4		8.4		12.8		26		39	

The J-V characteristics (a) and stabilized power conversion efficiencies (b) of the champion solar cells featuring different MAI concentrations are plotted in Figure 36. Additionally to the superior performance, the hysteresis mitigated in the solar

cells with lower MAI concentrations of 35-45 mg/ml. Finally the highest stabilized efficiency of 18.2% with the lowest hysteresis has achieved from the solar cell made with 40 mg/ml MAI concentration.
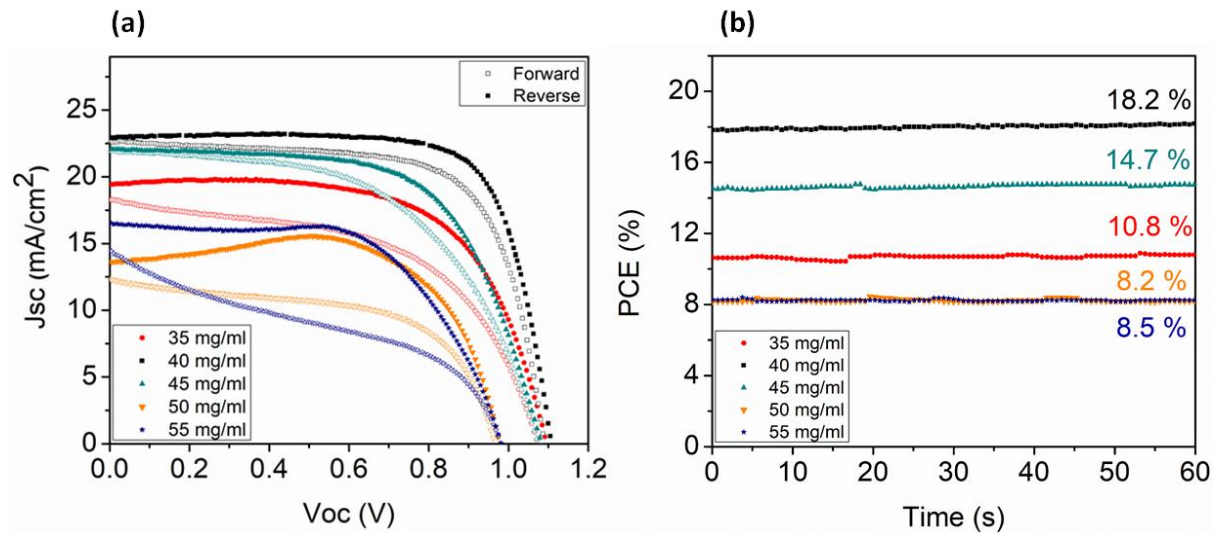

Figure 36. (a) J-V curves measured with scan rate of 43 mV/s and (b) stabilized PCE of the champion solar cells of different MAI concentrations.

TRPL measurements were done to evaluate the charge extraction quality of the samples with different stoichiometries but a similar TiO_2/PCBM electron transport bilayer. To increase the accuracy of the PL measurements, three measurements on different locations over each sample (Figure 37a) were performed. A bi-exponential decay model was used to fit the PL decay data and extract the life time values (Figure 37b). As can be seen in Figure 37a, the curves represent more or less the same trend for each stoichiometry. To explain the variable PL curve decay in different stoichiometries, it is important to note that these measurements were performed on the half-cell level where the perovskite

layers were deposited atop ETL and there were no hole transport layers and metal contacts deposited to collect the carriers before being recombined. This is important because the low life-time values derived from fitting calculations should not be considered as an indication for the weak performance of the full solar cell. For instance, the microscopic and optical properties of the perovskite layers formed with MAI concentrations of 40-45 mg/ml promised a higher performance than the other stoichiometries. However the fitted life-time values for 40-45 mg/ml concentrations were the lowest, which seems to be a contradiction. Indeed, evaluating the performance of the full solar cell based on the half-cell measurements will not deliver an accurate anticipation of the full cell performance. These kind of measurements could be useful to evaluate the stoichiometry-dependant passivation at perovskite-ETL interface or crystal grains levels. As an example, the lowest life-time calculated is for the 40 mg/ml MAI concentration but on the other hand this stoichiometry represents the highest efficiency (Figure 35). The key point here is the high quality of the perovskite-ETL interface due to the passivation by excess PbI_2, which facilitates the electron injection. Therefore the highest Jsc and FF are measured for this stoichiometry on the full-cell level while in the half-cell life-time measurements as collecting the dissociated charge carriers is impossible and due to the high quality of the interface, they reinject and recombine very fast. That is why the lowest life-time calculated from the data fitting does not necessarily correspond to the lowest Voc in full-cell level. By increasing the MAI concentrations towards 50-55 mg/ml the

passivation role of excess PbI_2 diminishes. Here however the half-cell life-time values increase but in the full-cell performance the Voc and Jsc values dramatically decrease and this is again due to the positive role of passivation at interface and grain boundaries by excess PbI_2, which is diminished by increasing the MAI concentrations. In case of 35 mg/ml the highest life-time value is calculated in the half-cell level but looking at the photovoltaics parameters of the solar cells made with this stoichiometry it could be understandable that the thick PbI_2 remaining at the perovskite-ETL, passivates the interface so that in a half-cell level the recombination process is delayed therefore high life-time value is achieved but in a full-cell level the FF is suffered from this thick barrier of PbI_2 layer, therefore the final efficiency decrease. Accordingly, to have a reliable anticipation of the cell performance it is tricky to only evaluate the life-time values achieved from half-cell TRPL measurements.
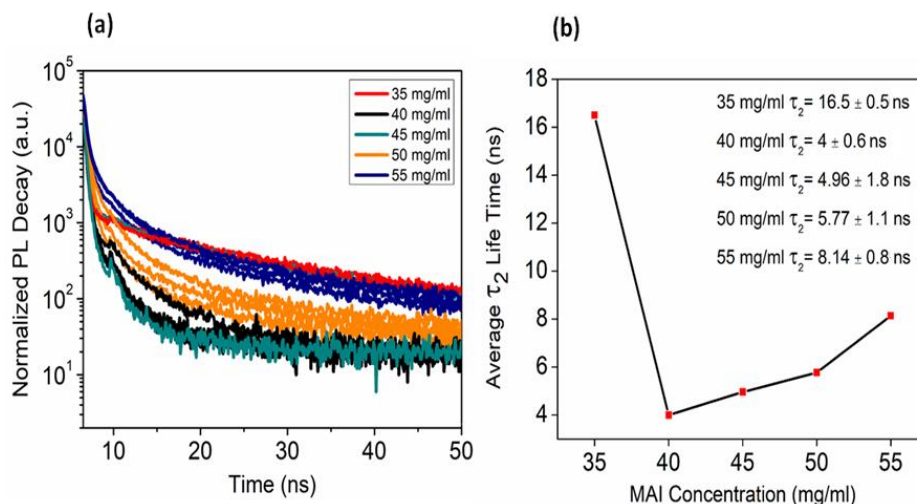

Figure 37. TRPL decay curves of the perovskite layers formed with different MAI concentrations (9a) and corresponding life time values (9b).

Steady-state PL intensity measurements were done on two different locations over each sample to achieve reliable understanding from the PL properties of each stoichiometry. As can be seen in Figure 38, the two PL intensities for each stoichiometry represent the same trend. In comparison with TRPL measurements the results are in good agreement. The differences in PL intensities could be correlated to the crystallization and grains growth conditions in different MAI concentrations. For the MAI concentrations of 40-45 mg/ml as confirmed by microscopic analysis, the grains are tightly connected to each other leaving no pinholes as defect centers. This is due to positive contribution of excess PbI_2 for passivation of the grains and perovskite-ETL interface. The PL intensity peaks of the PbI_2-rich samples or 35-45 mg/ml MAI concentrations are slightly red-shifted suggesting less defects. The highest PL quenching is measured for the MAI concentrations of 40-45 mg/ml, which is consistent with their Jsc values. By increasing the MAI concentrations to 50-55 mg/ml or decreasing the passivation role of excess PbI_2, the PL quenching efficiency decrease, which is also consistent with low Jsc values of these concentrations. As confirmed with TRPL and photovoltaic performances, here also the sample with the lowest MAI concentration (35 mg/ml) is strongly suffering from thick intact PbI_2 layer at perovskite-ETL interface, therefore the lowest quenching efficiency is measured for this stoichiometry.
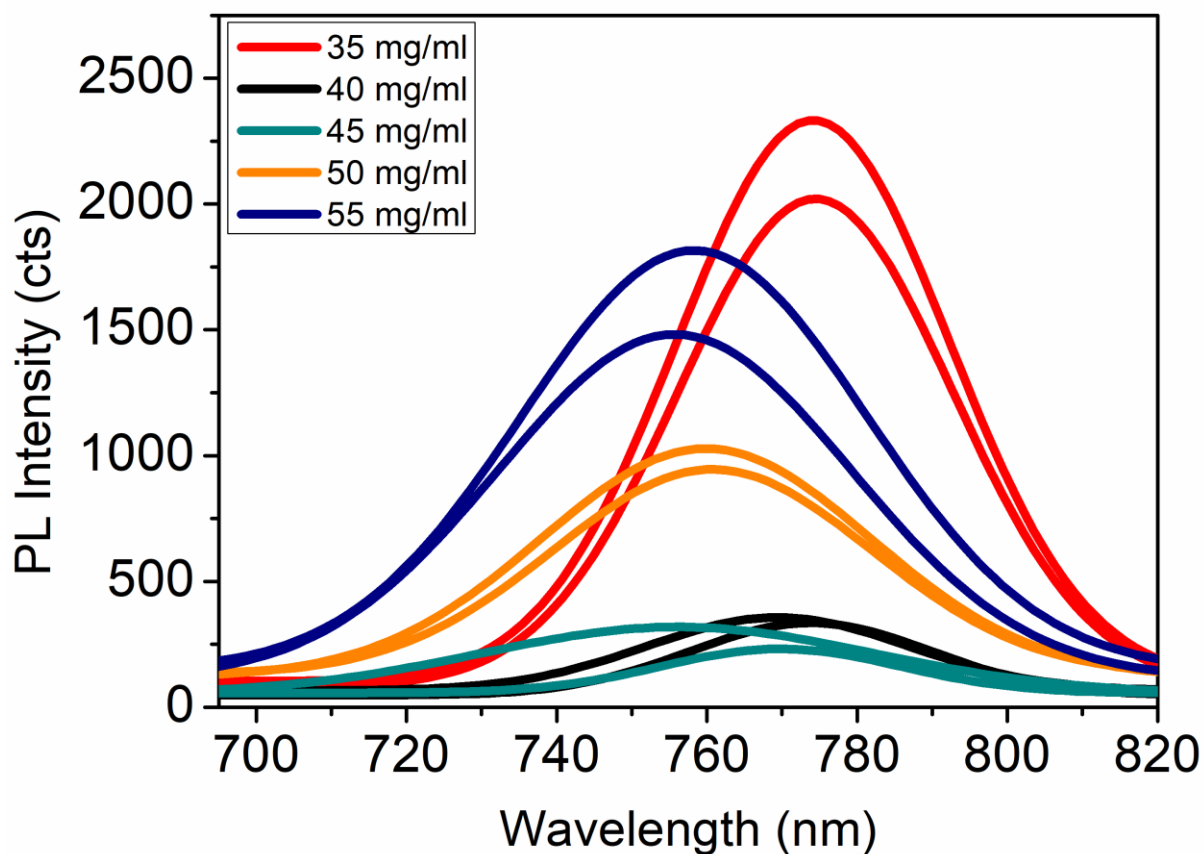
Figure 38. Steady-state PL curves of the perovskite layers formed with different MAI concentrations.

To present a rational explanation for the positive role of access PbI_2 observed in the samples with PCBM layer, kelvin probe force microscopy (KPFM) measurements on the samples with different crystallization conditions were performed. KPFM has been used as a tool to measure the contact potential difference (CPD) and the surface photovoltage (SPV).[48] Under illumination, the excited electrons and holes build an open-circuit potential across the film, which desociates the positive and negative ions. This could decrease the recombination and improve the charge carrier injection into the electron transport layer. At an 8

V bias voltage the mean potential values for the samples with different PbI$_2$ incorporation were measured (Figure 40). First the surface topography was mapped and then the KPFM measurements were done in dark and under illumination and finally the mean potentials were measured. As it can be seen, different PbI$_2$ contents yield different mean potentials. The highest mean potential corresponds to the highest efficiency and lowest hysteresis. This highlights the important role of passivation where the excess PbI$_2$ could passivate both the perovskite-ETL interface and crystal grains. This could eventually decrease the charge carrier recombination and improve the hysteresis in perovskite solar cells.
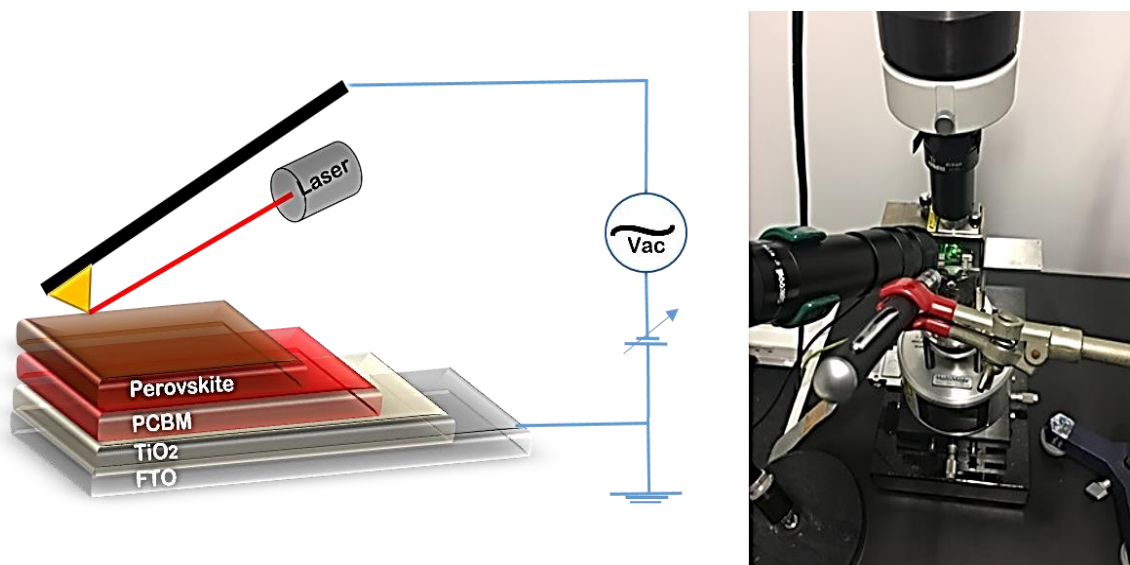

**Figure 39.** KPFM measurements setup.
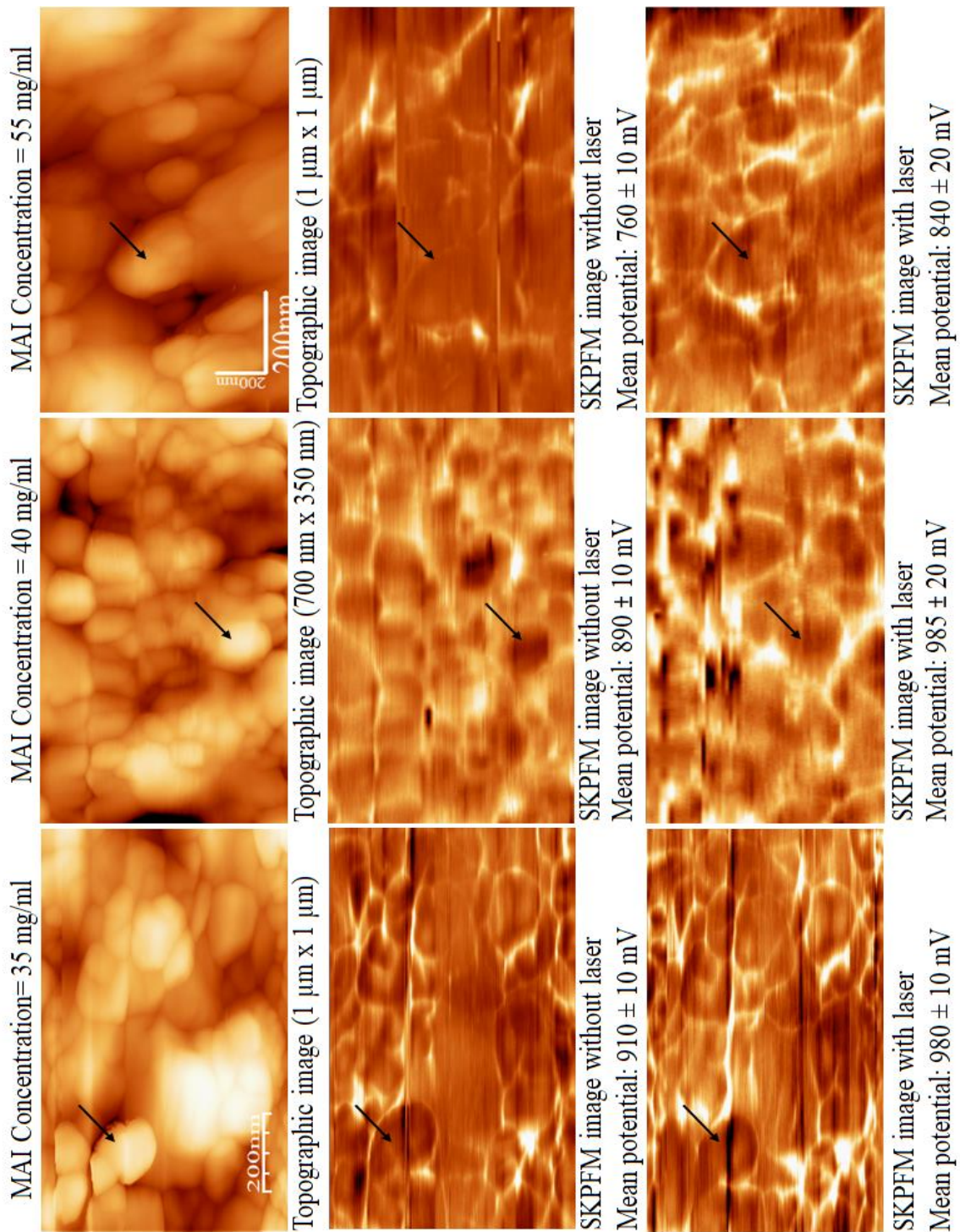
Figure 40. KPFM measurements of samples deposited with different MAI concentrations. For the well passivated sample of 40 mg/ml MAI concentration the mean potential is higher.

3.3 Interface engineering in two-step hybrid method, ITO vs FTO

FTO coated glasses are electrically conductive and ideal for use in a wide range of devices, including applications such as optoelectronics, thin film photovoltaics, energy-saving windows and other electro-optical and insulating applications. FTO has been recognized as a very promising material because it is relatively stable under atmospheric conditions, chemically inert, mechanically hard, high-temperature resistant, has a high tolerance to physical abrasion. Indium tin oxide (ITO) is widely used as a transparent conducting oxide. Its major characteristics are electrical conductivity, optical transparency and the ease to be deposited as a film. ITO and FTO are transparent conductive oxides which are frequently used as cathode contacts. ITO provided a flat substrate while FTO a rough one to grow the perovskite on top. The structural, optical and electrical properties of the perovskite layers formed atop ITO and FTO transparent conductive oxides were studied in this thesis.

The XRD graphs are shown in Figure 41. As can be seen, the PbI_2 peak is intensive in case of ITO. This can be attributed to the excess PbI_2 in perovskite structure due to the incomplete perovskite crystals growth. This incomplete perovskite crystal growth can be correlated to a better surface wettability offered by rough FTO where the MAI solution during the second step of hybrid deposition intercalated more effectively.
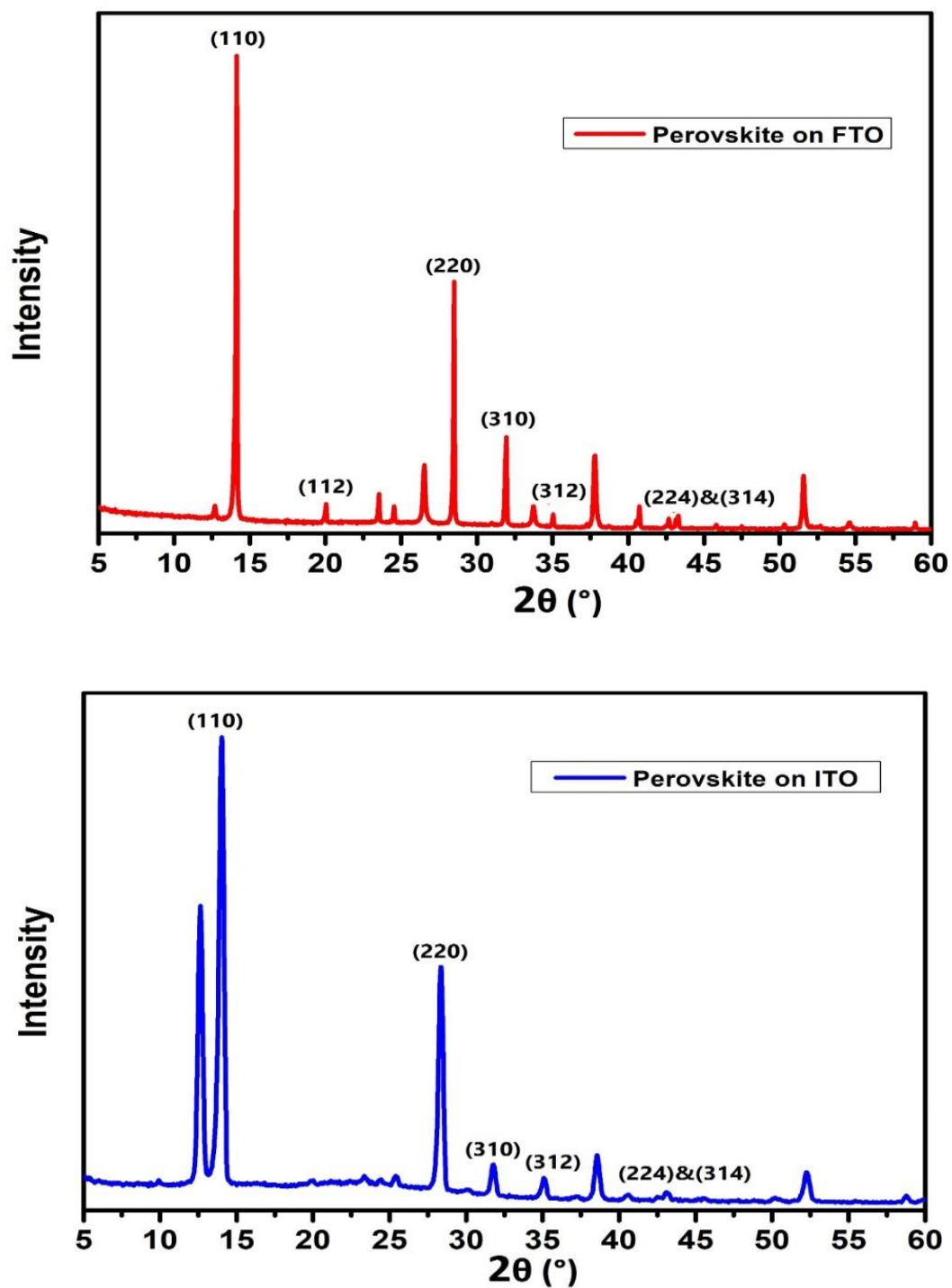
Figure 41. XRD patterns of the perovskite layers deposited atop FTO and ITO coated glass substrates and in presence of TiO_2/PCBM as ETL.

The cross section SEM images of the perovskite layers formed atop ITO and FTO coated glass substrates are illustrated in Figure 42. As can be seen, the ITO provides a flat substrate and FTO a rough one. The perovskite crystal grains

formed in case of FTO are more impinged than ITO. This is beneficial due to providing a pinhole free layer and mitigation of shunt passes from HTL to ETL through perovskite absorber.
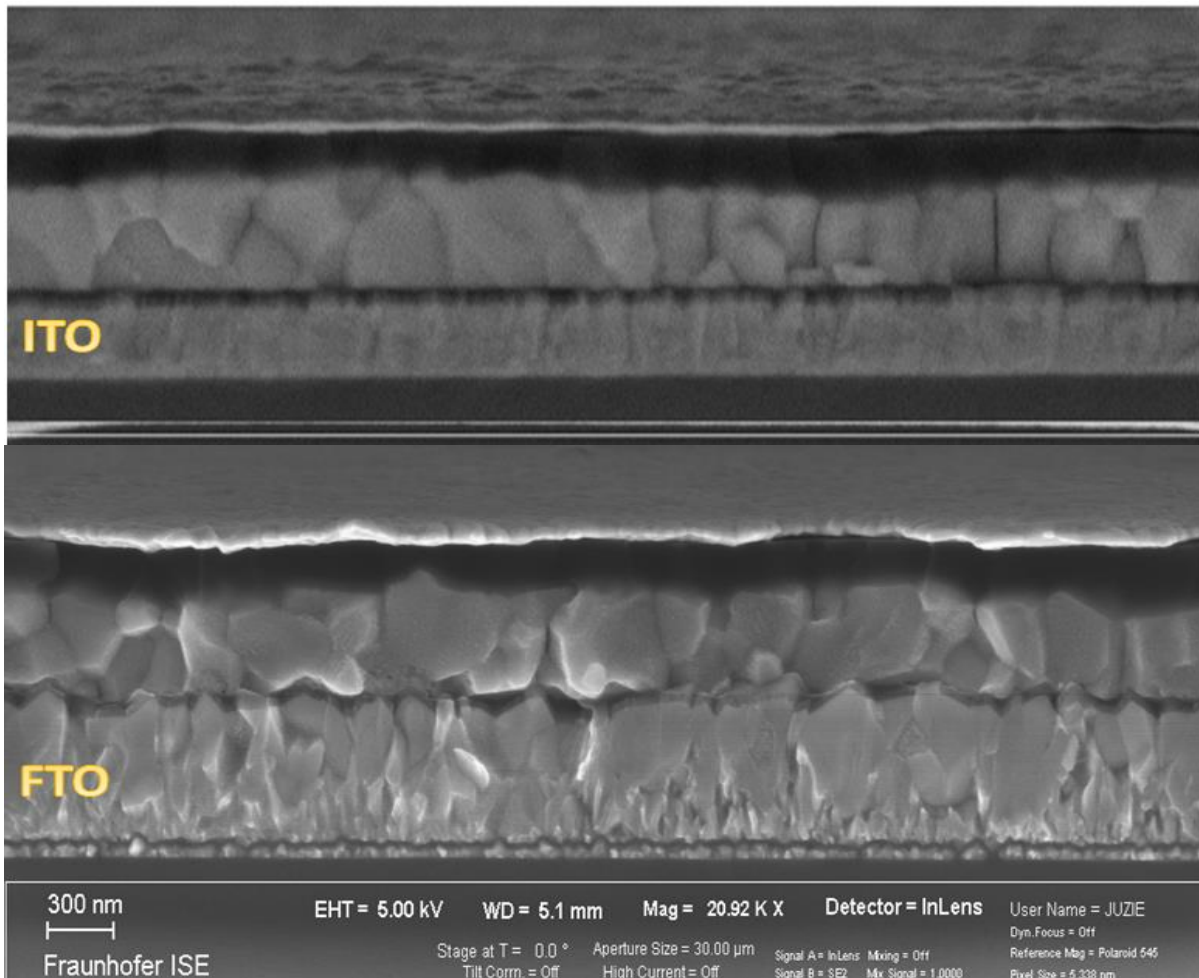

Figure 42. Cross-section SEM images of the perovskite layers deposited atop FTO/TiO$_2$/PCBM and ITO/TiO$_2$/PCBM coated glass substrates.

Optical spectroscopy measurements have been done to analyze the optical properties of the perovskite layers formed on ITO and FTO coated substrates. A 100 nm MgF$_2$ antireflection coating (ARC) was deposited on the glass side to

decrease reflection losses. The reflection and transmission of the solar cells were measured with a spectrophotometer and the absorption was calculated based on the following formula: A = 1- (R + T)

The optical properties of the solar cells fabricated with ITO coated glass with and without ARC are depicted in Figure 43.
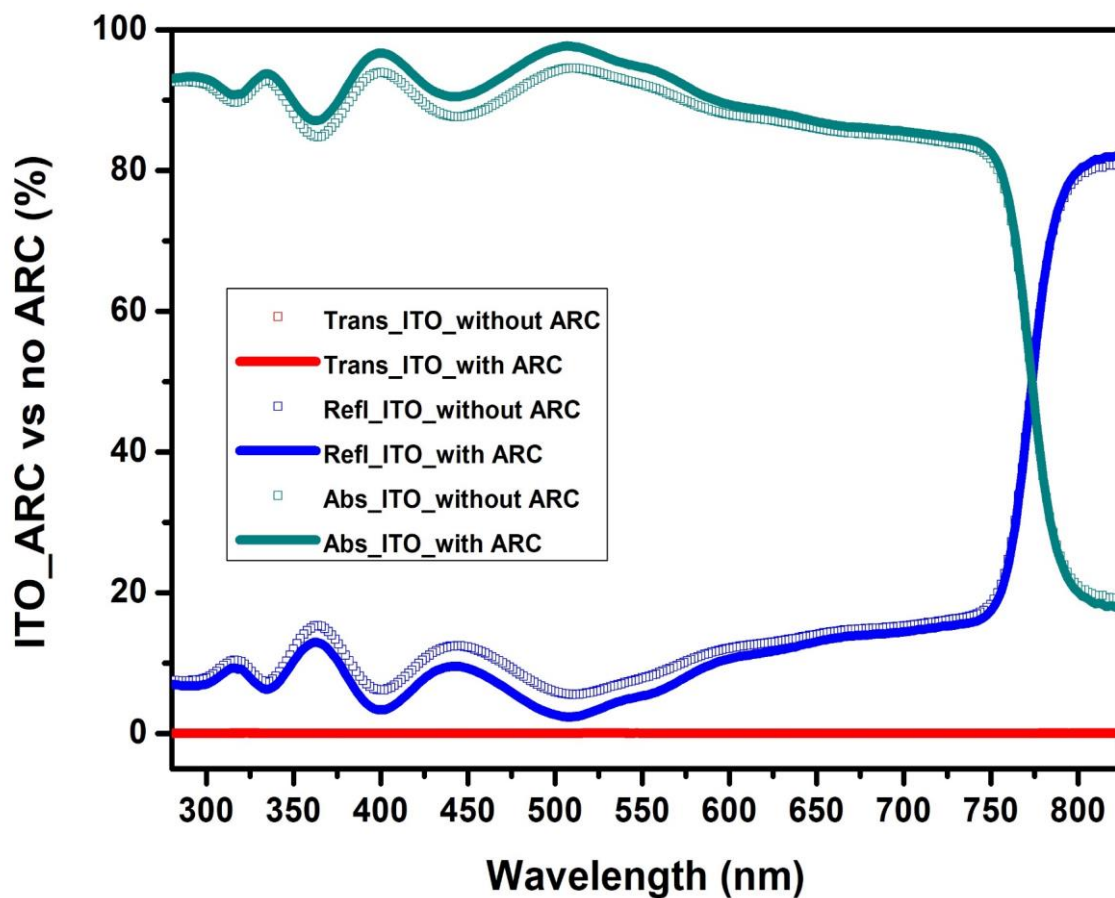

Figure 43. Optical properties of the perovskite layers deposited atop ITO coated glass substrates with and without ARC layer.

The 0% transmission measured is due to the gold contacts deposition and the fact that gold is a 100% reflector. As can be seen in Figure 43, deposition of a 100 nm MgF_2 enhanced the light absorption.

The same measurements were performed for the solar cells fabricated atop FTO coated glass substrates. As can be seen in Figure 44, similar to ITO, the presence of MgF_2 enhanced the light absorption in perovskite absorber.
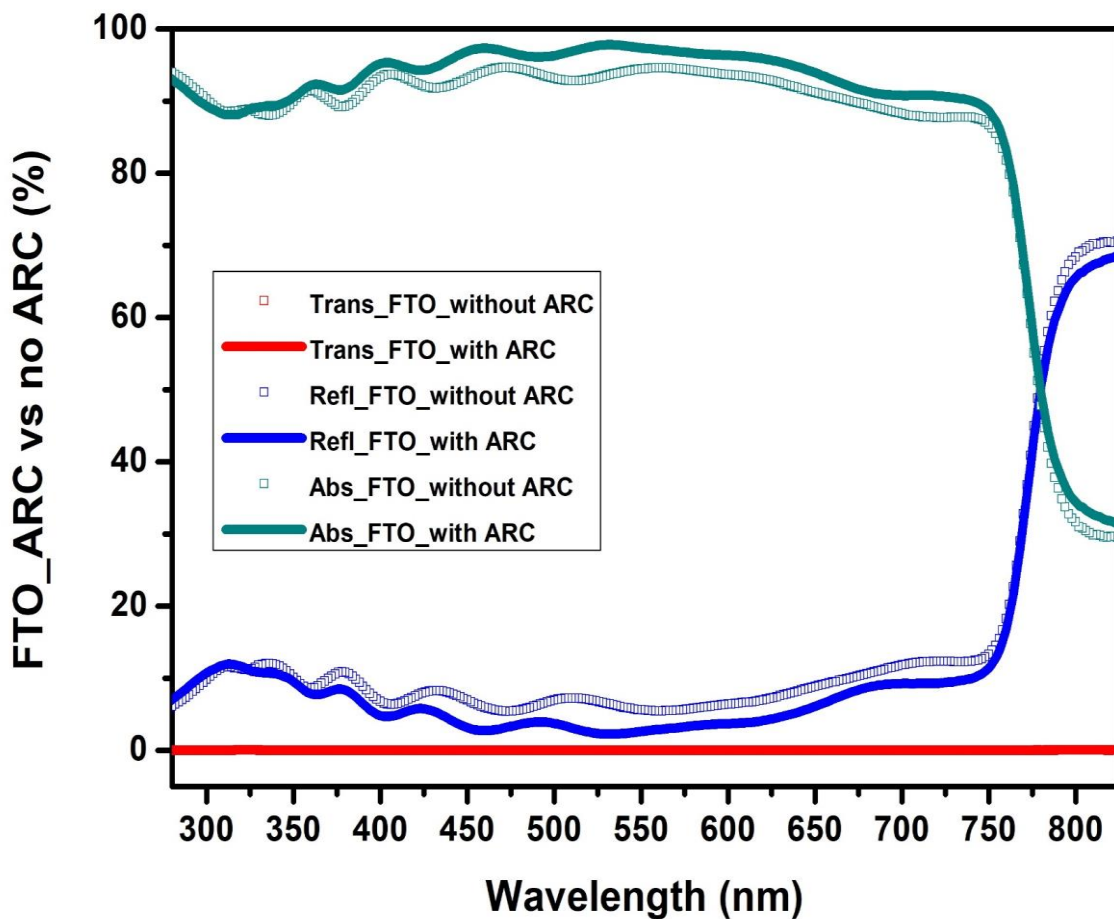
Figure 44. Optical properties of the perovskite layers deposited atop FTO coated glass substrates with and without ARC layer.

Optical properties of the perovskite solar cells made with ITO and FTO transparent conductive oxides were compared. The result of this comparison is illustrated in Figure 45. As can be seen, a higher optical absorption and lower transmission is measured for the sample deposited on FTO coated glass substrate. This can be explained by different perovskite formation atop different substrates, which is clear in SEM images.
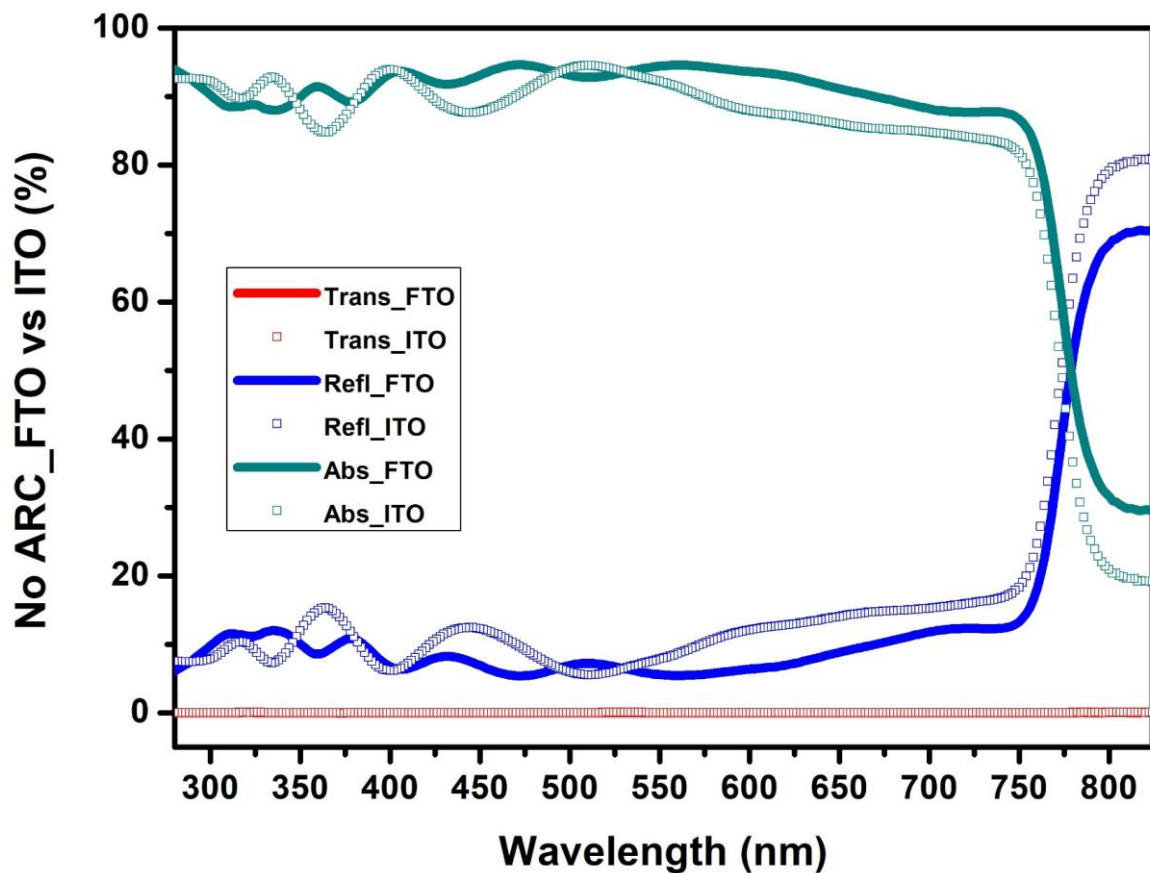
**Figure 45.** Comparison of the optical properties of the perovskite layers deposited atop ITO and FTO glass substrates.

The photovoltaic parameters were analyzed and compared for the solar cells made with ITO and FTO coated glass substrates (Figure 46). Slightly higher Jsc values in case of FTO is due to higher absorption in perovskite layers grown on top. Voc values are known to be correlated to the charge recombination in absorber bulk and interfaces. As can be seen in SEM images, the PCBM is well capped the smooth ITO substrate. This results in a good interface passivation, therefore higher Voc. FF values were higher for the solar cells made atop FTO. This is due to the interconnected grains and higher quality layer formation, while shunt passes can be seen in case of perovskite layer formed atop ITO substrate. Ultimately the PCE of the solar cells made using FTO substrates were higher than ITO.
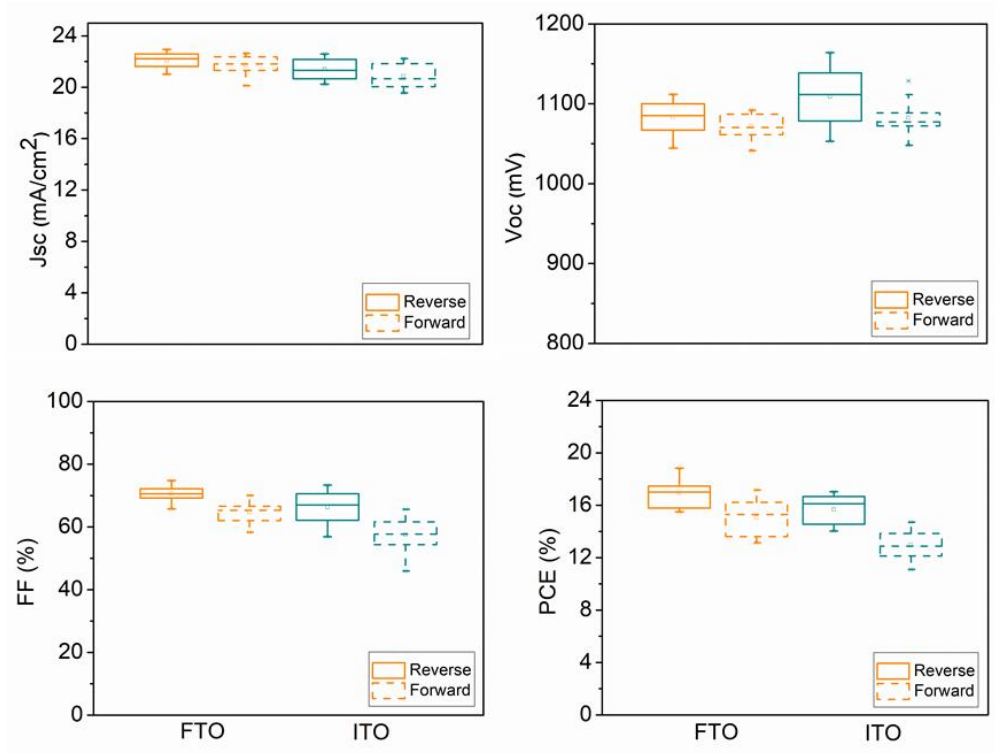
Figure 46. Comparison of the photovoltaic parameters of the perovskite layers deposited atop ITO and FTO glass substrates.

TRPL measurements were performed to compare the charge extraction qualities for the solar cells made atop FTO and ITO coated glass substrates. As can be seen in Figure 47, the decay trend is more or less the same with slightly more quenched PL signal in case of ITO.
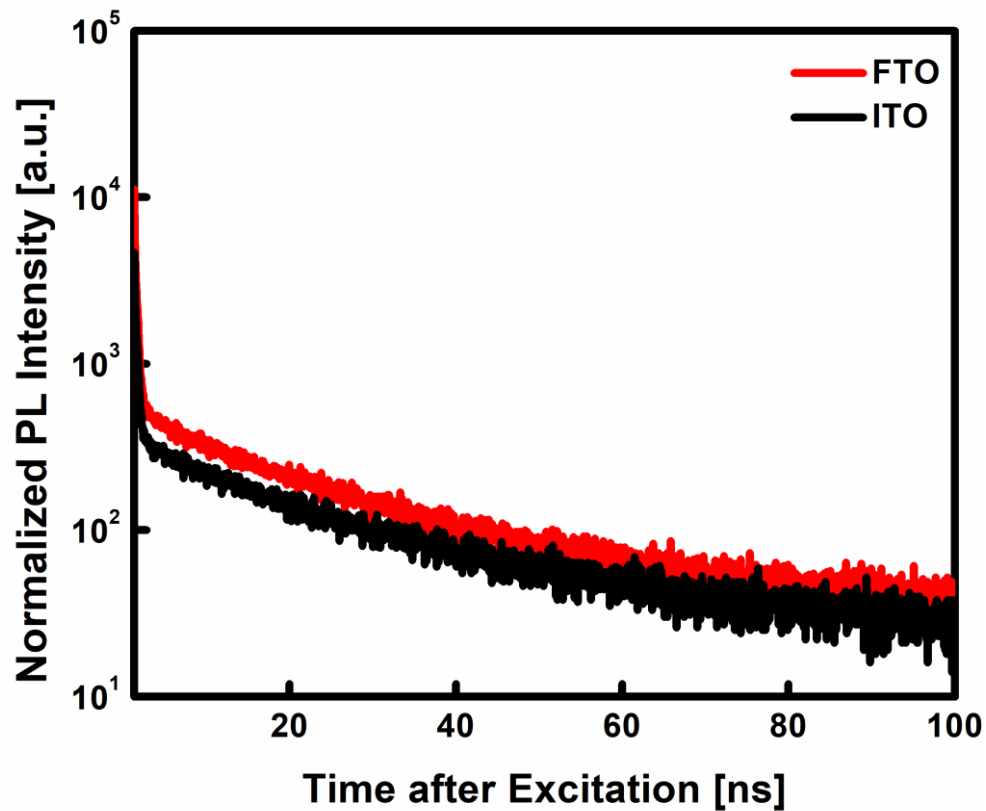
Figure 47. Comparison of the TRPL curves of the perovskite layers deposited atop ITO and FTO glass substrates.

The impact of the concentration of PCBM as an effective passivation layer on morphological and optoelectronic properties of perovskite solar cells has also been studied in this thesis. The PCBM concentration varied in the range of 0 (no PCBM layer) to 15 mg/ml. As can be seen from the cross-section (a) and top-view (b) SEM images in Figure 48, the crystallization and grain growth condition strongly affected by the PCBM concentration variation.
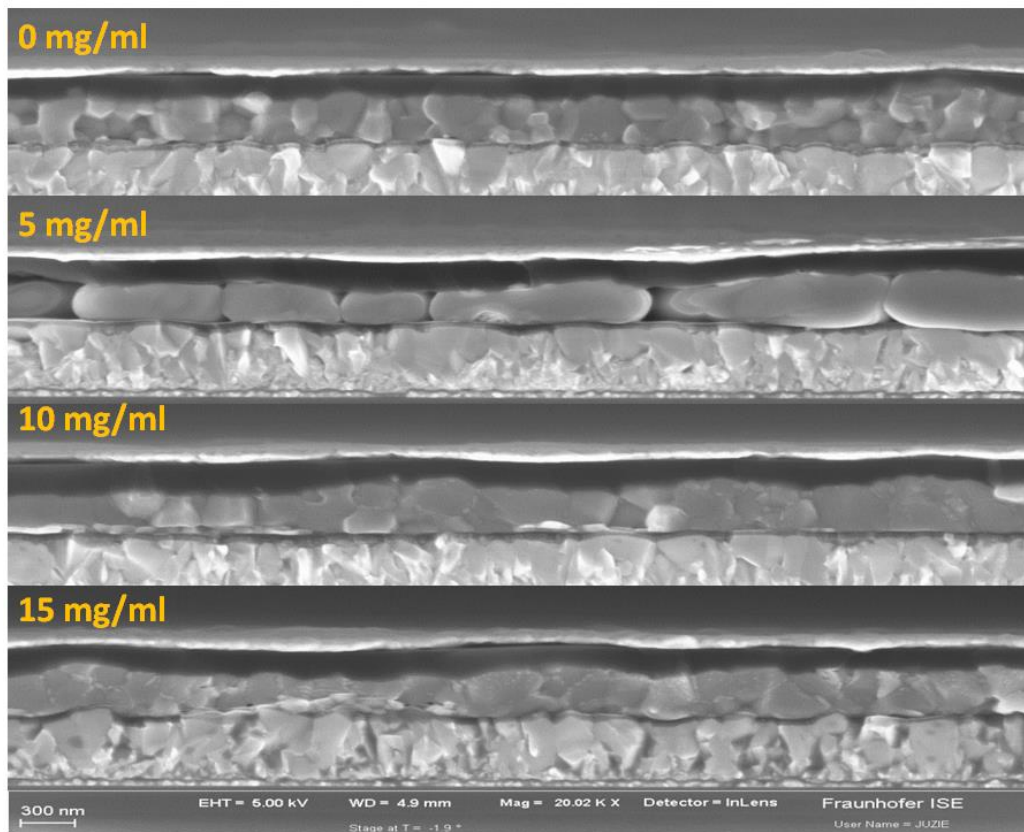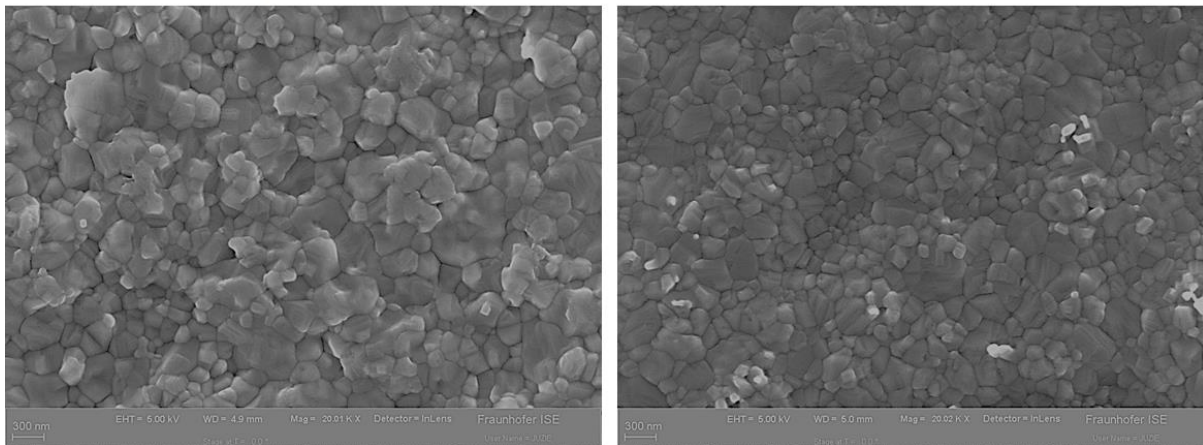
Figure 48. Cross-section (a) and top-view (b) SEM images of the perovskite solar cells made with PCBM layer with different concentrations.

Also the role of PCBM layer in perovskite layer formation atop flat and textured silicon was investigated. As can be seen in Figure 49 and 50, in presence of PCBM layer the crystal grains are strongly impinged while in case of no PCBM, the formed layer is not uniform and many voids appear between the grains.
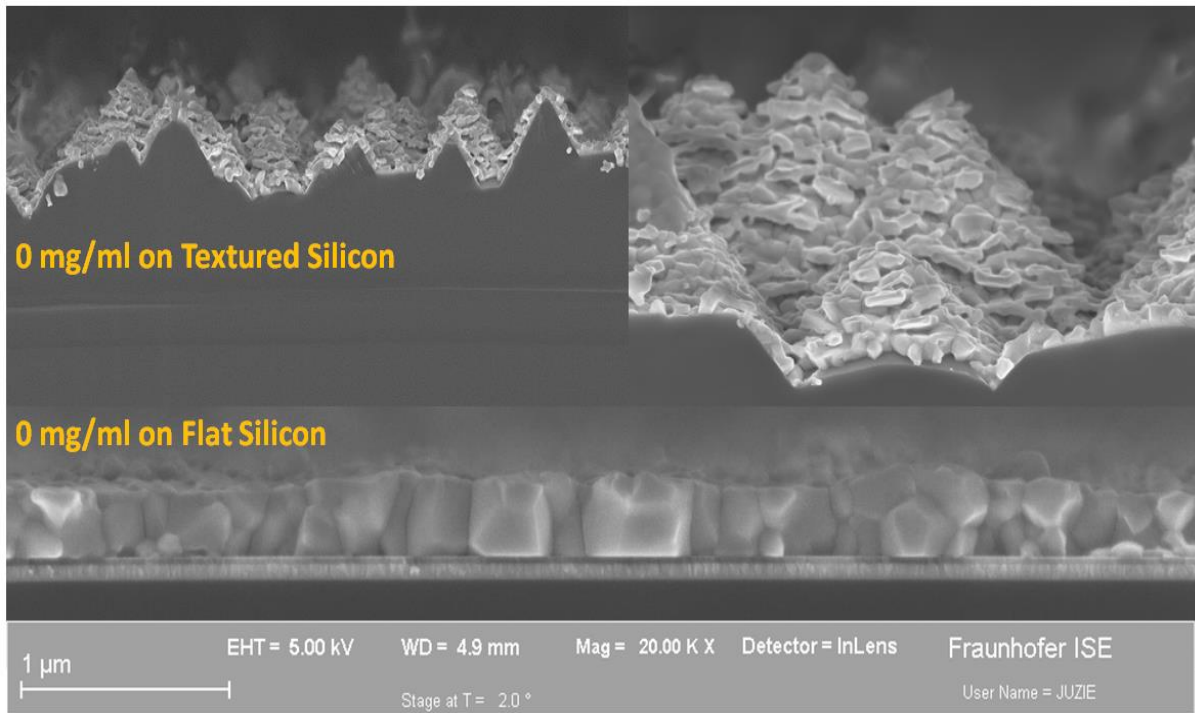
Figure 49. Perovskite layer formation atop flat and textured silicon without PCBM layer.
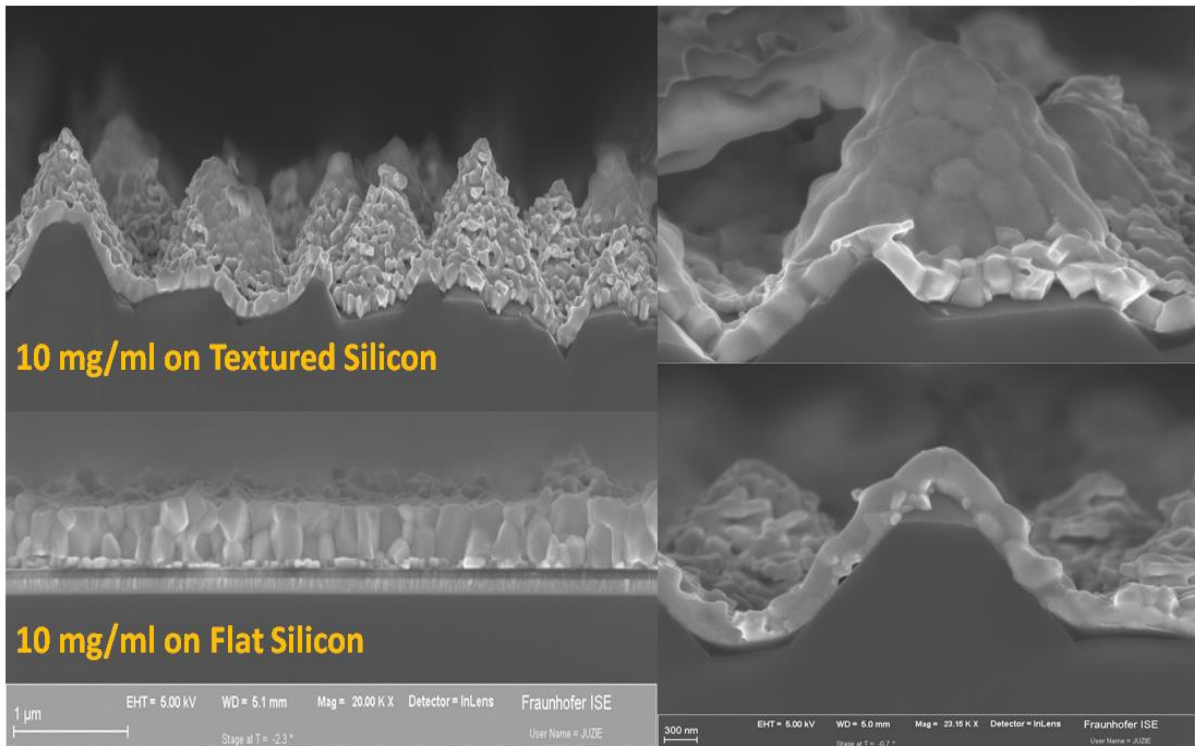
Figure 50. Perovskite layer formation atop flat and textured silicon with PCBM layer.

The steady-state PL measurements were done on the perovskite layers formed atop PCBM layer of different concentrations. The PL signal is strongly quenched for 10-15 mg/ml concentrations which promises a good charge carrier generation and extraction and thereupon high PCE.
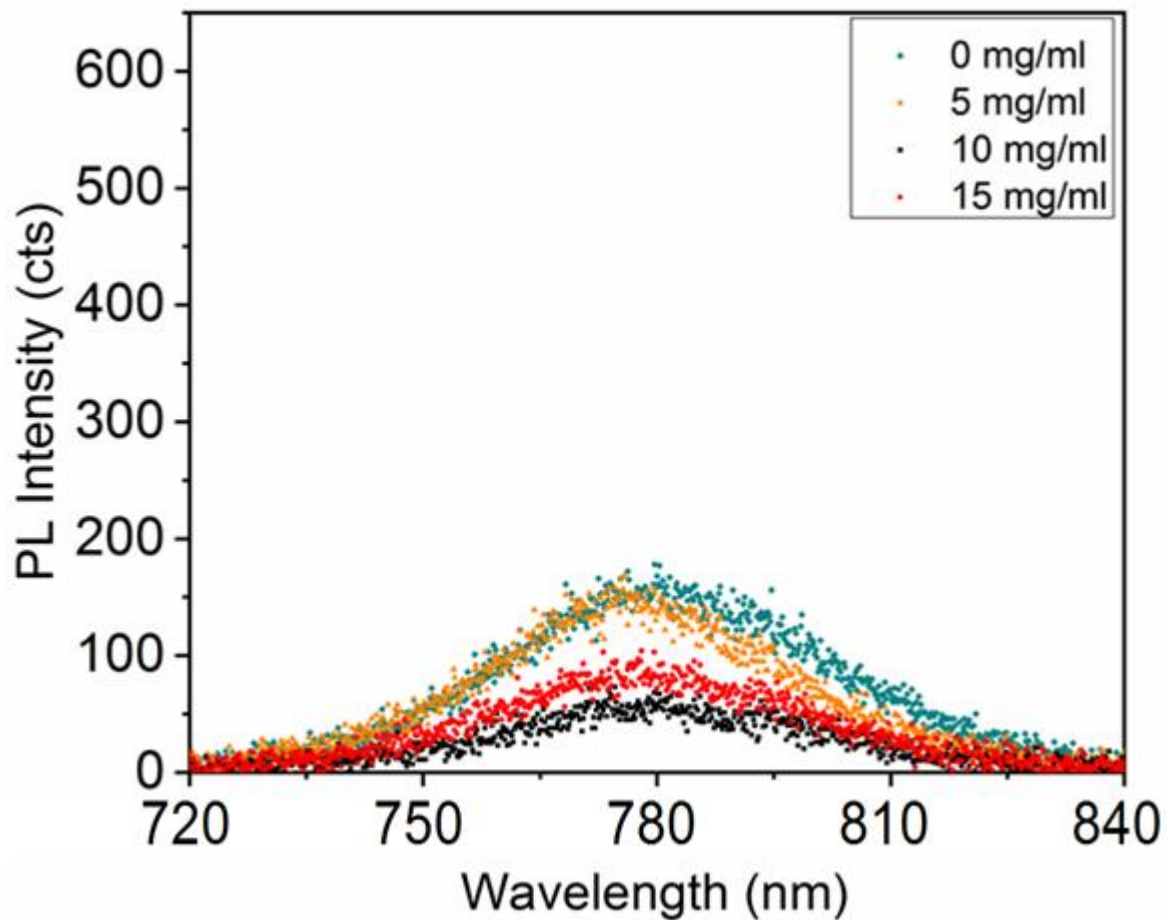
Figure 51. Steady-state PL measurements of the perovskite layers formed atop PCBM with different concentrations. The measurements are done from the back (glass) side.

Steady-state PL measurements depicted in Figure 51 were performed from the back side of the samples. These measurements are also done from the front side

(perovskite side). As can be seen in Figure 52, the trend of the curves are the same in comparison with Figure 51, but the curves are more separated. This could be due to the more photoexcited charge carriers generation closer to the perovskite/ETL interface.
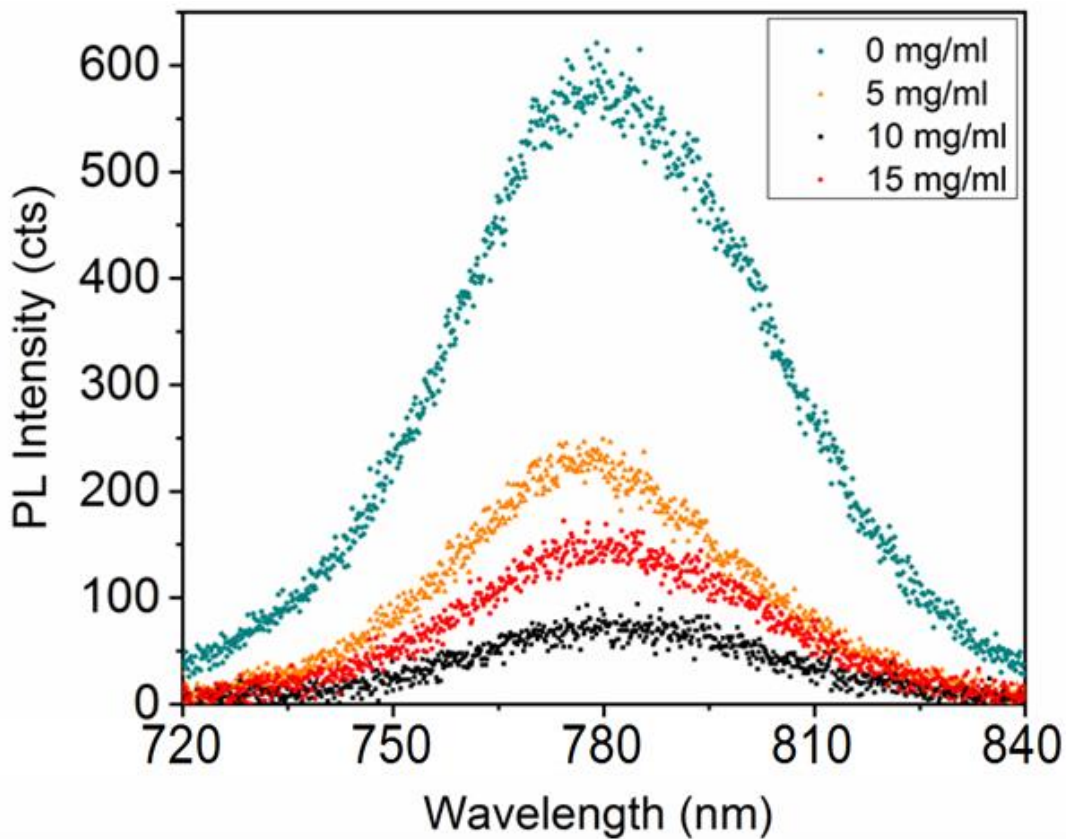
Figure 52. Steady-state PL measurements of the perovskite layers formed atop PCBM with different concentrations. The measurements are done from the top (perovskite) side.

JV and stabilized PCE measurements are shown in Figure 53 and 54. The impressive passivation role of the PCBM layer is visible where the efficiency and hysteresis are notably improved by increasing the PCBM concentration. The PCBM concentration of 10 mg/ml yielded the highest efficiency and lowest hysteresis.
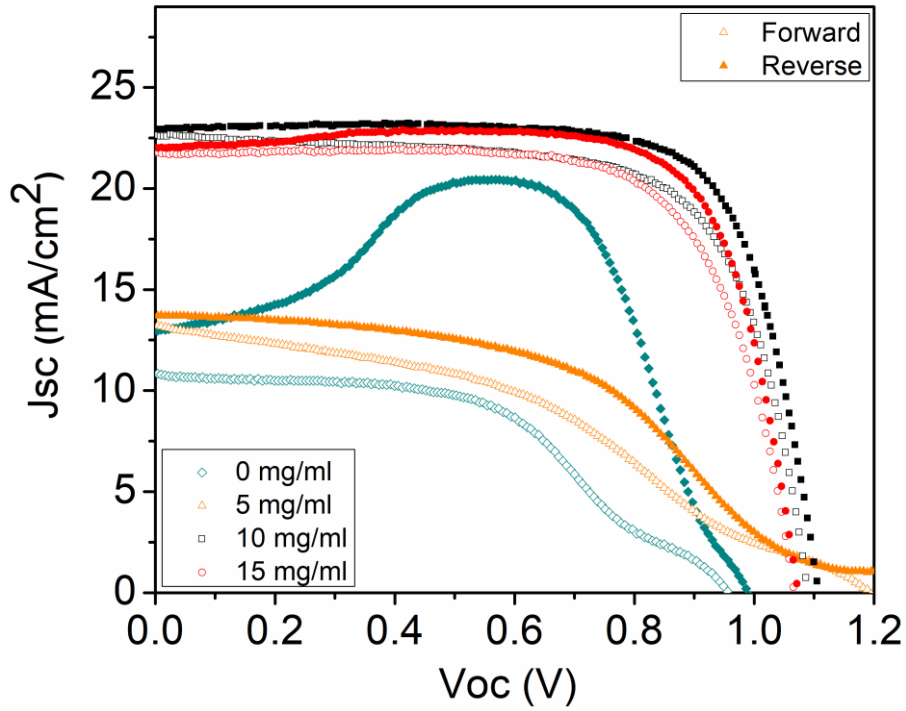
Figure 53. JV curves of perovskite solar cells made with PCBM layer of different concentrations.
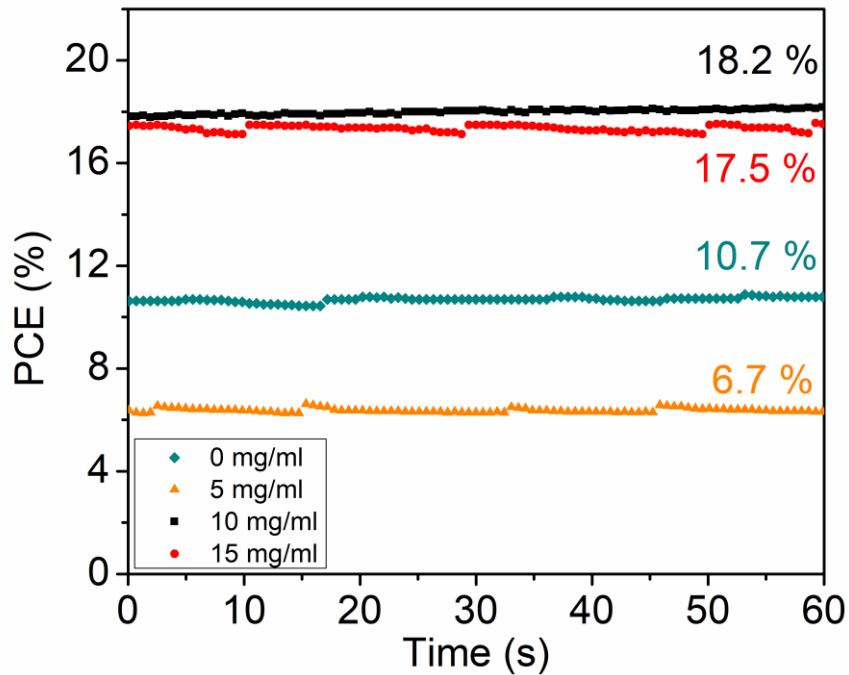
Figure 54. Stabilized PCE of perovskite solar cells made with PCBM layer of different concentrations.

The main photovoltaics figures of merit were measured and analyzed to understand the optimum concentration of PCBM in the solution used to prepare

passivation layer. Table IV presents the photovoltaic parameters of the champion solar cells made with PCBM layers of different concentrations. With 10 and 15 mg/ml, higher efficiencies and lower hysteresis were achieved. Comparing the results of concentration optimization, significant Voc, Jsc, and FF gains were achieved. This could be due to the uniform and compact layer formation as well as grains and interface passivation in case of higher PCBM concentrations.

Table IV. Photovoltaic parameters of the perovskite solar cells made with PCBM layer of different concentrations. 10-15 solar cells are made and analyzed for each concentration.

PCBM (mg/ml)	0		5		10		15	
Scan Direction	Forward	Reverse	Forward	Reverse	Forward	Reverse	Forward	Reverse
Jsc (mA/cm^2)	10.85	12.95	13.2	13.7	22.7	22.95	21.75	22.1
Voc (mV)	956	989.1	1192.9	1092.2	1090.6	1103.3	1065.9	1073.9
FF (%)	50.2	103.5 *	38.55	51.6	69.9	74.5	70.85	76.35
PCE (%)	5.2	13.26	6.1	7.72	17.3	18.9	16.43	18.12
Hysteresis (%)	60		21		8.4		9.3	

The highly reproducible 18%> efficiencies reported in sections 3.1-3.3 were achieved as a result of optimization of PbI$_2$ content (or MAI concentration) as well as both ETL and HTL layers. For all the results reported in experimental section of this thesis at least 10-15 samples were analyzed to have logical statics for reliable conclusions.

Chapter 4: Outlook

As single junction crystalline silicon (c-Si) solar cells approach their practical efficiency limits, new technologies are required to continue to this upward trend and further reduce the levelized cost of electricity (LCOE) of installed systems. Perovskite-silicon tandem solar cells are one very promising technology to achieve these goals by increasing the efficiency of c-Si cells with minimal additional fabrication costs. Such tandem cells have recently demonstrated certified efficiencies of up to 28%.[26]
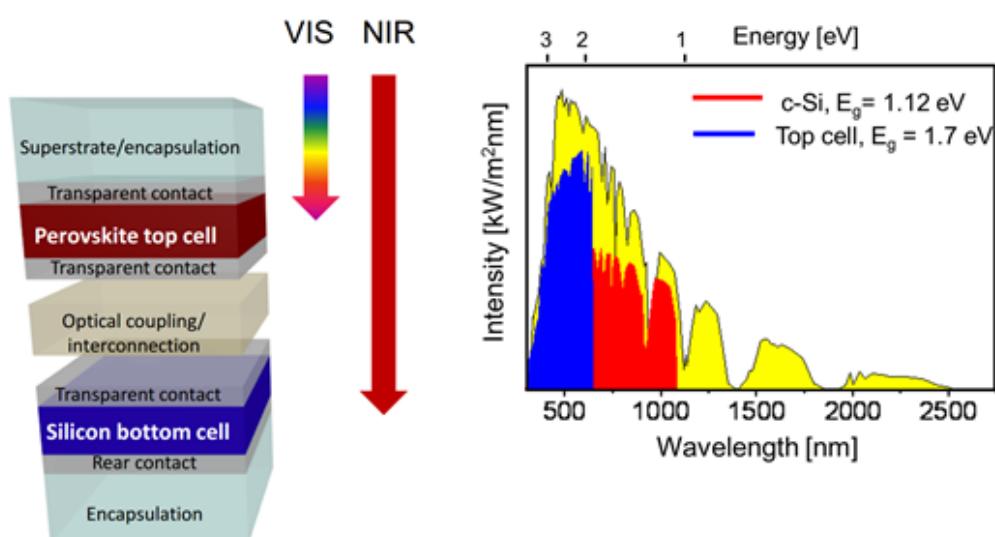
Figure 55. Schematic of perovskite/silicon monolithic tandem solar cell.

The perovskite-silicon tandem solar cells could be fabricated with three configurations. Monolithic two-terminal with direct contact between top and bottom cells,[22] mechanically stacked four-terminal with independently connected top and bottom cells[13] and optically coupled four-terminal featuring a mirror to reflect the light wave of longer wavelength to the bottom cell.[104] Each configuration has its pros and cons, two-terminal enables a direct electric connection between two cells through a tunnel junction. In this case only one TCO would be required resulting in low manufacturing costs and minimized parasitic absorption. Although, current matching between the two cells and possible fabrication damages on the bottom cells could be mentioned as draw backs of this configuration. Regarding four-terminal configuration, the fabrication of tandem solar cells which are mechanically stacked could be less demanding due to the separate top and bottom cells fabrication causing no damage on the bottom cell. However in this case there TCOs are required resulting in higher fabrication costs and parasitic absorption. Using a dichroic mirror within a four-terminal configuration could be a solution for lowering the parasitic absorption, however the expensive dichroic mirror could make the fabrication costly and less interesting. To choose the best strategy one should weigh up the pros and cons and find the best compromise.
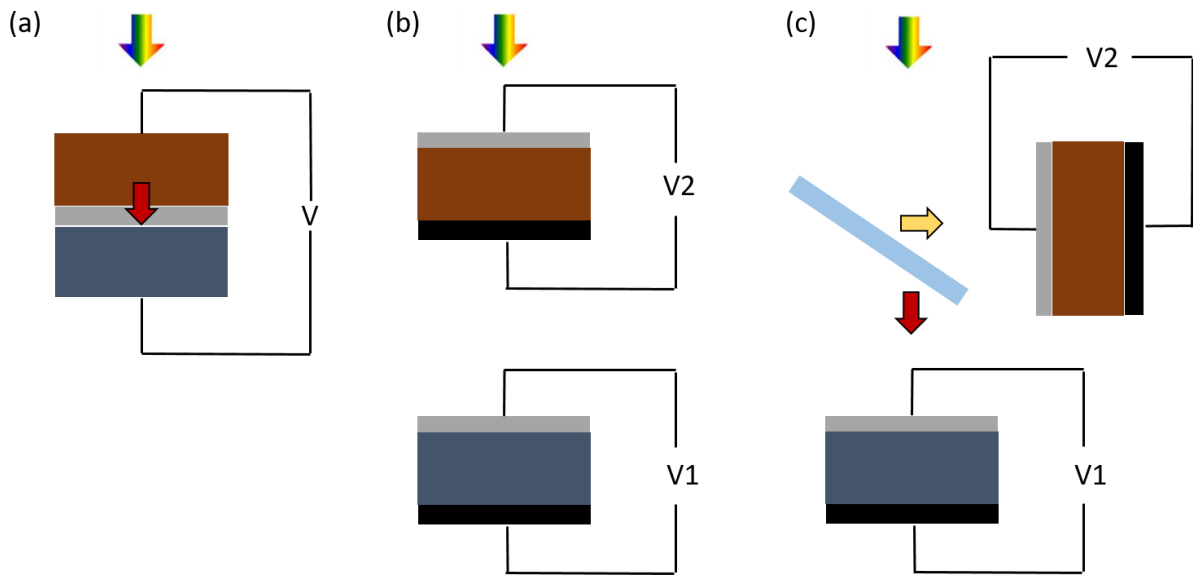
Figure 56. Schematic of different perovskite/silicon tandem solar cell configurations (a) monolithic 2-terminal, (b) mechanically stacked 4-terminal and (c) spectral splitting.

Different methods have been utilized for deposition of perovskite top cells on silicon bottom cells. From solution processing to evaporation-based methods. Solution processing enables easy compositional engineering in perovskite structure and band-gap tuning, interesting for tandem applications.[94-96] Figure 57 represents the $CsFAPb(I_{(1-x)}Br_x)_3$ perovskite layers formed with different Br contents in perovskite structure. By increasing the Br content the bad-gap increases but the color of absorber layer changes from dark black to amber and orange, which can negatively affect the light absorption in very high band-gaps. To realize an efficient tandem solar cell, band-gap engineering of top and bottom solar cells is crucial. Ability to band-gap tuning made perovskite a promising candidate as a top cell in tandem configuration on Silicon bottom cell.
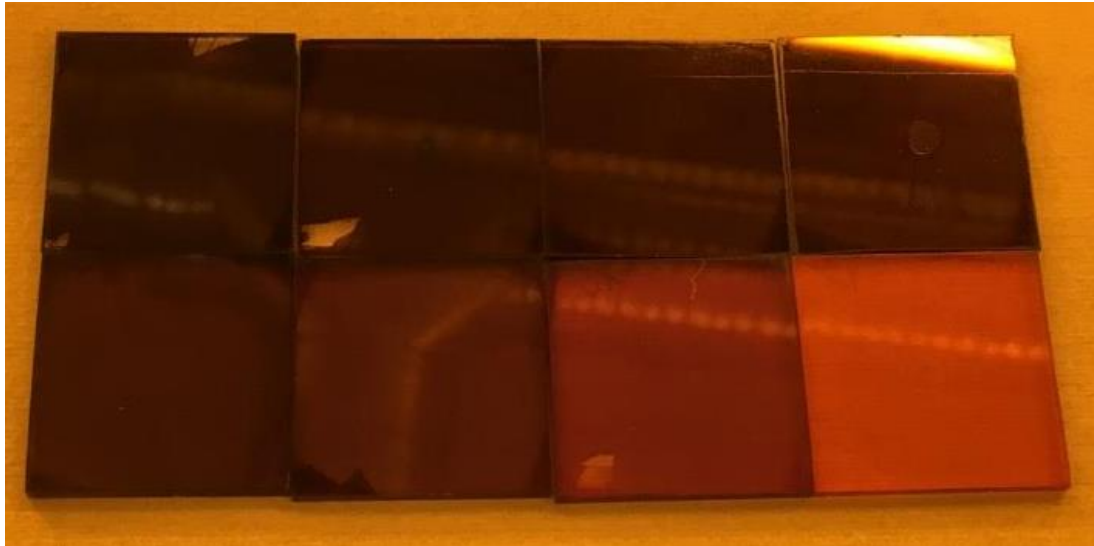
Figure 57. Perovskite layers formed with different Br contents. This study is carried out in CNST IIT lab in Milan.

Variable band-gaps of perovskite layers formed with different Br contents are illustrated in Figure 58.
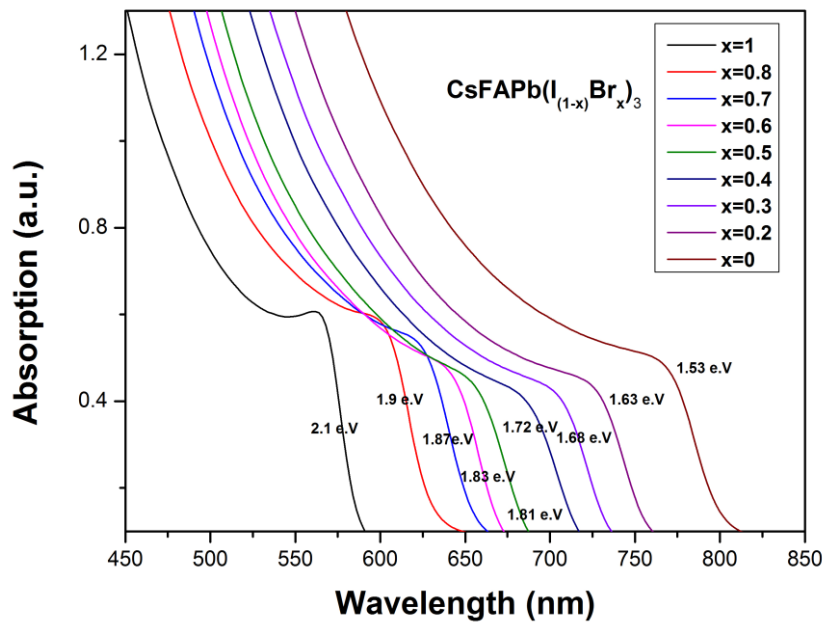
Figure 58. Band-gap engineering in perovskite layers by varying the Br contents. This study is carried out in CNST IIT lab in Milan.

As can be seen in Figure 58, by increasing the Br content a blue shift in absorption edge is visible. Based on theoretical and experimental investigations, a perovskite with band-gap of 1.68-1.72 eV is suitable for an efficient tandem perovskite/silicon solar cell.

To improve light trapping and reduce reflection at the front of the solar cell, industrial silicon cells are typically textured on both sides by a wet chemistry treatment, resulting in a pyramidal texture of a few micrometers in height. As the perovskite absorber is usually deposited via wet chemistry and its thickness is <1 μm, most of the tandem devices reported so far have featured a bottom cell that was mechanically polished on its front. Targeting compatibility with industrial monocrystalline c-Si process lines, a hybrid sequential deposition method could be a good candidate for the perovskite top cell deposition. Along with vacuum-deposited charge selective contacts, this approach enables to demonstrate a monolithic tandem solar cell featuring an n-type silicon heterojunction (SHJ) bottom cell textured on both sides, which has the potential to reach efficiencies beyond 30%.
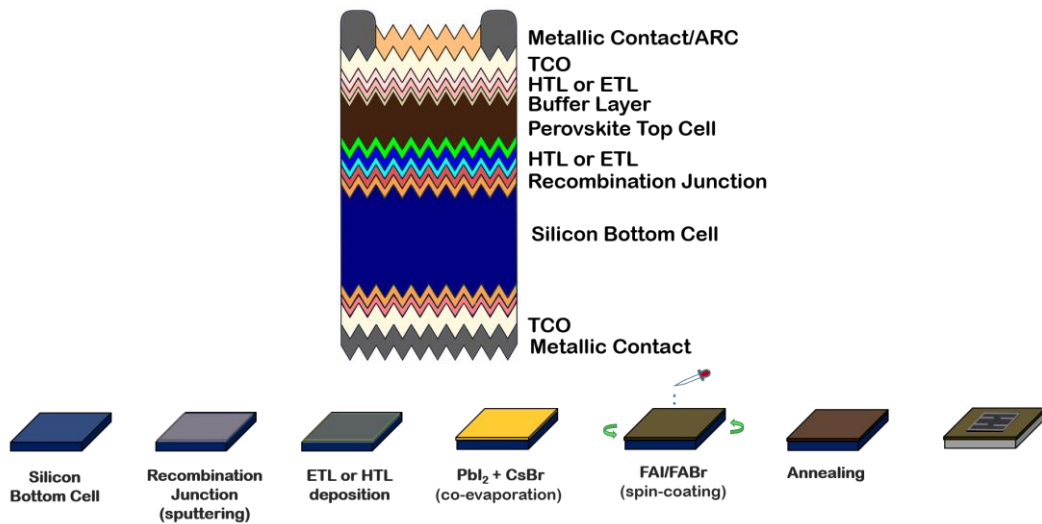
Figure 59. Perovskite-silicon tandem solar cell fabrication procedure using hybrid method for perovskite deposition and final schematic of perovskite-silicon tandem solar cell.

Basically, tandem configurations of a high band-gap top cell on a low band-gap bottom cell such as perovskite/silicon[94-96], perovskite/CIGS[97-98] perovskite/CdTe[99] and perovskite/perovskite[100] solar cells aiming to surpass the single junction efficiency limit, could pave the way of photovoltaics to become a game changer in the energy market. This is extremely important nowadays, as production of the greenhouse gases, resulting from consumption of the conventional energy sources, are seriously threating our environment. The global warming and climate change are the dangerous consequences. Therefore introducing a low-cost, highly efficient and highly stable source of energy such as tandem solar cells could be a solution. However, a lot of engineering and optimization works need to be done to address these three challenges in tandem solar cells.

Chapter 5: Conclusions

In this thesis a two-step hybrid evaporation-spincoating method was employed to fabricate low-temperature processed $MAPbI_3$ planar perovskite solar cells. The important role of charge transport layers and interface engineering on the perovskite grains growth and photovoltaic parameters of the final solar cells were addressed within an optimization study. The optimized value for PCBM deposition, as a substrate for perovskite top layer, resulted in a homogeneous and compact perovskite layer formation with well impinged grains and thereupon superb photovoltaic performance.

The role of crystallization and grain growth conditions on the morphological and optoelectronic properties as well as hysteresis behavior by a systematic variation of MAI concentrations in $MAPbI_3$ perovskite solar cells fabricated with a two-step hybrid evaporation-spin-coating method, was studied. Stoichiometry variation strongly impacted the crystallization and grain growth. The reduction in MAI concentrations down to 40 mg/ mL and accordingly increased PbI_2 incorporation resulted in highly crystalline perovskite layers with smaller but more impinged grain formation. For these samples, it was observed that the

remnant PbI_2 content correlated with higher efficiencies of photovoltaic operation, especially with higher voltages, higher currents, and thus higher efficiencies, as well as less hysteresis. The possible explanations for the superior performance with lower MAI concentrations were surface and interface passivation by PbI_2 and a positive contribution of interconnected grain boundaries allowing for improved charge extraction. Even lower MAI concentrations, however, then resulted in poor crystallization and low photovoltaic performance. Ultimately, 40 mg/mL is found to be the optimized value for the MAI concentration, resulting in the champion device stabilized efficiency of 18.2%. This is the highest value reported so far for perovskite solar cells fabricated with two-step hybrid evaporation-spincoating method.

Finally the structural and optoelectronic properties of perovskite solar cells made by hybrid method using FTO and ITO coated glasses substrates were compared. The results rationalized that the thin and rough FTO coating offered a well impinged crystal growth with good electronic couplings which resulted in high efficiency perovskite solar cells.

References

(1) Kadro, J. M.; Hagfeldt, A. The End-of-Life of Perovskite PV. *Joule* **2017**, *1*, 29-46.

(2) Yang, W. S.; Park, B. W. ; Jung, E. H.; Jeon, N. J.; Kim, Y. C.; Lee, D. U.; Shin, S. S.; Seo, J.; Kim, E. K.; Noh, J. H.; Seok, S.I. Iodide management in formamidinium-leadlhalide-based perovskite layers for efficient solar cells. *Science* **2017**, *356*, 1376-1379.

(3) Tan, H.; Jain, A.; Voznyy, O.; Lan, X.; De Arquer, F. P. G.; Fan, J. Z.; Bermudez, R. Q.; Yuan, M.; Zhang, B.; Zhao, Y.; Fan, F.; Li, P.; Quan, L. N.; Zhao, Y.; Lu, Z. H.; Yang, Z.; Hoogland, S.; Sargent, E. H. Efficient and stable solution-processed planar perovskite solar cells via contact passivation. *Science* **2017**, *355*, 722-726.

(4) Bi, D.; Tress, W.; Dar, M. I.; Gao, P.; Luo, J.; Renevier, C.; Schenk, K.; Abate, A.; Giordano, F., Correa-Baena, J.-P.; Decoppet, J. D.; Zakeeruddin, S. M.; Nazeeruddin, M. K.; Grätzel, M.; Hagfeldt, A. Efficient luminescent solar cells based on tailored mixed-cation perovskites. *Sci. Adv* **2016**, *2*, No. e1501170.

(5) Bi, D.; Luo, J.; Zhang, F.; Magrez, A.; Athanasopoulou, E. N.; Hagfeldt, A., Grätzel, M. Morphology engineering: a route to highly reproducible and high efficiency perovskite solar cells. *ChemSusChem* **2017**, *10,* 1624-1630.

(6) Correa-Baena, J.-P.; Saliba, M.; Buonassisi, T.; Grätzel, M.; Abate, A.; Tress, W.; Hagfeldt, A. Promises and challenges of perovskite solar cells. *Science* **2017**, *358*, 739-744.

(7) Tian, S.; Li, J. ; Li, S.; Bu, T.; Mo, Y.; Wang, S.; Li, W.; Huang, F. A facile green solvent engineering for up-scaling perovskite solar cell modules. *Solar Energy* **2019**, *183*, 386-391.

(8) Saliba, M.; Matsui, T.; Seo, J. Y.; Domanski, K.; Correa-Baena, J.-P; Nazeeruddin, M. K.; Zakeeruddin, S.M.; Tress, W.; Abate, A.; Hagfeldt, A.; Grätzel, M. Cesium-containing triple cation perovskite solar cells:improved stability, reproducibility and high effiency. *Energy Environ. Sci.* **2016**, *9*, 1989-1997.

(9) McMeekin, D. P.; Sadoughi, G.; Rehman, W.; Eperon, G. E.; Saliba, M.; Hörantner, A. Haghighirad, M. T.; Sakai, N.; Korte, L.; Rech, B.; Johnston, M. B.; Herz, L. M.; Snaith, H. J. A mixed-cation lead mixed-halide perovskite absorber for tandem solar cells. *Science* **2016**, *351*, 151-155.

(10) Bush, K. A.; Frohna, K.; Prasanna, R.; Beal, R. E.; Leijtens, T.; Swifter, S.A.; McGehee, M. D. Compositional engineering for efficient wide band gap perovskite with improved stability to photoinduced phase segregation. *ACS Energy Lett* **2018**, *3*, 428-435.

(11) Bush, K. A.; Palmstrom, A. F.; Yu, Z. J.; Boccard, M.; Cheacharoen, R.; Mailoa, J. P.; McMeekin, D. P.; Hoye, R. L. Z.; Bailie, C. D.; Leijtens,

T.; Peters, I. M.; Minichetti, M. C.; Rolston, N.; Prasanna, R.; Sofia, S.; Harwood, D.; Ma, W.; Moghadam, F.; Snaith, H. J.; Buonassisi, T.; Holman, Z. C.; Bent, S. F.; McGehee, M. D. 23.6%-efficient monolithic perovskite/silicon tandem solar cells with improved stability. *Nature Energy* **2017**, *17*, No. 17009.

(12) Mazzarella, L.; Lin, Y.; Kirner, S.; Morales-Vilches, A. B.; Korte, L.; Albrecht, S.; Crossland, E.; Stannowski, C.; Case, C.; Snaith, H. J.; Schlatmann, R. Infrared Light Management Using a Nanocrystalline Silicon Oxide Interlayer in Monolithic Perovskite/Silicon Heterojunction Tandem Solar Cells with Efficiency above 25%. *Adv. Energy Mater.* **2019**, *9*, 1803241.

(13) Jošt, M.; Köhnen, E.; Morales-Vilches, A. B.; Lipovšek, B.; Jäger, K.; Macco, B.; Al-Ashouri, A.; Krč, J.; Korte, L.; Rech, B.; Schlatmann, R.; Topič, M.; Stannowski, B.; Albrecht, S. Textured interfaces in monolithic perovskite/silicon tandem solar cells: advanced light management for improved efficiency and energy yield. *Energy Environ. Sci.* **2018**, *11*, 3511-3523.

(14) Werner, J.; Weng, C. H.; Walter, A.; Fesquet, L.; Seif, J. P.; Wolf, S. D.; Niesen, B.; Ballif, C. Efficient monolithic perovskite/silicon tandem solar cell with cell area >1 cm^2. *J. Phys. Chem. Lett*. **2016**, *7*, 161-166.

(15) Momblona, C.; Gil-Escrig, L.; Bandiello, E.; Hutter, E. M.; Sessolo, M.; Lederer, K.; Blochwitz-Nimoth, J.; Bolink, H. J. Efficient Vacuum

Deposited p-i-n and n-i-p Perovskite Solar Cells Employing Doped Charge Transport Layers. *Energy Environ. Sci*. **2016**, *9*, 3456–3463.

(16) Longo, G.; Momblona, C.; La-Placa, M.-G.; Gil-Escrig, L.; Sessolo, M.; Bolink, H. J. Fully Vacuum-Processed Wide Band Gap Mixed-Halide Perovskite Solar Cells. *ACS Energy Lett*. **2018**, *3*, 214-219.

(17) Rafizadeh, S.; Wienands, K.; Schulze, P. S. C.; Bett, A. J.; Andreani, L. C.; Hermle, M.; Glunz, S. W.; Goldschmidt, J. C. Efficiency Enhancement and Hysteresis Mitigation by Manipulation of Grain Growth Conditions in Hybrid Evaporated−Spin-coated Perovskite Solar Cells. *ACS Appl. Mater. Interfaces* **2019**, *11*, 722-729.

(18) Tao, C.; Neutzner, S.; Colella, L.; Marras, S.; Srimath Kandada, A. R.; Gandini, M.; Bastiani, M. D.; Pace, G.; Manna, L.; Caironi, M.; Bertarelli, C.; Petrozza, A. 17.6% Stabilized Efficiency in Low-Temperature Processed Planar Perovskite Solar Cells. *Energy Environ. Sci*. **2015**, *8*, 2365–2370.

(19) Rafizadeh, S.; Wienands, K.; Mundt, L. E.; Bett, A. J.; Schulze, P. S. C.; Andreani, L. C.; Hermle, M.; Glunz, S. W.; Goldschmidt, J. C. The Role of Surface Passivation Layer Prepration in Crystallization and Optoelectronic Performance of Hybrid Evaporated-Spincoated Perovskite Solar Cells. *IEEE JOURNAL OF PHOTOVOLTAICS* **2019**, *9*, 1428-1435.

(20) Abzieher, T.; Mathies, F.; Hetterich, M.; Welle, A.; Gerthsen, D.; Lemmer, U.; Paetzold, U. W.; Powalla, M. Additive-Assisted

Crystallization Dynamics in Two-Step Fabrication of Perovskite Solar Cells. *Phys.Status Solidi A*. **2017**, *214*, 1700509.

(21) Cojocaru, L.; Wienands, K.; Kim, T. W.; Uchida, S.; Bett, A. J.; Rafizadeh, S.; Goldschmidt, J. C.; Glunz, S. W. Detailed Investigation of Evaporated Perovskite Absorbers with High Crystal Quality on Different Substrates. *ACS Appl. Mater. Interfaces*. **2018**, *10*, 26293-26302.

(22) Sahli, F.; Werner, J.; Kamino, B. A.; Bräuninger, M.; Monnard, R.; Paviet-Salomon, B.; Barraud, L.; Ding, L.; Diaz Leon, J. J.; Sacchetto, D.; Cattaneo, G.; Despeisse, M.; Boccard, M.; Nicolay, S.; Jeangros, Q.; Niesen, B.; Ballif, C. Fully Textured Monolithic Perovskite/Silicon Tandem Solar Cells with 25.2% Power Conversion Efficiency. *Nature Materials* **2018**, *17*, 820-826.

(23) Kojima, A.; Teshima, K.; Shirai, Y.; Miyasaka, T. Organometal Halide Perovskites as Visible-Light Sensitizers for Photovoltaic Cells. *J. Am. Chem. Soc.* **2009**, *17*, 6050-6051.

(24) Snaith, H.J. Perovskites: The Emergence of a New Era for Low-Cost, High-Efficiency Solar Cells. *J. Phys. Chem. Let*. **2013**, *4*, 3623-3630.

(25) Green, M. A.; Ho-Baillie, A. Perovskite Solar Cells: The Birth of a New Era in Photovoltaics. *ACS Energy Lett*. **2017**, *2*, 822-830.

(26) Best Research-Cell Efficiencies. National Renewable Energy Laboratory (NREL), 2019. https://www.nrel.gov/pv/cell-efficiency.html.

(27) Saliba, M.; Correa-Baena, J.-P.; Grätzel, M.; Hagfeldt, A.; Abate, A. Perovskite Solar Cells: From the Atomic Level to Film Quality and Device Performance. *Angew. Chem. Int. Ed.* **2018**, *57, 2554-2569.

(28) Matteocci, F.; Vesce, L.; Kosasih, F. U.; Castriotta, L. A.; Cacovich, S.; Palma, A. L.; Divitini, G.; Ducati, C.; Di Carlo, A. Fabrication and Morphological Characterization of High-Efficiency Blade-Coated Perovskite Solar Modules. *ACS Appl. Mater. Interfaces.* **2019**, *11*, 25195-25204.

(29) Kim, J.; Kim, S.; Zuo, C.; Gao, M.; Vak, D.; Kim, D. Humidity-Tolerant Roll-to-Roll Fabrication of Perovskite Solar Cells via Polymer-Additive-Assisted Hot Slot Die Deposition. *Adv. Funct. Mater*. **2019**, *29*, 1809194.

(30) Howard, I. A.; Abzieher, T.; Hossain, I. M.; Eggers, H.; Schackmar, F.; Ternes, S.; Richards, B. S.; Lemmer, U.; Paetzold, U. W. Coated and Printed Perovskites for Photovoltaic Applications. *Adv. Mater.* **2019**, *31*, 1806702.

(31) Chang, N. L.; Ho-Baillie, A. W. Y.; Vak, D.; Gao, M.; Green, M. A.; Egan, R. J. Manufacturing cost and market potential analysis of demonstrated roll-to-roll perovskite photovoltaic cell processes. *Solar Energy Materials & Solar Cells* **2018**, *174*, 314–324.

(32) Schulze, P. S. C.; Bett, A. J.; Winkler, K.; Hinsch, A.; Lee, S.; Mastroianni, S.; Mundt, L. E.; Mundus, M.; Würfel, U.; Glunz, S. W.;

Hermle, M.; Goldschmidt, J. C. Novel Low-Temperature Process for Perovskite Solar Cells with a Mesoporous TiO$_2$ Scaffold. *ACS Appl. Mater. Interfaces* **2017**, *9*, 30567-30574.

(33) Stolterfoht, M.; Wolff, C. M.; Amir, Y.; Paulke, A.; Toro, L. P.; Caprioglio, P.; Neher, D. Approaching the fill factor Shockley–Queisser limit in stable, dopant-free triple cation perovskite solar cells. *Energy Environ. Sci.* **2017**, *10*, 1530-1539.

(34) Schutt, K.; Nayak, P. K.; Ramadan, A. J.; Wenger, B.; Lin, Y.; Snaith, H. J. Overcoming Zinc Oxide Interface Instability with a Methylammonium-Free Perovskite for High-Performance Solar Cells. *Adv. Funct. Mater.* **2019**, 1900466.

(35) Abzieher, T.; Moghadamzadeh, S.; Schackmar, F.; Eggers, H.; Sutterlüti, F.; Farooq, A.; Kojda, D.; Habicht, K.; Schmager, K.; Mertens, A.; Azmi, R.; Klohr, L.; Schwenzer, J. A.; Hetterich, M.; Lemmer, U.; Richards, B. S.; Powalla, M.; Paetzold, U. W. Electron-Beam-Evaporated Nickel Oxide Hole Transport Layers for Perovskite-Based Photovoltaics. *Adv Energy Mater.* **2019**, *9*, 1802995.

(36) Kim, G. Y.; Senocrate, A.; Yang, T.-Y.; Gregori, G.; Grätzel, M.; Maier, J. Large Tunable Photoeffect on Ion Conduction in Halide Perovskites and Implications for Photodecomposition. *Nature Materials.* **2018**, *17* (5), 445-449.

(37)   Snaith, H. J., Abate, A., Ball, J. M., Eperon, G. E., Leijtens, T., Noel, N. K., Stranks, S. D.; Wang, J. T-W.; Wojciechowski, K.; Zhang, W. Anomalous Hysteresis in Perovskite Solar Cells. *J. Phys. Chem. Lett.* **2014**, *5*, 1511-1515.

(38)   Yuan, Y.; Huang, J. Ion Migration in Organometal Trihalide Perovskite and Its Impact on Photovoltaic Efficiency and Stability. *Acc. Chem. Res.* **2016**, *49*, 286-293.

(39)   Son, D.-Y.; Kim, S.-G.; Seo, J.-Y.; Lee, S.-H.; Shin, H.; Lee, D.; Park, N.-G. Universal Approach toward Hysteresis-Free Perovskite Solar Cell via Defect Engineering. *J. Am. Chem. Soc.* **2018**, *40*, 1358-1364.

(40)   Turren-Cruz, S.-H.; Saliba, M.; Mayer, M. T.; Santiesteban, H. J.; Mathew, X.; Nienhaus, L.; Tress, W.; Erodici, M. P.; Sher, M. J.; Bawendi, M. G.; Grätzel, M.; Abate, A.; Hagfeldt, A.; Correa-Baena, J.-P. Enhanced charge carrier mobility and lifetime suppress hysteresis and imrove efficiency in planar perovskite solar cells. *Energy Environ. Sci.* **2018**, *11*, 78-86.

(41)   Weber, S. A. L., Hermes, I. M., Turren-Cruz, S.-H., Gort, C., Bergmann, V. W., Gilson, L., Hagfeldt, A.; Graetzel, M.; Tress, W.; Berger, R. How the Formation of Interfacial Charge Causes Hysteresis in Perovskite Solar Cells. *Energy Environ. Sci.* **2018**, *11*, 2404-2413.

(42)   Zhao, P.; Kim, B. J.; Jung, H. S. Passivation in perovskite solar cells: A review. *Materials Today Energ* **2018**, *7*, 267-286.

(43)   Wang, F.; Bai, S.; Tress, W.; Hagfeldt, A.; Gao, F. Defects Engineering for High-Performance Perovskite Solar Cells. *npj Flexible Electronics* **2018**, *2:22*, doi:10.1038/s41528-018-0035-z.

(44)   Peng, J.; Wu, Y.; Ye, W.; Jacobs, D. A.; Shen, H.; Fu, X.; Wan, Y.; Duong, T.; Wu, N.; Barugkin, C.; Nguyen, H. T.; Zhong, D.; Li, J.; Lu, T.; Liu, Y.; Lockrey, M. N.; Weber, K. J.; Catchpole, K. R.; White, T. P. Interface passivation using ultrathin polymer–fullerene films for high-efficiency perovskite solar cells with negligible hysteresis. *Energy Environ. Sci.* **2017**, *10*, 1792-1800.

(45)   Kegelmann, L.; Wolff, C. M.; Omondi, C. A.; Lang, F.; Unger, E. L.; Korte, L.; Dittrich, T.; Neher, D.; Rech, B.; Albrecht, S.It takes two to tango- double-layer selective contacts in perovskite solar cells for improved device performance and reduced hysteresis. *ACS Appl. Mater. Interfaces* **2017**, *9*, 17245-17255.

(46)   Wong, K. K.; Fakharuddin, A.; Ehrenreich, P.; Deckert, T.; Abdi-Jalebi, M.; Friend, R. H.; Schmidt-Mende, L. Interface-Dependent Radiative and Nonradiative Recombination in Perovskite Solar Cells. *J. Phys. Chem. C*. **2018**, *122* (20), 10691-10698.

(47)   Yadav, P.; Turren-Cruz, S.-H.; Prochowicz, D.; Tavakoli, M. M.; Pandey, K.; Zakeeruddin, S. M.; Grätzel, M.; Hagfeldt, A.; Saliba, M. Elucidation of Charge Recombination and Accumulation Mechanism in

Mixed Perovskite Solar Cells. *J. Phys. Chem. C*. **2018**, *122* (27), 15149-15154.

(48) Yun, J. S.; Baillie, A. H.; Huang, S.; Woo, S. H.; Heo, Y.; Seidel, J.; Huang, F.; Cheng, Y. B.; Green, M. A. Benefit of Grain Boundaries in Organic-Inorganic Halide Planar Perovskite Solar Cells. *J. Phys. Chem. Lett* **2015**, *6*, 875-880.

(49) Roose, B.; Ummadisingu, A.; Correa-Baena, J.-P., Saliba, M.; Hagfeldt, A.; Graetzel, M.; Steiner, U.; Abate, A. Spontaneous crystal coalescence enables highly efficient perovskite solar Cells. *Nano Energy* **2017**, *39*, 24-29.

(50) Lee, J.-W.; Bae, S.-H.; De Marco, N.; Hsieh, Y.-T.; Dai, Z.; Yang, Y. The Role of Grain Boundaries in Perovskite Solar Cells. *Materials Today Energy*. **2018**, *7*, 149-160.

(51) Li, J.-J.; Ma, J.-Y.; Ge, Q.-Q.; Hu, J.-S.; Wang, D.; Wan, L.-J. Microscopic Investigation of Grain Boundaries in Organolead Halide Perovskite Solar Cells. *ACS Appl. Mater. Interfaces*. **2015**, *7*, 28518-28523.

(52) Nguyen, B. P.; Kim, G. Y.; Jo, W.; Kim, B. J.; Jung, H. S. Trapping charges at grain boundaries and degradation of $CH_3NH_3Pb(I_{1-x} Br_x)_3$ perovskite solar cells. *Nanotechnology* **2017**, *28*, 315402.

(53) Yun, J. S.; Kim, J.; Young, T.; Patterson, R. J.; Kim, D.; Seidel, J.; Lim, S.; Green, M. A.; Huang, S.; Baillie, A. H. Humidity-Induced Degradation

via Grain Boundaries of HC(NH$_2$)$_2$PbI$_3$ Planar Perovskite Solar Cells. *Adv. Funct. Mater.* **2018**, *28*, 1705363.

(54) Shao, Y.; Fang, Y.; Li, T.; Wang, Q.; Dong, Q.; Deng, Y.; Yuan, Y.; Wei, H.; Wang, M.; Gruverman, A.; Shield, J.; Huang, J. rain boundary dominated ion migration in polycrystalline organic–inorganic halide perovskite films. *Energy Environ Sci*. **2016**, *9*, 1752-1759.

(55) Cho, K. T.; Paek, S.; Grancini, G.; Carmona, C. R.; Gao, P.; Lee, Y.; Nazeeruddin, M. K. Highly efficient perovskite solar cells with a compositionally engineered perovskite/hole transporting material interface. *Energy Environ. Sci*. **2017**, *10*, 621-627.

(56) Bett, A. J.; Schulze, P. S. C.; Winkler, K.; Gasparetto, J.; Ndione, P. F.; Bivour, M.; Hinsch, A.; Kohlstädt, M.; Lee, S.; Mastroianni, S.; Mundt, L. E.; Mundus, M.; Reichel, C.; Richter, A.; Veita, C.; Wienands, K.; Würfel, U.; Veurman, W.; Glunz, S. W.; Hermle, M.; Goldschmidt, J. C. Low temperature perovskite solar cells with an evaporated TiO$_2$ compact layer for perovskite silicon tandem solar cells. *Energy Procedia* **2017**, *4*, 567-576.

(57) Wojciechowski, K.; Leijtens, T.; Siprova, S.; Schlueter, C.; Hörantner, M. T.; Wang, J. T.-W.; Li, C.-Z.; Jen, A. K.-Y.; Lee, T.-L.; Snaith, H. J. C60 as an Efficient n-Type Compact Layer in Perovskite Solar Cells. *J. Phys. Chem. Lett*. **2015**, *6*, 2399-2405.

(58) Cui, J.; Meng, F.; Zhang, H.; Cao, K.; Yuan, H.; Cheng, Y.; Huang, F.; Wang, M. $CH_3NH_3PbI_3$-Based Planar Solar Cells with Magnetron-Sputtered Nickel Oxide. *ACS Appl. Mater. Interfaces* **2014**, *6*, 22862-22870.

(59) Seol, D.-J.; Lee, J.-W.; Park, N.-G. On the Role of Interfaces in Planar-Structured $HC(NH_2)_2PbI_3$ Perovskite Solar Cells. *ChemSusChem* **2015**, *8*, 2414-2419.

(60) Shi, J.; Xu, X.; Li, D.; Meng, Q. Interfaces in Perovskite Solar Cells. *Small* **2015**, *11*, 2472-2486.

(61) Fakharuddin, A.; Schmidt-Mende, L.; Garcia-Belmonte, G.; Jose, R.; Mora-Sero, I. Interfaces in Perovskite Solar Cells. *Adv. Energy Mater* **2017**, *7*, 1700623.

(62) Fan, R.; Huang, Y.; Wang, L.; Li, L.; Zheng, G.; Zhou, H. The Progress of Interface Design in Perovskite-Based Solar Cells. *Adv. Energy Mater* **2016**, *6*, 1600460.

(63) Chang, J.; Xiao, J.; Lin, Z.; Zhu, H.; Xu, Q.-H.; Zeng, K.; Hao, Y.; Ouyang, J. Elucidating the charge carrier transport and extraction in planar heterojunction perovskite solar cells by Kelvin probe force microscopy. *J. Mater. Chem. A* **2016**, *4*, 17464-17472.

(64) Dymshits, A.; Henning, A.; Segev, G.; Rosenwaks, Y.; Etgar, L. The electronic structure of metal oxide/organo metal halide perovskite

junctions in perovskite based solar cells. *Scientific Reports* **2015**, *5*, doi:10.1038/srep08704.

(65)   Zhou, L.; Chang, J.; Liu, Z.; Sun, X.; Lin, Z.; Chen, D.; Zhang, C.; Zhang, J.; Hao, Y. Enhanced planar perovskite solar cell efficiency and stability using a perovskite/PCBM heterojunction formed in one step. *Nanoscale* **2018**, *10*, 3053-3059.

(66)   Zuo, L.; Gu, Z.; Ye, T.; Fu, W.; Wu, G.; Li, H.; Chen, H. Enhanced Photovoltaic Performance of $CH_3NH_3PbI_3$ Perovskite Solar Cells through Interfacial Engineering Using Self-Assembling Monolayer. *J. Am. Chem. Soc.* **2015**, *137*, 2674-2679.

(67)   Zhou, H.; Chen, Q.; Li, G.; Luo, S.; Song, T. -b.; Duan, H.-S.; Hong, Z.; You, J.; Liu, Y.; Yang, Y. Interface engineering of highly efficient perovskite solar cells. *Science* **2014**, *345*, 542-546.

(68)   Yang, X.; Zhang, X.; Deng, J.; Chu, Z.; Jiang, Q.; Meng, J.; Wang, P.; Zhang, L.; Yin, Z.; You, J. Efficient green light-emitting diodes based on quasi-two-dimensional composition and phase engineered perovskite with surface passivation. *Nature Communications* **2018**, *9*, doi:10.1038/s41467-018-03702-1.

(69)   Zhang, X.; Wang, W.; Xu, B.; Liu, S.; Dai, H.; Bian, D.; Chen, S.; Wang, K.; Sun, X. W. Thin film perovskite light-emitting diode based on $CsPbBr_3$ powders and interfacial engineering. *Nano Energy* **2017**, *37*, 40-45.

(70)   Harwell, J. R.; Whitworth, G. L.; Turnbull, G. A.; Samuel, I. D. W. Green Perovskite Distributed Feedback Lasers. *Scientific Reports* **2017**, *7*, doi:10.1038/s41598-017-11569-3.

(71)   Kakavelakis, G.; Gagaoudakis, E.; Petridis, K.; Petromichelaki, V.; Binas, V.; Kiriakidis, G.; Kymakis, E. Solution Processed $CH_3NH_3PbI_3$–xClx Perovskite Based Self-Powered Ozone Sensing Element Operated at Room Temperature. *ACS Sens.* **2017**, *3*, 135-142.

(72)   Wang, H., Kim, D. H. Perovskite-based photodetectors: materials and devices. *Chem. Soc. Rev.* **2017**, *46*, 5204-5236.

(73)   Feng, J.; Gong, C.; Gao, H.; Wen, W.; Gong, Y.; Jiang, X.; Zhang, B.; Wu, Y.; Wu, Y.; Fu, H.; Jiang, L.; Zhang, X. Single-crystalline layered metal-halide perovskite nanowires for ultrasensitive photodetectors. *Nature Electronics* **2018**, *1*, 404-410.

(74)   Gill, H. S.; Elshahat, B.; Kokil, A.; Li, L.; Mosurkal, R.; Zygmanski, P.; Sajo, E.; Kumar, J. Flexible perovskite based X-ray detectors for dose monitoring in medical imaging applications. *Physics in Medicine* **2018,** *5*, 20-23.

(75)   Xu, Q.; Wei, H.; Wei, W.; Chuirazzi, W.; DeSantis, D.; Huang, J.; Cao, L. Detection of charged particles with a methylammonium lead tribromide perovskite single crystal. *Nuclear Inst. and Methods in Physics Research, A* **2018**, *848*, 106-108.

(76) Ciro, J.; Betancur, R.; Mesa, S.; Jaramillo, F. High performance perovskite solar cells fabricated under high relative humidity conditions. *Solar Energy Materials & Solar Cells* **2017**, *163*, 38-42.

(77) Song, Z.; Abate, A.; Watthage, S. C.; Liyanage, G. K.; Phillips, A. B.; Steiner, U.; Graetzel, M.; Heben, M. J. Perovskite Solar Cell Stability in Humid Air: Partially Reversible Phase Transitions in the PbI_2 CH_3NH_3I-H_2O System. *Adv. Energy Mater* **2016**, 6, 1600846.

(78) Han, G. S.; Yoo, J. S.; Yu, F.; Duff, M. L.; Kang, B. K.; Lee, J.-K. Highly stable perovskite solar cells in humid and hot environment. *J. Mater. Chem. A* **2017**, *5*, 14733-14740.

(79) Fu, Q.; Tang, X.; Huang, B.; Hu, T.; Tan, L.; Chen, L.; Chen, Y. Recent Progress on the Long-Term Stability of Perovskite Solar Cells. *Advanced Science* **2018**, *5*, 1700387.

(80) Liu, C.; Hu, M.; Zhou, X.; Wu, J.; Zhang, L.; Kong, W.; Li, X.; Zhao, X.; Dai, S.; Xu, B.; Cheng, C. Efficiency and stability enhancement of perovskite solar cells by introducing $CsPbI_3$ quantum dots as an interface engineering layer. *NPG Asia Materials* **2018**, *10*, 552-561.

(81) Habisreutinger, S. N.; McMeekin, D. P.; Snaith, H. J.; Nicholas, R. J. Research Update: Strategies for improving the stability of perovskite solar cells. *APL Materials* **2016**, *4*, 091503.

(82)   Chen, Y.; Zhang, L.; Zhang, Y.; Gao, H.; Yan, H. Large-area perovskite solar cells – a review of recent progress and issues. *RSC Adv.* **2018**, *8*, 10489-10508.

(83)   Gao, L.-L.; Li, C.-X.; Li, C.-J.; Yang, G.-J. Large-area high-efficiency perovskite solar cells based on perovskite films dried by the multi-flow air knife method in air. *J. Mater. Chem. A* **2017**, *5*, 1548-1557.

(84)   Jung, Y.-S.; Hwang, K.; Heo, Y.-J.; Kim, J.-E.; Vak, D.; Kim, D.-Y. Progress in Scalable Coating and Roll-to-Roll Compatible Printing Processes of Perovskite Solar Cells toward Realization of Commercialization. *Adv. Optical Mater* **2018**, *6*, 1701182.

(85)   Zuo, C.; Vak, D.; Angmo, D.; Ding, L.; Gao, M. One-step roll-to-roll air processed high efficiency perovskite solar cells. *Nano Energy* **2018**, *46*, 185-192.

(86)   Bishop, J. E.; Routledge, T. J.; Lidzey, D. G. Advances in Spray-Cast Perovskite Solar Cells. *J. Phys. Chem. Lett.* **2018**, *9*, 1977-1984.

(87)   Deng, Y.; Peng, E.; Shao, Y.; Xiao, Z.; Dong, Q.; Huang, J. Scalable fabrication of efficient organolead trihalide perovskite solar cells with doctor-bladed active layers. *Energy Environ. Sci.* **2015**, *8*, 1544-1550.

(88)   Mathies, F.; Eggers, H.; Richards, B. S.; Hernandez-Sosa, G.; Lemmer, U.; & Paetzold, U. W. Inkjet-Printed Triple Cation Perovskite Solar Cells. *ACS Appl. Energy Mater.***2018**, *1*, 1834-1839.

(89) Liu, F.; Dong, Q.; Wong, M. K.; Djurišic, A. B.; Ng, A.; Ren, Z.; Shen, Q.; Surya, C.; Chan, W. K.; Wang, J.; Ng, A. M. C.; Liao, C.; Li, H.; Shih, K.; Wei, C.; Su, H.; Dai, J. Is excess PbI$_2$ beneficial for perovskite solar cell performance? *Adv. Energy Mater*. **2016**, *6*, No. 1502206.

(90) Kim, Y. C.; Jeon, N. J.; Noh, J. H.; Yang, W. S.; Seo, J.; Yun, J. S.; Baillie, A. H.; Huang, S.; Green, M. A.; Seidel, J.; Ahn, T. K.; Seok, S. II. Beneficial Effects of PbI$_2$ Incorporated in Organo-Lead Halide Perovskite Solar Cells. *Adv. Energy Mater*. **2016**, *6*, No. 1502104.

(91) Cao, D. H.; Stoumpos, C. C.; Malliakas, C. D.; Katz, M. J.; Farha, O. K.; Hupp, J. T.; Kanatzidis, M. G. Remnant PbI$_2$, an Unforeseen Necessity in High-Efficiency Hybrid Perovskite-Based Solar Cells? *APL Materials*. **2014**, *2*, 091101.

(92) Chen, Y.; Yerramilli, A.; Shen, Y.; Zhao, Z.; Alford, T. Effect of Excessive Pb Content in the Precursor Solutions on the Properties of the Lead Acetate Derived CH$_3$NH$_3$PbI$_3$ Perovskite Solar Cells. *Solar Energy Materials and Solar Cells*. **2018**, *174*, 478-484.

(93) Bi, D.; El-Zohry, A. M.; Hagfeldt, A.; Boschloo, G. Unraveling the Effect of PbI$_2$ Concentration on Charge Recombination Kinetics in Perovskite Solar Cells. *ACS Photonics*. **2015**, *2*, 589-594.

(94) Leijtens, T.; Bush, K. A.; Prasanna, R.; McGehee, M. D. Opportunities and challenges for tandem solar cells using metal halide perovskite semiconductors. *Nature Energy* **2018**, *3*, 828-838.

(95) Altazin, S.; Stepanova, L.; Werner, J.; Niesen, B.; Ballif, C.; Ruhstaller, B. Design of perovskite/crystalline-silicon monolithic tandem solar cells. *Optics Express* **2018**, *26*, A579.

(96) Jiang, F.; Liu, T.; Luo, B.; Tong, J.; Qin, F.; Xiong, S.; Li, Z.; Zhou, Y. A two-terminal perovskite/perovskite tandem solar cell. *J. Mater. Chem. A* **2016**, *4*, 1208-1213.

(97) Shen, H.; Duong, T.; Peng, J.; Jacobs, D.; Wu, N.; Gong, J.; Wu, Y.; Karuturi, K. K,; Fu, X.; Weber, K.; Xiao, X.; White, T. P.; Catchpole, K. Mechanically-stacked perovskite/CIGS tandem solar cells with efficiency of 23.9% and reduced oxygen sensitivity. *Energy Environ. Sci.* **2018**, 11, 394-406.

(98) Han, Q.; Hsieh, Y.-T.; Meng, L.; Wu, J.-L.; Sun, P.; Yao, E.-P.; Chang, S.-Y.; Bae, S.-H.; Kato, T.; Bermudez, V.; Yang, Y. High-performance perovskite/Cu(In,Ga)Se$_2$ monolithic tandem solar cells. *Science* **2018**, *361*, 904-908.

(99) Rühle, S. The detailed balance limit of perovskite/silicon and perovskite/CdTe tandem solar cells. *Phys.Status Solidi A.* **2017**, *214*, 1600955.

(100) Sheng, R.; Hörantner, M. T.; Wang, Z.; Jiang, Y.; Zhang, W.; Agosti, A.; Huang, S.; Hao, X.; Ho-Baillie, A.; Green, M.; Snaith, H. J. Monolithic Wide Band Gap Perovskite/Perovskite Tandem Solar Cells with Organic Recombination Layers. *J. Phys. Chem. C* **2017**, *121*, 27256-27262.

(101) Caprioglio, P.; Stolterfoht, M.; Wolff, C. M.; Unold, T.; Rech, B.; Albrecht, S.; Neher, D. On the Relation between the Open-Circuit Voltage and Quasi-Fermi Level Splitting in Efficient Perovskite Solar Cells. *Adv Energy Mater.* **2019**, 1901631.

(102) Gharibzadeh, S.; Abdollahi Nejand, B.; Jakoby, M., Abzieher, T.; Hauschild, D.; Moghadamzadeh, S.; Schwenzer, J. A.; Brenner, P.; Schmager, R.; Haghighirad, A. A.; Weinhardt, L.; Lemmer, U.; Richards, B. S.; Howard, I. A.; Paetzold, U. W. Record Open-Circuit Voltage Wide-Bandgap Perovskite Solar Cells Utilizing 2D/3D Perovskite Heterostructure. *Adv. Energy Mater*. **2019**, 1803699.

(103) https://www.perkinelmer.com/product/lambda-850-uv-vis-spectrophotometer-l950

(104) Sheng, R.; Ho-Baillie, A. W. Y.; Huang, S.; Keevers, M.; Hao, X.; Jiang, L.; Cheng, Y.-B.; Green, M. A. Four-Terminal Tandem Solar Cells Using CH3NH3PbBr3 by Spectrum Splitting. *J. Phys. Chem. Lett.* **2015**, *6*, 3931-3934.